

Volume 3, Issue 1, 2025

Print ISSN: 2959-9865
Online ISSN: 2959-9873

WORLD JOURNAL OF ENGINEERING RESEARCH



Copyright© Upubscience Publisher

World Journal of Engineering Research

Volume 3, Issue 1, 2025



Published by Upubscience Publisher

Copyright© The Authors

Upubscience Publisher adheres to the principles of Creative Commons, meaning that we do not claim copyright of the work we publish. We only ask people using one of our publications to respect the integrity of the work and to refer to the original location, title and author(s).

Copyright on any article is retained by the author(s) under the Creative Commons Attribution license, which permits unrestricted use, distribution, and reproduction in any medium, provided the original work is properly cited.

Authors grant us a license to publish the article and identify us as the original publisher.

Authors also grant any third party the right to use, distribute and reproduce the article in any medium, provided the original work is properly cited.

World Journal of Engineering Research

Print ISSN: 2959-9865 Online ISSN: 2959-9873

Email: info@upubscience.com

Website: <http://www.upubscience.com/>

Table of Content

ENGINEERING FOR SUSTAINABLE DEVELOPMENT IN AFRICA: CHALLENGES, INNOVATIONS, AND COLLABORATIVE PATHWAYS Okechukwu Chidoluo Vitus	1-7
SIMULATION ANALYSIS OF THE DYNAMIC RESPONSE CHARACTERISTICS OF A TYPICAL GOLD MINE TAILING DAM UNDER THE COUPLING OF EARTHQUAKE AND RAINFALL PengJin Liu, Jie Wang, JiaFa Du, JianFei Sun*, YongLiang Zhang, HongWei Mu	8-19
PROGRESS ON URBAN RECREATIONAL GREEN SPACE ACCESS BASED ON BIBLIOMETRIC ANALYSIS SiRu Ye, HongJun Xie*	12-15
FAULT DIAGNOSIS METHOD OF AERO-ENGINE ROLLING BEARINGS BASED ON TIME-FREQUENCY ANALYSIS AND MACHINE LEARNING YeQi Jin	33-40
THE FLOW AND COMPONENT VARIATION CHARACTERISTICS OF THE HYDROGEN SUPPLY SYSTEM IN FUEL CELLS JingGuang Xie*, NanNan Liao, JianHua Liu, Jun Li, YaNan Gao	41-46
EXPLORATION OF THE DETECTION METHOD OF THE CONDITION OF PATIENTS ON THE AMBULANCE STRETCHER XinLei Yang, JueXiao Chen*	47-51
FUNCTIONAL ENHANCEMENT OF ENZYMATICALLY HYDROLYZED DOUBLE CROSSLINKED HOT MELT STARCH Hao Wang, ChuanWei Zhang*	52-64
A NOVEL VEHICLE TRAJECTORY TRACKING CONTROL METHOD BASED ON HORIZONTAL–VERTICAL DECOUPLING Zheng Hao	65-74
INTERNAL HEAT AND MASS TRANSFER MECHANISM OF SOLAR CPC CONCENTRATOR ADSORBER BASED ON CFD SIMULATION YuDong Li*, HaiPeng Sun, XiuJuan Chen	75-82
LEAST SQUARES AND CLUSTER ANALYSIS BASED METHODOLOGY FOR SONIC BOOM LOCALIZATION OF ROCKET DEBRIS XianYang Zhou*, WeiRong Zhang, SiQi Ji, Yang Song	83-89

ENGINEERING FOR SUSTAINABLE DEVELOPMENT IN AFRICA: CHALLENGES, INNOVATIONS, AND COLLABORATIVE PATHWAYS

Okechukwu Chidoluo Vitus

Omnibus Institute of Professional Learning and Development, Lagos 42100, Nigeria.

Corresponding Email: jlcm medias@gmail.com

Abstract: This research article explores the unique challenges and opportunities present in the field of engineering in Africa, motivated by the continent's rapid development and the critical need for sustainable solutions. Despite abundant resources and a youthful population, Africa faces significant obstacles, including inadequate infrastructure, limited access to education, and socio-economic disparities. The study analyzes various engineering disciplines, highlighting innovations that address local issues, such as renewable energy technologies, water management systems, and transportation networks. Key findings indicate that collaborative efforts among governments, academia, and industry stakeholders are essential for fostering an environment conducive to engineering advancements. Additionally, the research identifies a growing emphasis on local content in engineering projects, which not only promotes economic growth but also enhances skills transfer and capacity building within communities. The implications of this study are far-reaching, suggesting that by investing in engineering education and infrastructure, African nations can harness their potential, drive technological innovation, and improve the quality of life for their citizens. This article aims to contribute to a greater understanding of the engineering landscape in Africa and inspire further research and investment in the region, ultimately leading to sustainable development and prosperity.

Keywords: Engineering; Research; Africa; Sustainable development and prosperity

1 INTRODUCTION

Engineering research in Africa is a critical field that holds the potential to address numerous local challenges while simultaneously driving economic development and fostering innovation. With diverse and complex problems ranging from inadequate infrastructure to energy shortages, the necessity for targeted engineering solutions is more pressing than ever. As the continent grapples with rapid urbanization and climate change, engineering research emerges as a vital element in crafting sustainable responses tailored to the unique context of African nations.

The current state of engineering education and research across various African countries reveals a mixed landscape. While some nations, such as South Africa and Kenya, have made significant strides in establishing robust engineering programs and research initiatives, others still face substantial hurdles. Challenges include limited funding, inadequate facilities, and a shortage of qualified educators, which hinder the development of a capable workforce. Despite these obstacles, there is a palpable enthusiasm among students and young professionals, driven by a desire to innovate and contribute to their communities.

In recent years, there has been a growing recognition of the importance of local content in engineering projects. This shift not only aims to enhance project outcomes but also focuses on building local capacity through skills transfer and knowledge sharing. Collaborative efforts between governments, universities, and industry stakeholders have become increasingly necessary to create an ecosystem that nurtures engineering talent and encourages research that addresses the continent's pressing needs.

Ultimately, engineering research in Africa stands at a crossroads where it can significantly impact the continent's future. By investing in education and fostering a culture of innovation, African nations can leverage engineering as a catalyst for growth and development, ensuring that local challenges are met with sustainable and effective solutions.

2 HISTORICAL CONTEXT OF ENGINEERING IN AFRICA

The historical evolution of engineering practices in Africa is a tapestry woven from indigenous knowledge, colonial influences, and post-colonial developments. Indigenous engineering methods have existed for centuries, as communities utilized local materials and traditional techniques to construct structures, manage water resources, and create agricultural systems. Notable examples include the ancient pyramids of Egypt, the intricate irrigation systems of the Shona people in present-day Zimbabwe, and the stone houses of the Zulu in South Africa. These practices showcased a deep understanding of the environment and sustainable resource management.

However, the colonial era profoundly altered the engineering landscape. European powers imposed their own engineering standards and practices, often disregarding indigenous techniques. Infrastructure projects such as railways and roads were constructed primarily to facilitate resource extraction and control territories, rather than to benefit local communities. This period also saw the introduction of formal engineering education in Africa, with institutions established by colonial powers aiming to train a small elite rather than fostering broad access to engineering knowledge.

The post-colonial period marked a significant turning point in engineering practices across the continent. Newly independent nations prioritized the need to develop local engineering capacity, leading to the establishment of various engineering institutions. For instance, the University of Nairobi in Kenya and the University of Cape Town in South Africa emerged as key players in engineering education, promoting research that aligned with local needs. Additionally, many African countries began to embrace local content in engineering projects, emphasizing the importance of homegrown solutions and skills transfer.

Noteworthy milestones in engineering education include the formation of the African Engineering Education Association in the early 2000s, which aimed to enhance the quality of engineering programs across the continent. Today, engineering practices in Africa continue to evolve, driven by a blend of indigenous knowledge, modern techniques, and a commitment to addressing the continent's unique challenges.

2.1 Current Trends in Engineering Research

The landscape of engineering research in Africa is witnessing a transformative shift, characterized by a growing focus on renewable energy technologies, sustainable infrastructure, and technology-driven solutions. As nations grapple with the realities of climate change and energy shortages, innovative approaches that harness local resources and expertise are becoming paramount. Countries are increasingly investing in solar, wind, and biomass energy as viable alternatives to traditional fossil fuels, with research institutions leading the charge in developing and implementing these technologies.

Sustainable infrastructure is another area garnering attention in engineering research. The need for resilient urban centers that can withstand environmental stresses has prompted engineers to explore eco-friendly building materials, waste management systems, and efficient transportation networks. For instance, the integration of green building practices and smart city technologies is being researched to enhance urban living while minimizing environmental impacts. These projects often prioritize local materials and labor, ensuring that communities benefit directly from the advancements.

Partnerships between universities and industries are playing a crucial role in driving these trends forward. Collaborative initiatives are emerging, where academic research is aligned with industry needs, fostering a culture of innovation that addresses real-world problems. For example, universities are partnering with local governments and businesses to develop renewable energy projects that not only provide power but also create jobs and stimulate local economies. Such synergies are essential for translating research into practical applications that can improve the quality of life for citizens.

Moreover, technology-driven solutions are being embraced across various sectors, including agriculture, healthcare, and telecommunications. The rise of digital platforms and mobile technologies is facilitating access to information and services, thereby enhancing productivity and efficiency. Research focused on integrating these technologies into engineering practices is crucial for ensuring that Africa does not lag in the global technological landscape.

In summary, the current trends in engineering research within Africa reflect a proactive approach to tackling pressing issues through innovation and collaboration. With a strong emphasis on sustainable practices and local partnerships, the continent is poised to make significant strides in engineering advancements that can lead to long-term development and prosperity.

2.2 Challenges Faced by Engineers in Africa

Engineers in Africa encounter a myriad of challenges that significantly hinder their ability to implement effective solutions to local problems. One of the foremost issues is the lack of funding for engineering projects. According to the African Development Bank, the continent requires approximately \$170 billion annually to address its infrastructure deficits, yet only a fraction of this amount is available. This funding gap severely limits the capacity for large-scale projects and innovations that could transform communities.

Inadequate infrastructure is another pressing concern. Many regions lack essential services such as reliable electricity, clean water, and efficient transportation systems. This deficiency not only hampers engineering efforts but also affects the overall economic development of countries. A case study from Nigeria illustrates this challenge: over 40% of the population lacks reliable access to electricity, which stifles industrial growth and innovation.

Brain drain exacerbates the situation, as skilled engineers often migrate to developed countries in search of better opportunities and working conditions. The World Bank estimates that up to 30% of highly educated professionals from sub-Saharan Africa have relocated abroad. This exodus creates a significant shortage of qualified engineers who can address local challenges and implement sustainable solutions.

Moreover, limited access to advanced technology poses a considerable barrier. Many African engineers lack exposure to cutting-edge tools, software, and methodologies that are essential for modern engineering practices. For instance, while

countries like South Africa and Kenya are making strides in technology adoption, other nations lag behind due to insufficient investment in research and development.

The combination of these challenges creates a complex landscape for engineers in Africa. Tackling these issues requires a concerted effort from governments, educational institutions, and private sectors to invest in infrastructure, attract and retain talent, and provide access to modern technologies. By addressing these critical areas, Africa can unlock the potential of its engineering workforce and drive sustainable development across the continent.

2.3 Case Studies of Successful Engineering Projects

Across Africa, numerous engineering projects have emerged as beacons of success, demonstrating innovative approaches to local challenges while yielding significant community impacts. This section highlights several case studies that exemplify the power of engineering in driving sustainable development.

One notable project is the Kakuma Refugee Camp Solar Microgrid in Kenya. The objective of this initiative was to provide reliable and sustainable energy to the camp, which hosts over 190,000 refugees. Implemented by a consortium of NGOs and energy companies, the methodology involved the installation of solar panels and battery storage systems. The outcome was not only a reduction in reliance on diesel generators but also a significant decrease in energy costs for residents. The microgrid has empowered local businesses, facilitated educational programs, and improved healthcare services, showcasing the potential for renewable energy to transform lives in challenging environments.

In South Africa, the Zola Electrification Project serves as another compelling case study. Launched to address the energy needs of underprivileged communities, the project aimed to electrify informal settlements in the Zola area of Soweto. By employing a community-driven approach, local residents were involved in the planning and implementation phases. This not only ensured that the solutions were tailored to their specific needs but also fostered a sense of ownership. As a result, the project successfully connected thousands of households to the national grid, enhancing safety, education, and economic opportunities in the community [1].

The Water and Sanitation Project in Addis Ababa, Ethiopia, also stands out as a model of engineering success. Faced with a growing urban population and inadequate infrastructure, this project sought to improve access to clean water and sanitation facilities. Utilizing a participatory approach, engineers collaborated with local communities to design and construct water supply systems and sanitation facilities. The outcomes were profound, leading to a significant reduction in waterborne diseases and improved overall health in the community. The project not only addressed immediate needs but also promoted sustainable water management practices that will benefit future generations.

Each of these case studies underscores the pivotal role of engineering in fostering sustainable development across Africa. By employing innovative methodologies and engaging local communities, these projects have demonstrated the potential for engineering solutions to create lasting positive impacts.

3 THE ROLE OF GOVERNMENT AND POLICY IN ENGINEERING

Government policies play a pivotal role in shaping the landscape of engineering research and development. They can either facilitate progress and innovation or hinder it through bureaucratic hurdles and lack of support. In many African countries, the government's commitment to engineering and technology development is reflected in various initiatives aimed at enhancing the sector's capabilities. For instance, investment in educational programs, research grants, and public-private partnerships are critical strategies employed to foster engineering talent and infrastructure.

One significant initiative is the establishment of national engineering councils and regulatory bodies that set standards for engineering practices and education. These organizations often collaborate with universities to ensure that curricula align with industry needs, thereby improving the employability of graduates. Furthermore, governments can incentivize research and development through tax breaks and grants for companies that invest in innovative engineering solutions. This approach not only stimulates local research but also encourages foreign investment, as companies seek to capitalize on the burgeoning engineering sector.

However, many African nations still grapple with policies that inhibit engineering growth. Challenges such as cumbersome regulatory processes, insufficient funding for research institutions, and a lack of infrastructure investment can stifle innovation. For example, engineers often face delays in project approvals due to bureaucratic inefficiencies, which can lead to increased costs and project abandonment. Inadequate funding for engineering education and research also results in a shortage of skilled professionals, further exacerbating the challenges faced by the sector.

Noteworthy examples of successful government initiatives include the African Union's Agenda 2063, which emphasizes the importance of science, technology, and innovation in driving sustainable development. Additionally, various countries have implemented policies aimed at enhancing STEM (Science, Technology, Engineering, and Mathematics) education at all levels, recognizing that a strong foundation in these fields is essential for future engineering advancements.

In summary, the interplay between government policy and engineering development is complex and multifaceted. Effective policies can serve as catalysts for growth, while inadequate or poorly implemented regulations can impede progress. By

prioritizing engineering through supportive policies and investment, governments can significantly enhance the capacity and capability of the engineering sector, ultimately contributing to the continent's development goals.

3.1 Indigenous Knowledge and Technology Integration

The integration of indigenous knowledge systems with modern engineering practices is increasingly recognized as a vital approach to developing sustainable solutions that resonate with local communities. Indigenous knowledge, deeply rooted in cultural traditions and environmental stewardship, offers valuable insights that can enhance contemporary engineering methodologies. By merging these two distinct yet complementary knowledge systems, engineers can create solutions that are not only technically sound but also culturally relevant and ecologically sustainable.

One prominent example of successful integration is the Mokoro Project in Botswana, which focuses on sustainable water management in the Okavango Delta. Local communities possess extensive knowledge about the hydrology of the delta, traditionally using their understanding of seasonal changes and indigenous plant species to manage water resources. Engineers working alongside these communities have combined this traditional expertise with modern hydrological modeling techniques to develop a comprehensive water management plan. This collaboration has resulted in improved water conservation practices that respect local customs while addressing the challenges posed by climate change [2].

Another noteworthy case is the Indigenous Forestry and Engineering Collaboration in Canada, where traditional ecological knowledge has been integrated into forest management practices. Indigenous communities have long employed sustainable methods of resource extraction that consider biodiversity and ecosystem health. By partnering with engineers and environmental scientists, these communities have developed innovative timber harvesting practices that reduce environmental impact while enhancing economic opportunities. This synergy not only protects the forest ecosystem but also revitalizes indigenous economies, demonstrating a successful model for integrating traditional knowledge with modern engineering.

In the realm of renewable energy, the Sustainable Energy for All (SE4ALL) initiative showcases how indigenous knowledge can play a crucial role in the deployment of solar energy solutions. In various regions of Africa, local populations have utilized their understanding of sun patterns and resource availability to design solar energy systems that are tailored to their specific needs. Engineers collaborating with these communities have been able to create more efficient energy solutions that align with cultural practices and local preferences, ultimately leading to increased adoption and satisfaction.

These examples illustrate the importance of integrating indigenous knowledge systems with contemporary engineering practices. Such collaborations not only yield innovative solutions but also empower local communities, fostering a sense of ownership and stewardship over their resources. By valuing and incorporating indigenous knowledge, the engineering field can enhance its relevance and effectiveness in addressing the unique challenges faced by diverse populations across Africa and beyond.

3.2 Future Prospects for Engineering Research

The future of engineering research in Africa is poised for significant transformation, particularly with the advent of emerging technologies such as artificial intelligence (AI), robotics, and bioengineering. As these technologies evolve, they present unique opportunities for addressing the continent's pressing challenges, ranging from healthcare accessibility to infrastructure development and environmental sustainability.

Artificial intelligence is set to revolutionize various sectors in Africa. From predictive analytics in agriculture that can enhance crop yields to AI-driven healthcare applications improving diagnostics and patient care, the potential is immense. Governments and research institutions are increasingly investing in AI training programs, creating a workforce capable of harnessing this technology. Moreover, AI can facilitate data-driven decision-making in urban planning, resource management, and disaster response, making it a crucial tool for sustainable development.

Robotics also holds promise for engineering research in Africa, particularly in sectors where labor shortages exist. Automated systems can optimize manufacturing processes and improve productivity across industries, such as mining and agriculture. Emerging initiatives, like robotics competitions in schools, are fostering interest in this field among young engineers. Collaborations with international partners can further enhance research in robotics, providing access to advanced technologies and expertise [3].

Bioengineering is another frontier with vast potential. With Africa's rich biodiversity, bioengineering research can lead to innovative solutions tailored to local needs, such as developing drought-resistant crops or affordable medical devices. The continent's unique ecosystems offer a wealth of biological resources that can be harnessed for sustainable practices, contributing to global efforts in combating climate change and promoting health equity.

International collaboration will be pivotal in advancing engineering research in Africa. Partnerships with universities and research institutions worldwide can facilitate knowledge exchange, technology transfer, and funding opportunities. Collaborative projects can address shared challenges, such as climate change adaptation, and leverage diverse expertise to

create innovative solutions. By fostering a culture of collaboration, Africa can position itself as a leader in engineering research, driving sustainable development and enhancing its global competitiveness.

3.3 Comparative Analysis with Other Regions

The comparative analysis of engineering research capacity in Africa versus regions such as Europe and Asia reveals significant disparities in performance metrics such as publications, funding, and research output. While Africa is experiencing a gradual increase in research activity, particularly in sectors like renewable energy and sustainable development, it still lags behind more established regions.

In Europe, engineering research is characterized by robust funding mechanisms and a high volume of publications. The European Union invests heavily in research and innovation through programs like Horizon Europe, which allocates billions of euros to foster technological advancements and collaborations. This investment results in a wealth of high-impact publications, with European countries leading in various engineering disciplines, including civil, mechanical, and environmental engineering. The emphasis on interdisciplinary research and international collaboration further amplifies the research output in Europe.

In contrast, Africa faces challenges related to limited funding for research initiatives. Many African nations allocate only a small percentage of their GDP to research and development, which impacts the capacity of local universities and research institutions to produce high-quality engineering research. Despite the enthusiasm of young engineers and researchers, the lack of adequate resources often hampers their ability to publish findings in reputable journals or to participate in global research networks [4].

Asia presents an intriguing case, with countries like China and India rapidly advancing their engineering research capabilities. China, in particular, has made substantial investments in infrastructure and technology, leading to a significant increase in research output and publications. The country's focus on innovation and technology transfer has positioned it as a global leader in engineering, surpassing many Western nations in various metrics. India, with its growing technology sector, is also seeing an increase in engineering research, particularly in software and telecommunications.

While Africa is beginning to harness local knowledge and cultivate partnerships between academia, industry, and government, it remains essential to address the funding gaps and infrastructure deficits that limit research capacity. By learning from the successful frameworks established in Europe and Asia, African nations can develop targeted strategies to enhance their engineering research landscape, ultimately contributing to sustainable development and economic growth.

3.4 Education and Capacity Building

Education plays a pivotal role in developing a skilled engineering workforce in Africa, which is essential for addressing the continent's unique challenges and harnessing its vast potential. To cultivate an effective engineering workforce, it is crucial to not only enhance the quality of engineering curricula but also foster research skill development among students. A robust educational framework can empower future engineers to innovate and implement sustainable solutions that directly benefit their communities [5].

One of the primary recommendations for strengthening engineering curricula is the integration of practical, hands-on learning experiences. Curricula should be designed to include project-based learning, internships, and collaborations with local industries. This approach not only equips students with theoretical knowledge but also provides them with practical skills and real-world exposure necessary for their professional growth. By engaging with local engineering challenges, students can apply their learning in meaningful ways, fostering a sense of ownership and responsibility towards their communities.

Furthermore, curricula should emphasize interdisciplinary learning, combining engineering principles with subjects such as environmental science, economics, and social studies. This holistic approach can help future engineers develop a broader perspective on the implications of their work and encourage innovative solutions that address socio-economic and environmental issues. Institutions should also focus on incorporating emerging technologies, such as artificial intelligence and renewable energy systems, into their programs to ensure that students are well-versed in the latest advancements [6].

In addition to curriculum development, fostering research skill development is vital. Universities should provide opportunities for undergraduate and graduate students to engage in research projects, ideally in collaboration with faculty members and industry partners. By encouraging students to participate in research, institutions can nurture critical thinking, problem-solving skills, and creativity. This not only enhances the students' educational experience but also contributes to the advancement of engineering knowledge in Africa.

Ultimately, investing in education and capacity building is essential for cultivating a skilled engineering workforce capable of driving sustainable development across the continent. By enhancing engineering curricula and fostering research skill development, African nations can empower their youth to become innovative leaders who can effectively tackle local challenges.

3.5 Role of International Collaboration

International collaboration plays a crucial role in advancing engineering research in Africa, significantly enhancing research capacity and fostering innovation. Through partnerships with universities, research institutions, and industries around the globe, African nations can leverage external expertise, funding, and technology, which are often scarce locally. Such collaborations are particularly essential in addressing complex engineering challenges, including infrastructure development, renewable energy adoption, and sustainable resource management.

One notable example of successful international collaboration is the African Research Universities Alliance (ARUA), which brings together top research universities across Africa to collaborate on addressing the continent's pressing challenges. ARUA has established partnerships with leading global institutions, facilitating joint research projects and capacity-building initiatives. Through these partnerships, African researchers gain access to cutting-edge research facilities and resources, fostering an environment conducive to innovative engineering solutions [7].

Another impactful program is the Engineering for Development (E4D) initiative, which focuses on enhancing engineering education and research capacity in developing countries, including several African nations. By partnering with universities in Europe and North America, E4D provides training, funding, and resources to support engineering projects that directly address local needs. This initiative has successfully contributed to building a skilled workforce capable of implementing sustainable engineering solutions in various sectors, such as water management and renewable energy.

Furthermore, international collaborations often lead to knowledge exchange and skills transfer, empowering local engineers and researchers. Programs such as the Global Innovation through Science and Technology (GIST), supported by the U.S. Department of State, encourage collaboration between American and African innovators. GIST fosters entrepreneurship and technological innovation, enhancing the capacity of local teams to develop solutions tailored to regional challenges.

In summary, international collaboration is vital for advancing engineering research in Africa. By fostering partnerships that leverage global expertise and resources, African nations can enhance their research capacity, drive technological innovation, and ultimately contribute to sustainable development across the continent [8].

4 ETHICS AND SUSTAINABILITY IN ENGINEERING

In the context of engineering practice in Africa, ethical considerations and sustainability issues are increasingly central to decision-making processes. As the continent faces unique socio-economic challenges, engineers must navigate a complex landscape that includes resource scarcity, environmental degradation, and the need for inclusive development. The ethical dimension of engineering encompasses accountability to local communities, respect for cultural values, and the pursuit of equitable solutions that foster long-term sustainability [9].

One significant ethical consideration is the impact of engineering projects on the environment and local communities. Engineers are tasked with designing solutions that not only address immediate needs but also consider the long-term consequences of their actions. For instance, infrastructure projects must evaluate potential environmental impacts, such as habitat destruction or water pollution, and strive to incorporate sustainable practices that mitigate these effects. It is crucial for engineers to embrace a holistic approach that prioritizes ecological integrity while delivering essential services.

Frameworks for ensuring responsible engineering decisions include adherence to established ethical guidelines and standards. Organizations such as the International Federation of Consulting Engineers (FIDIC) and the American Society of Civil Engineers (ASCE) provide codes of ethics that emphasize integrity, transparency, and social responsibility. Additionally, the integration of sustainability principles into engineering education equips future professionals with the knowledge to make informed decisions that align with ethical standards.

Moreover, stakeholder engagement is vital in the engineering process, allowing for diverse perspectives to inform project planning and execution. By actively involving local communities in decision-making, engineers can better understand the specific needs and concerns of those affected by their work, fostering trust and promoting ethical accountability.

To promote sustainability, engineers should also consider the lifecycle of projects, emphasizing renewable resources, energy efficiency, and waste reduction. The implementation of sustainable engineering practices not only addresses urgent infrastructure needs but also contributes to the broader goal of sustainable development, ensuring that future generations can thrive within a balanced ecological framework [10].

5 CONCLUSION

In summary, this paper has explored the critical role that engineering research plays in driving Africa's growth and development. Through various sections, we have highlighted the unique challenges faced by the continent, including inadequate infrastructure, limited access to education, and socio-economic disparities. Despite these hurdles, engineering research holds immense potential to create innovative solutions tailored to local contexts, fostering sustainable progress.

We've seen that a collaborative approach among governments, academia, and industry stakeholders is essential for cultivating an environment conducive to engineering advancements. Emphasizing local content in engineering projects not only stimulates economic growth but also promotes skills transfer, capacity building, and community empowerment. The historical context of engineering in Africa reveals a legacy of both indigenous practices and colonial influences, which continue to shape the current landscape and inform future initiatives.

Current trends reflect a shift towards sustainable energy solutions, eco-friendly infrastructure, and technology-driven approaches, showcasing a proactive response to pressing issues such as climate change and urbanization. However, challenges such as funding limitations and the need for enhanced educational frameworks must be addressed to unlock the full potential of engineering research.

As we look to the future, the landscape of engineering in Africa is poised for transformation. By investing in education, fostering international collaborations, and adhering to ethical and sustainable practices, the continent can harness its engineering capabilities to drive meaningful development. The journey ahead presents a unique opportunity for African nations to emerge as leaders in engineering innovation, ultimately improving the quality of life for their citizens and contributing to global advancements [11].

COMPETING INTERESTS

The authors have no relevant financial or non-financial interests to disclose.

REFERENCES

- [1] World Bank. Africa's Infrastructure: A Time for Transformation. World Bank, 2021. <https://www.worldbank.org/en/region/afr/publication/africas-infrastructure-a-time-for-transformation>.
- [2] United Nations Development Programme (UNDP). Human Development Report 2021: Sustainable Development Goals and the Future We Want. UNDP, 2021. <https://hdr.undp.org/en/2021-report>.
- [3] Nyang'oro J, Oduor J. The Role of Local Knowledge in Engineering Solutions: Case Studies from East Africa. *Journal of Applied Engineering Science*, 2020, 18(2): 132-145. DOI: <https://doi.org/10.5937/jaes0-27005>.
- [4] Muniyiri R, Chikandi P. Challenges in Engineering Education in Kenya: A Case Study. *International Journal of Engineering Education*, 2021, 37(3): 1014-1025. <https://www.ijee.ie>.
- [5] Kumar A, Zulu L. Sustainable Engineering Practices in Africa: A Review of Current Trends. *African Journal of Engineering Research*, 2023, 8(1): 67-79. DOI: <https://doi.org/10.22034/ajer.2023.01.05>.
- [6] International Federation of Consulting Engineers (FIDIC). FIDIC Code of Ethics. FIDIC, 2019. <https://fidic.org/ethics>.
- [7] Global Innovation through Science and Technology (GIST). Fostering Tech Entrepreneurship in Africa. U.S. Department of State, 2021. <https://www.gistnetwork.org>.
- [8] Engineering for Development (E4D). Enhancing Engineering Education and Research Capacity in Developing Countries. E4D Report, 2019. <https://www.e4d.org/report>.
- [9] African Research Universities Alliance (ARUA). Strengthening Research Capacity in African Universities. ARUA, 2020. <https://arua.org/wp-content/uploads/2020/02/ARUA-Strategic-Plan-2020.pdf>.
- [10] African Development Bank. African Economic Outlook 2021: Financing for a Sustainable Recovery. African Development Bank Group, 2021. <https://www.afdb.org/en/documents/african-economic-outlook-2021>.
- [11] Akinyemi A. Engineering Education in Africa: Challenges and Opportunities. *Journal of Engineering Education*, 2022, 111(4): 543-558. DOI: <https://doi.org/10.1002/jee.20374>.

SIMULATION ANALYSIS OF THE DYNAMIC RESPONSE CHARACTERISTICS OF A TYPICAL GOLD MINE TAILING DAM UNDER THE COUPLING OF EARTHQUAKE AND RAINFALL

PengJin Liu¹, Jie Wang², JiaFa Du¹, JianFei Sun^{2*}, YongLiang Zhang², HongWei Mu²

¹Qinghai Shanjin Mining Co. Ltd., Haixi 817000, Qinghai, China.

²School of Mechanical and Automotive Engineering, Qingdao University of Technology, Qingdao 266000, Shandong, China.

Corresponding Author: JianFei Sun, Email: sunjianfei@qut.edu.cn

Abstract: When an earthquake and precipitation coincide, there is a considerable increase in the danger of tailing dam instability. This work chooses a typical metal mine tailing dam in the Jiaodong area and numerically models the danger of tailing dam instability under the coupling of earthquake and rainfall. The simulation is based on the genuine demand for efficient warning of tailing dam instability under extreme natural conditions. The analysis focuses on the tailing dam's displacement and instability risk in the event of a strong earthquake, intense rainfall, or a combination of the two. According to the simulation results, the middle and upper portions of the accumulation dam exhibit the largest horizontal displacement of the tailing dam, while the rainfall coupling condition exhibits the maximum horizontal displacement of the dam body. According to the study, there is a higher risk of dam failure in the upper-middle region of the tailing dam, and in two extremely harsh natural settings, an earthquake will have a more significant effect on the stability of the dam. The study's findings offer a solid scientific foundation for emergency planning and for monitoring and warning of tailing dams during severe natural disasters.

Keywords: Tailing dam; Rainfall and earthquake; Coupling action; Dynamic response

1 INTRODUCTION

One source of man-made debris flow hazards with a high potential energy is a tailings dam. Tailings dam failures have become more common in recent years [1]. The dam is vulnerable to a number of force sources during regular operation, and it is also susceptible to dam failure due to natural events like earthquakes and rainfall, which might have disastrous effects on the environment, property, and human lives. Consequently, it is crucial to research the integrity of tailings dams under extreme natural disturbances from a practical standpoint.

Many studies have been conducted on the stability of tailing dams from various angles, with a primary emphasis on seismic and rainy circumstances. Terzaghi and Michalowski used the proposed static force method to study seismic conditions [2-3], draw the slope stability diagram, and calculate the slope safety coefficient; In order to assess the tailing dam's dynamic stability, Haper and colleagues used the residual strength theory by using FLAC3D software [4]; Yasuda and colleagues conducted tests using a shaking table model [5], talked about the phenomena of residual deformation brought on by soil liquefaction, and suggested a technique for horizontal deformation prediction; In addition, Towhata and colleagues extended the mathematical equation for the lateral deformation of a laying liquefied soil layer and performed shaking table tests [6]; Seid-Karbasi M and others demonstrated that soil liquefaction significantly increases the risk of tailing dam instability [26]; R.S. Jakka and others investigated the stability of tailing dam constructed by upstream and downstream methods under different seismic wave conditions [4]. The study's findings demonstrated that the stability of tailing dam is affected by a variety of conditions, including the method of dam construction; Debarghya and colleagues simulated and examined the impact of soil liquefaction on the stability of tailing dams [3]; the findings demonstrated a considerable increase in the impact of soil liquefaction on tailing dam stability; Chakrabrabhan and others conducted numerical simulations of side slopes under seismic conditions [2], and explored the effect of different rock qualities and footings on the side slope stability; S. Srikrishnan and others carried out numerical simulations of side slopes under seismic conditions to investigate the effect of different rock qualities and footings on the slope stability [10]; B. Xu and colleagues used the limit equilibrium method to determine the tailing dam's liquefaction zone under dynamic loading conditions and came to the conclusion that the tailing dam was still stable under seismic conditions [11]; Strong earthquakes have a significant impact on the stability of tailings dams, according to research by Mahdi Naeini and others using SIGMA/W software to investigate the stress-pore pressure coupling of the dams under dynamic loading conditions [12]; Takaji used the Newmark method to determine whether seismic energy would cause slope landslides and to calculate the slope displacements following the occurrence of landslides [8].

Alonso and colleagues computed the two-site saturated seepage field in the rainy circumstances investigation [14], accounting for real fluctuations in air pressure; Sammori and others used the Galerkin method to analyze the factors affecting slope stability and deduced the temporary seepage state of the slope through experiments [15]. The study's

findings indicated that the infiltration coefficient, the slope's length, and the thickness of the soil layer all had an impact on the stability of the slope. Fledlund examined slope stability under heavy rainfall conditions and summarized the law of rainfall duration on the pore water pressure [16]; Muntohar conducted a study that determined the sliding time and damage depth of shallow slope instability brought on by rainfall [17]; Zandarín used a force-water coupled finite element model to simulate and analyze the dam [18], and the results indicated that the capillary phenomenon of capillary water had a significant impact on the dam's stability; Ormann conducted a finite element analysis of pore water pressure during the damming period [19], and the study showed that the stability of the tailing dam decreased with an increase in pore water pressure; N.G. and others simulated and examined the stability of rainfall slopes using finite element software [20]; Wang and others conducted experimental studies on tailing dam breaching under rainfall conditions, and generalized and summarized the increase in the length of the infiltration line with the increase in the length of the rainfall [21]. Tarek and others generalized the probability distribution function of the safety factor of the tailing dam by analyzing three factors: permeability coefficient, angle of internal friction, and cohesion [5]; An experimental research of tailings dam failure during rainfall was carried out by Wang and colleagues [21], who also described the changing rule of the infiltration line with the increase of rainfall duration; In experiments on hydraulic erosion on slopes subjected to rainfall, Sun and colleagues demonstrated that rainfall infiltration is the primary cause of the decline in slope stability [23]; Liu and others demonstrated that rainfall infiltration increases the tailing dam's pore water pressure [23], which impacts the stability of the dam; Rong Gui and others established a hydraulic deposition model to experimentally investigate the effects of rainfall infiltration on the stability of the dam [4].

The studies mentioned above primarily concentrate on the impact of a single factor on the stability of the tailing dam, rarely take into account the risk of instability of the tailing dam under extreme earthquake and rainfall coupling conditions, and do not offer recommendations for monitoring and warning of instability under such conditions. Based on this, tailing dam destabilization under high intensity earthquake, heavy rainfall, and the superposition of the two is studied through numerical simulation in order to reveal, study the risk of tailing dam destabilization under high intensity environments, and provide guidance on monitoring and warning of tailing dam destabilization as well as the creation of emergency response plans.

2 PROJECT OVERVIEW AND MODEL CONSTRUCTION

2.1 Overview of the Project

In this study, a typical metal mine tailing dam in Jiaodong, Shandong province, is chosen for numerical simulation analysis. It is a valley-type tailing reservoir with a total capacity of $2.2455 \times 10^6 \text{ m}^3$. In accordance with the Safety Technical Regulations for Tailing Reservoirs (AQ2006-2005), it is classified as a fourth-class tailing reservoir. With a slope ratio of 1:3, a maximum dam height of 12 meters, and a total storage capacity of $1.782 \times 10^5 \text{ m}^3$, the initial dam is a crushed rock-fill dam (Figure 1).



Figure 1 Tailing Dam Site

Strong earthquakes could happen in this location, according to studies of the regional geological structure and previous seismic data. The location falls within Group II of the Code for Seismic Design of Buildings (GB50011-2010), which has a seismic intensity of VII and a design fundamental seismic acceleration of $0.15g$.

The yearly average for both temperature and precipitation is 11.8°C and 637 mm, respectively. The rainy season typically begins in late June and lasts until early September. Precipitation at this time of year makes up around 75% of the total yearly amount and is characterized by intense, concentrated downpours with a maximum hourly precipitation of more than 50mm.

2.2 Model Construction and Boundary Condition Setting

FLAC3D software was selected for numerical simulation analysis in this paper because it can better handle the complicated subject of geotechnical bodies and can more intuitively demonstrate the emergence and development of large-model instability damage under complex multi-case settings. The more practical Rhino 7 program is utilized for modeling and meshing due to the intricacy of FLAC3D's built-in modeling. The model is then imported into FLAC3D for further study.

2.3 Modeling and Meshing

Based on the tailing dam's real dimensions—550 m for length, 300 m for breadth, and 100 m for height—a simplified model was created. The profile was segmented into seven areas based on the materials' mechanical and physical characteristics.

The Y-axis represents the vertical dam direction, the X-axis the direction along the dam strike, and the Z-axis the opposite direction of gravity. Figure 2 depicts the tailing dam's three-dimensional stability simulation model, which has 9466 zones and 6630 gridpoints.

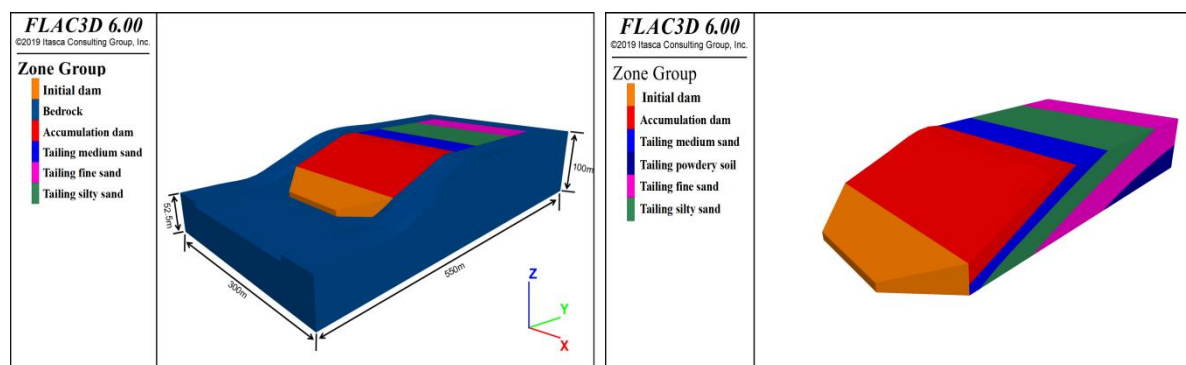


Figure 2 Numerical Calculation Model Diagram (Left: Numerical Modeling Diagram; Right: Reservoir Capacity Modeling Diagram)

2.4 Boundary Condition Setting

The bottom of the bedrock is subject to predetermined limits while defining the static field boundary conditions; the remaining direction is left free to tail in the tailing dam as a subsequent accumulation on the bedrock. The water table burial depth is set at eight meters in reference to the actual value of the engineering monitoring data.

In order to simulate the seismic condition, the static boundary condition is applied to the model's bedrock, the free boundary is placed around the model, and the static boundary condition is released to place the model in a free state.

The top plane of the reservoir area is designated as the permeable boundary, the bottom and two sides of the model are designated as the impermeable boundary, and the top plane is designated as the contact surface between rainwater and the dam body.

Determination of the intrinsic model and computational parameters:

The mohr-coulomb model was used for this tailing dam stability simulation because it primarily depicts loose and cemented granular bulk materials, and tailing sand has the properties of loose cementation. The density of the geotechnical body, the pertinent modulus of elasticity, the geotechnical body's strength characteristics, and poisson's ratio are the parameters that make up this model. The parameters used in the numerical simulation are all the values of the engineering field sampling experiment, which is shown in Table 1. The permeability coefficient in the table will also be used for numerical simulation of seepage during rainfall.

Table 1 Calculation Parameters

Ground Level	Density P(g/cm ³)	Friction Ψ(°)	Cohesion C(kPa)	Modulus of elasticity E(MPa)	Poisson	Permeability K(cm/s)
Tailing medium sand	1830	33	35	77	0.32	8.5×10 ⁻⁶
Tailing silty sand	1870	31	52	79	0.32	5.7×10 ⁻⁶
Tailing fine sand	1900	30	58	95	0.32	2.9×10 ⁻⁶
Tailing powdery soil	1940	29	65	110	0.32	1×10 ⁻⁶
Bedrock	2700	38	10000	10000	0.33	4.5×10 ⁻⁷
Initial dam	2400	36	1000	5000	0.33	6.5×10 ⁻⁷

Accumulation dam	1890	31	550	80	0.33	5.5×10^{-6}
------------------	------	----	-----	----	------	----------------------

2.5 Input of Dynamic Loads

The "Code for Seismic Design of Buildings" (GB50011-2010) states that the tailing dam area's site characteristic period value is $T_g = 0.30$ s and the initial dam site's site characteristic period value is $T_g = 0.40$ s. These values are based on the project's building site category and the city's seismic grouping as group II.

Wenchuan wave is used in the simulation because the seismic intensity of the region where the tailing dam is located is grade VII. As a result, when the seismic wave is applied, the intensity of Wenchuan wave is adjusted to grade VII, and the corrected peak velocity is consistent with the peak velocity interval of grade VII earthquakes. As a result, the seismic wave can be used for the numerical simulation of subsequent grade VII earthquakes. Figure 3 depicts the seismic time curve following baseline correction. The earthquake lasted for a total of 16 seconds.

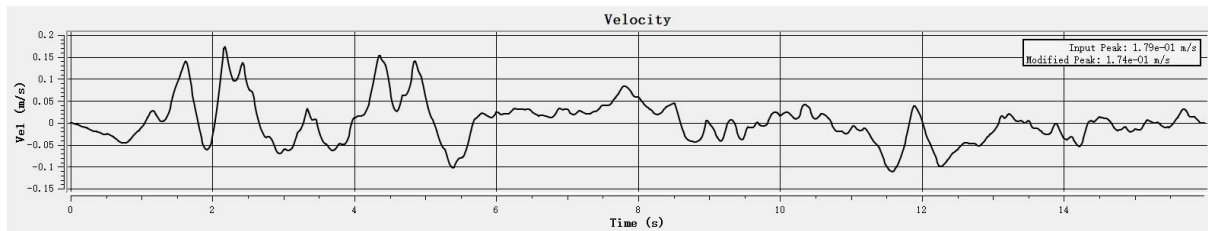


Figure 3 Seismic Velocity Time Course Profile after Filtering and Baseline Correction

2.6 Simulation Program

Stability simulations were created for the following four scenarios to examine the impacts of earthquake, rainfall, and their coupling on the stability of the tailing dam: 1) The static field condition; 2) The earthquake condition; 3) The rainfall condition; and 4) The coupling of the earthquake and rainfall.

Specific simulation programs are set up as follows:

- (1) The initial total stress field, displacement field, and safety factor of the dam body are simulated in the static field condition with only the gravitational field applied, and the actual monitoring values are compared to make sure the ensuing simulation is accurate, which is of reference significance.
- (2) Use the static method to determine the safety coefficient following an earthquake and the method of applying filtered and baseline-corrected ground vibration loads to the bottom of the tailing dam to determine the dynamic response of the dam body after the earthquake and perform the liquefaction analysis.
- (3) To examine the dynamic reaction under the rainfall environment, a downpour with an imposed rainfall intensity of 50 mm/h is utilized, and the imposed time is 2, 4, 6, and 8 hours, respectively. This is done with reference to the actual rainfall in the local area.
- (4) In the coupled case, a 16-second earthquake is applied first, followed by 50 mm/h rainstorms for 2, 4, 6, and 8 hours. This is done to investigate the dam's dynamic response to post-earthquake rainfall conditions as well as the distribution law of the dam instability region. This is because most earthquakes are accompanied by extended periods of heavy rainfall.

3 ANALYSIS OF SIMULATION RESULTS

Figure 4 depicts the Z direction total stress and pore-pressure cross section cloud of the tailing dam in the scenario where the gravity field is the only applied force.

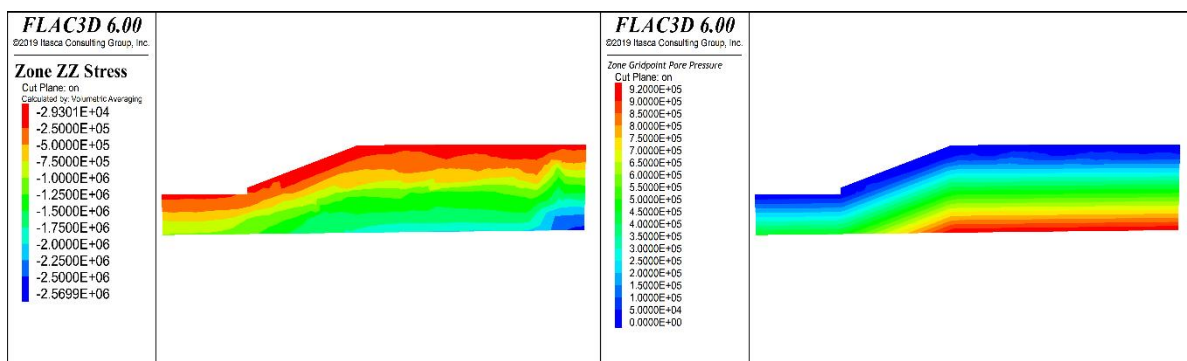


Figure 4 Total Stress and Pore-Pressure Cloud Diagram (Left: Z Direction Total Stress Cloud; Right: Initial Pore-Pressure Cloud)

The cloud map reveals:

- (1) The maximum value of the total stress cloud map of the tailings dam is about 2.57MPa, and the maximum value of pore-pressure is 0.92Mpa, and their distribution pattern is basically the same. The maximum values are located at the bottom of the dam.
- (2) Since the tailing dam's primary stress is compressive stress, as indicated by its total stress map, there won't be any visible tensile damage zone while the tailing dam is in a static field condition.
- (3) Under static field conditions, the tailing dam's bottom region is where its maximum total stress is distributed. The distribution of the stress is essentially parallel to that of the terrain, which is consistent with the depositional properties of the soil body.

3.1 Displacement Field Analysis

Figure 5 depicts the displacement cloud in the Y-axis direction and the Z-axis direction when only the gravity field is used.

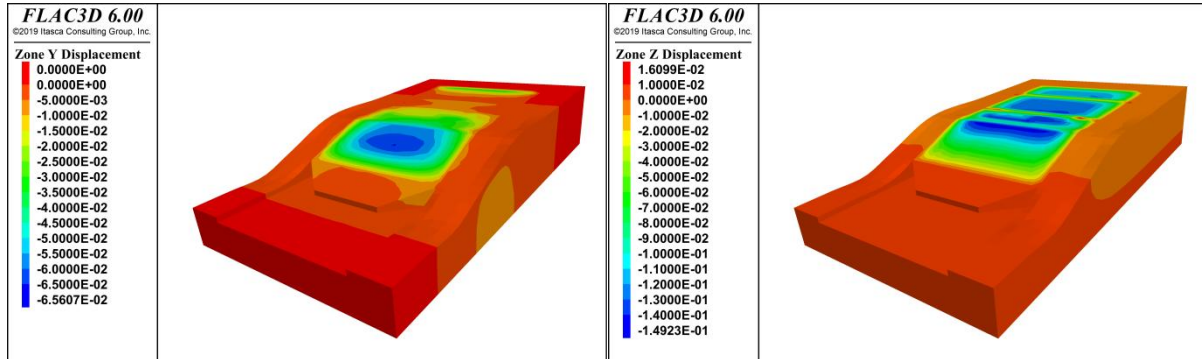


Figure 5 Overall Displacement Cloud (Left:Y-Axis Displacement Map; Right: Z-Axis Displacement Map)

The maximum displacement of the tailing dam in the vertical direction, which is shown in Fig. 5(Left), is concentrated in the middle of the tailing accumulation slope and is approximately 6.56 cm. The surface displacement of the reservoir area is also greater than the internal displacement of the reservoir area. This demonstrates that the displacement distribution pattern in the vertical dam direction is characterized by a surface displacement that is greater than an internal displacement. The accumulation dam's slope, where the biggest displacement is located, suggests that this area is less stable than others because of its lower stability.

According to Figure 5 (Right), the dry beach area and the accumulation slope are where the tailing dam's maximum displacement in the vertical direction, which is approximately 14.9 cm, is concentrated. Greater than the internal displacement of the reservoir area is the surface displacement of the reservoir area.

For the analysis of the displacement cloud, the cross-section at the center point (X=-150m) was further chosen, and the profile displacement cloud is presented in Figure 6:

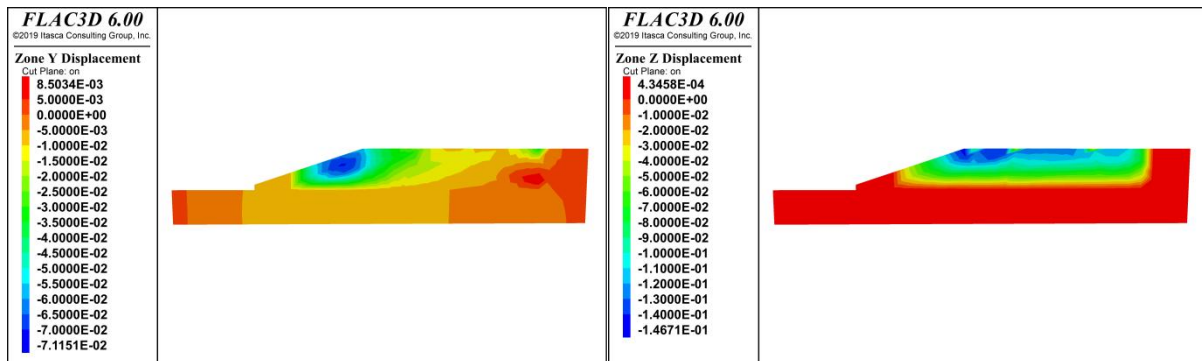


Figure 6 Displacement Cloud Map of the Profile(Left: Y-Axis Cross-Section Displacement Map; Right: Z-Axis Cross-Section Displacement Map)

As can be seen in Figure 6, the displacement distribution pattern in the Y-axis and Z-axis directions of the profile is the same as that of the whole, and the maximum displacement is concentrated on the slope surface and the top of the slope, and the displacement distribution shows the pattern of large surface and small internal displacement. In order to ensure that the simulation can truly characterize the actual displacement and instability, the simulation results were compared with the on-site displacement meter monitoring data, and the difference was in millimeters, which indicates that the model is in line with the actual site.

3.2 Three-Dimensional Dynamic Stability Calculation Results and Analysis

Stability analysis of dam under seismic conditions:

3.2.1 Displacement field analysis

The post-seismic displacement cloud of the tailing dam is shown in Figure 7:

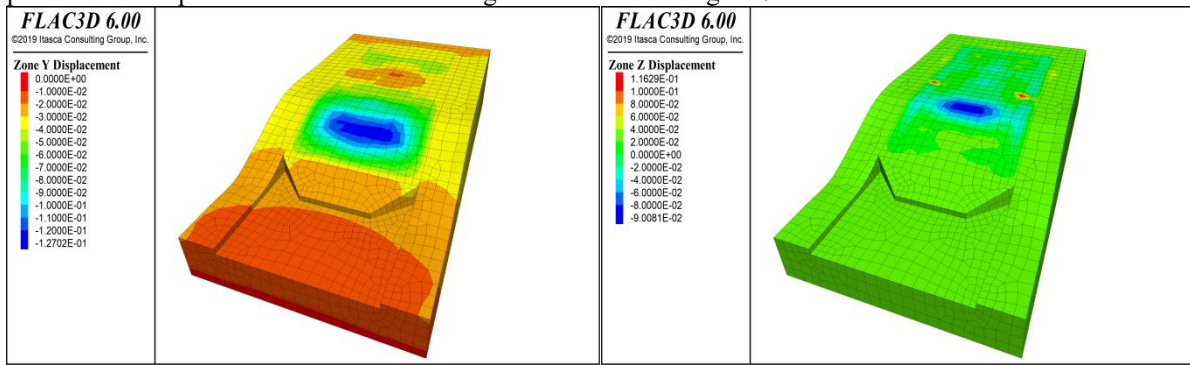


Figure 7 Overall Displacement(Left: Y-Axis Displacement Map; Right: Z-Axis Displacement Map)

The highest value of the tailing dam under seismic loading is shown in Figure 7 (Left), and it is approximately 12.7 cm in the vertical dam direction. The surface displacement of the reservoir area is also shown, and it is more than the internal displacement of the reservoir area. The initial dam's residual deformation is minimal, however the residual deformation of the accumulation dam and the dam body is substantial, showing that this position is less stable than other places.

Figure 7 (Right) illustrates that the highest vertical displacement of the tailing dam, which is approximately 9 cm, is located at the intersection of the dry beach and the stockpile slope.

Figure 8 depicts the displacement map of the profile, which was intercepted in the center of the pile slope (X=-150m) for analysis.

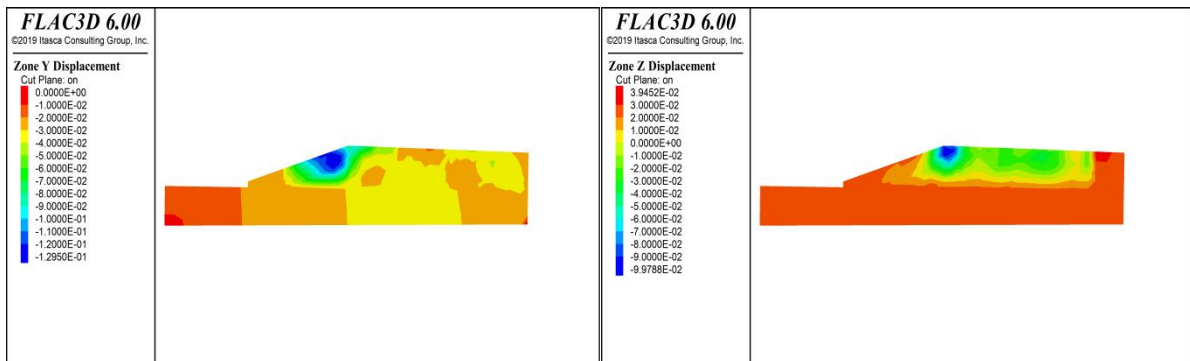


Figure 8 Cross-Sectional Displacement Cloud (Left: Y-Axis Cross-Section Displacement Cloud; Right: Z-Axis Cross-Section Displacement Cloud)

The maximum displacement is centered on the slope surface and the top of the pile-up slope, as seen in Figure 8. This distribution pattern of large surface and small interior is consistent with the only distribution pattern of the static field, and it further suggests that the middle-upper part of the pile-up slope is where the maximum displacement is distributed.

3.2.2 Judgment of liquefaction

(1) Judgment basis

In this study, we employ the excessive static pore-pressure ratio cloud diagram for liquefaction analysis, which is given the following definition by 3D numerical calculations(Yumin, 2013):

$$r_u = 1 - \frac{\sigma'_1 + \sigma'_2 + \sigma'_3}{\sigma_{10} + \sigma_{20} + \sigma_{30}} \quad \#(\text{Eq 1}) \quad (1)$$

σ'_{j0} ($j = 1, 2, 3$) Three effective stress components of the unit before the dynamic calculation;

σ'_j ($j = 1, 2, 3$) Three effective stress components of the cell during the dynamic calculation.

The magnitude of the degree of liquefaction can be determined by the super-porous pressure ratio, and its criteria are as follows: $r_u=1$ denotes total liquefaction, and $0.7 \leq r_u < 1$ denotes near liquefaction. In this study, we use fish language to write a program to calculate the excessive static pore-pressure ratio, generate the excessive static pore-pressure ratio cloud map, and then judge whether the tailings dam liquefaction.

(2) Liquefaction analysis of tailing dam

To ascertain whether soil liquefaction occurs in the reservoir region due to ground vibration load, the cloud diagram of super-porous pressure ratio in the reservoir area is examined. The cloud diagram of super-porous pressure ratio is illustrated in Figure 9:

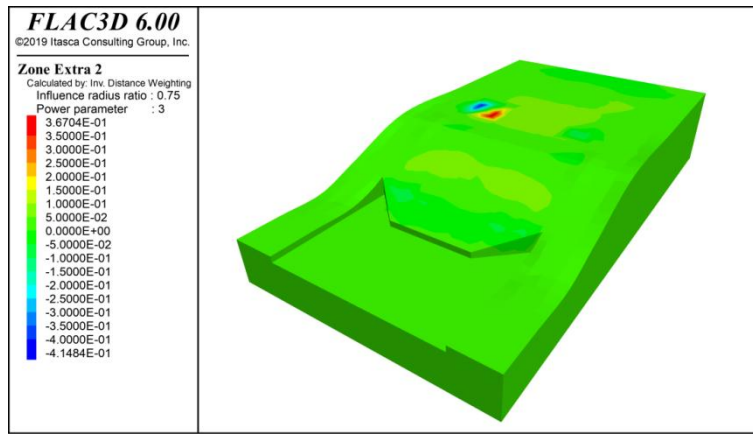


Figure 9 Cloud Diagram of Super-Porous Pressure Ratio

The tailing dam did not liquefy as a result of the earthquake, as can be seen from the study of the figure, which shows that the super-porous pressure ratios are minor after the earthquake and all locations are less than 0.7.

3.3 Dam Stability Analysis under Rainfall Conditions

The top of the tailings dam is selected as the precipitation infiltration surface, and the soil permeability coefficients of each layer are shown in Table 1 and Figure 10 displays the rainfall in the tailing dam displacement cloud maps at 2 hours, 4 hours, 6 hours, and 8 hours.

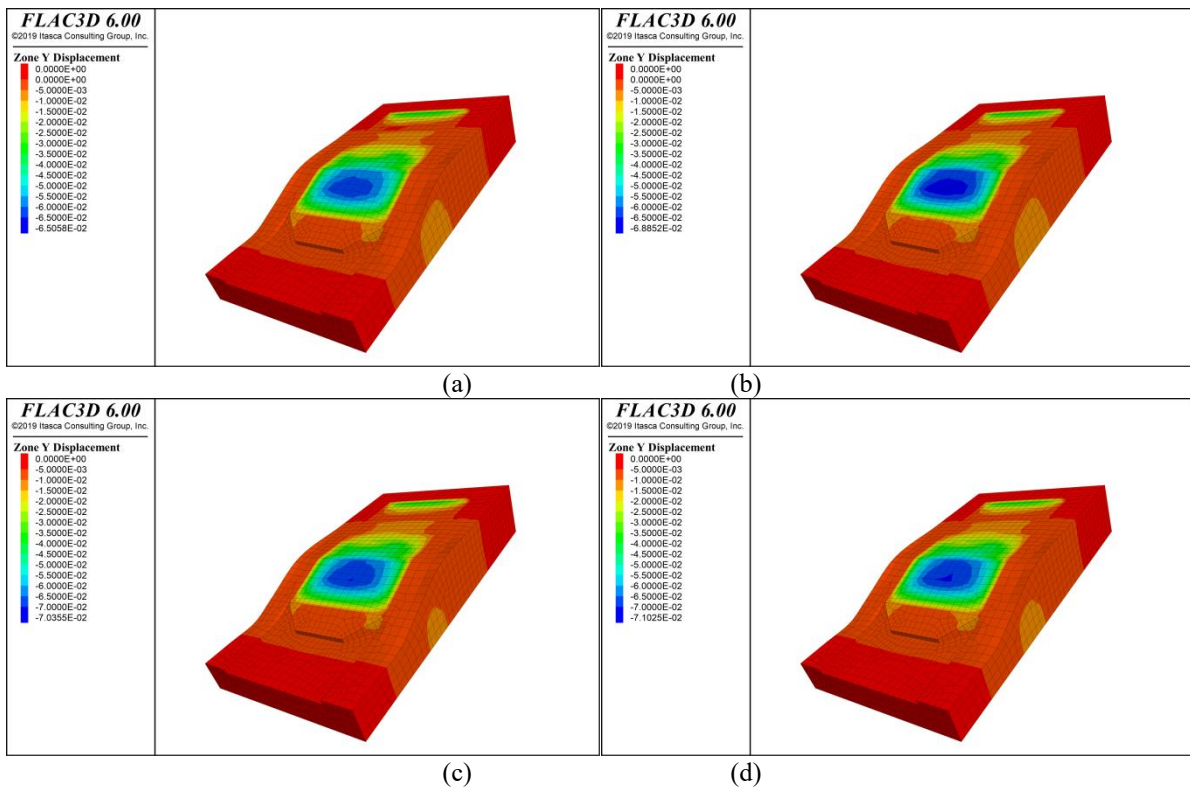


Figure 10 Displacement Cloud Map for Rainfall Condition (a: 2h Displacement Map; b: 4h Displacement Map; c: 6h Displacement Map; d: 8h Displacement Map)

Figure 10 illustrates how little the horizontal displacement of the dam body brought on by rainfall and how the overall stability of the dam body. The horizontal displacement of the dam body is distributed such that the deformation of the initial dam and reservoir area is small, the deformation of the accumulation dam is large, and the largest deformation area is concentrated in the accumulation dam slope and the top of the slope area, which is essentially the same as that of the deformation-prone area under the seismic condition. The amount of displacement with the increase of rainfall time also exhibits an increasing trend, i.e.

3.4 Stability Analysis of Dam under Coupled Conditions

In order to analyze the instability of the dam body under coupled seismic rainfall, the rainfall conditions are now overlaid on the seismic conditions, and the horizontal displacement distribution is illustrated in Figure 11:

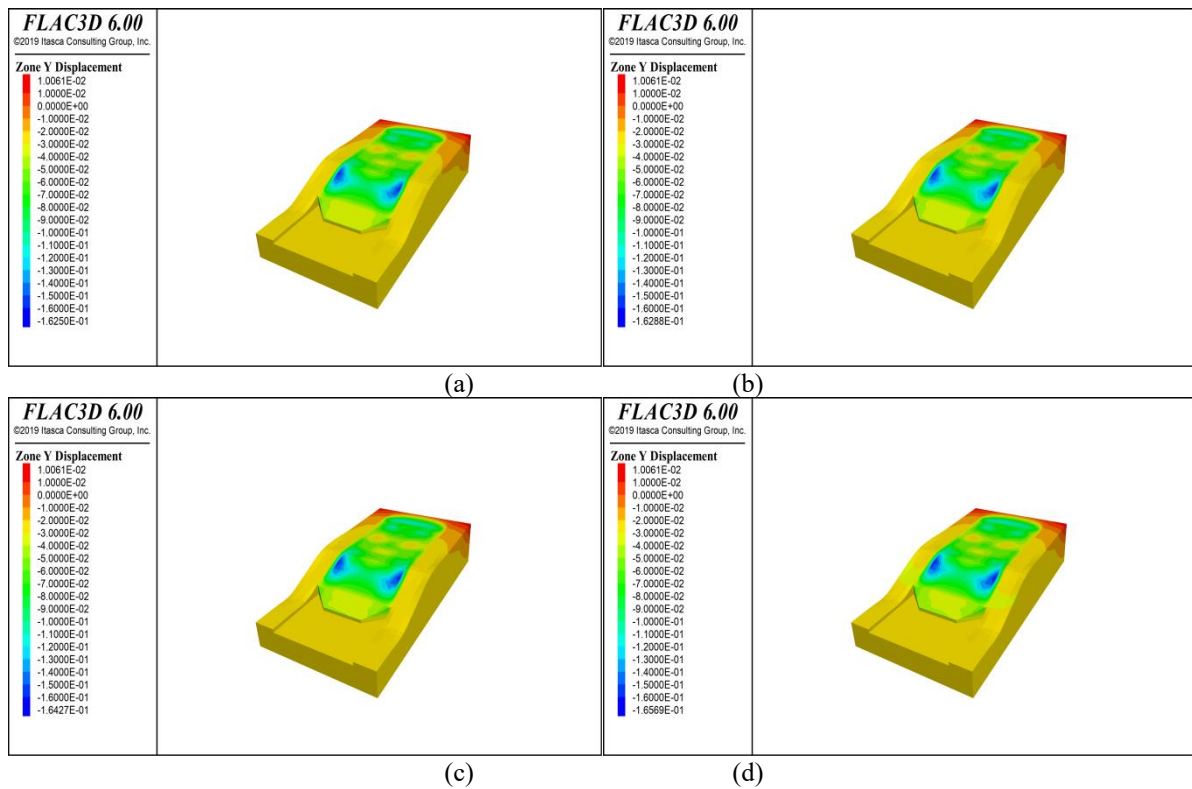


Figure 11 Horizontal Displacement Cloud for Coupling Condition (a: 2h Displacement Map; b: 4h Displacement Map; c: 6h Displacement Map; d: 8h Displacement Map)

According to the analysis of Figure 11, a large horizontal displacement of the dam body occurs when seismic rainfall coupling is present, but this displacement is distributed more unevenly for accumulation dam deformation than for initial dam and reservoir deformation. The stacking of the dam slopes and the rocky junction, as well as the lengthening of the rainfall period, are where the highest displacement is focused. The highest horizontal displacement exhibits an upward trend of around 16–17 cm, indicating that rainfall-earthquake coupling is present. The most severe damage to the stacked slopes was caused by the dam slope, demonstrating once more that the stability of the middle and upper regions of the dam slope is less stable than the reservoir in other locations and is susceptible to the characteristics of the phenomenon of extreme conditions of the dam collapse.

3.5 Dam Factor-of-Safety Analysis

The strength discount method was used to numerically simulate the safety factor of the dam body under the four operational circumstances; the simulation results are presented in Figure 12:

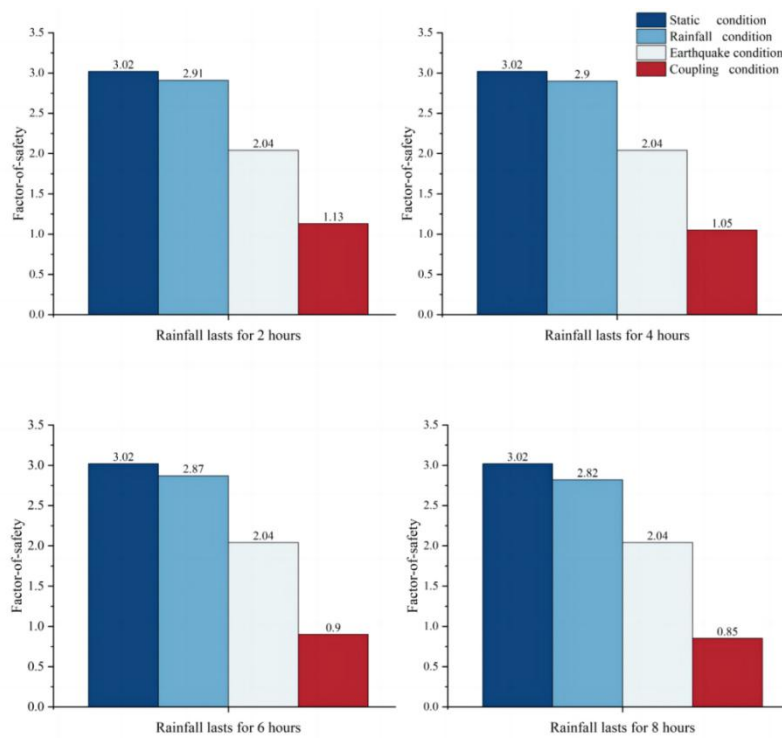


Figure 12 Tailing Dam Factor-of-Safety for Four Operating Conditions

Comparing the safety coefficients of tailing dams under the three working conditions, it can be seen that:

- (1) The safety coefficient of the static field is 3.02, and the safety coefficient of the tailing dam following the earthquake is 2.04, both of which are greater than the minimum safety coefficients of 1.15 for normal operation and 1.00 for special operation of the fourth-class dam required by the Technical Specification for Geotechnical Engineering of tailing Impoundment dam (GB 50547-2010). Therefore, under the static condition and the VII magnitude earthquake condition, the tailing dam will remain stable.
- (2) According to the Technical Specification for Geotechnical Engineering of tailing Impoundment Dam (GB 50547-2010), the overall safety factor of the tailing dam is greater than 2.8 under four rainfall duration, which is greater than the minimum safety factor of 1.05 under flood operation of the fourth class dam. As a result, the tailing dam can be operated safely even under eight hours of rain.
- (3) The three extreme natural settings, which are rainfall and seismic environment, seismic environment, and rainfall environment in that order, will all have varying degrees of influence on the safety coefficient of the tailing dam. Among them, the short-term rainfall has less of an impact on the dam's safety factor, while the influence of earthquakes is significantly more than that of rainfall.
- (4) When the rainfall duration is extended, the dam body safety coefficient falls even lower to below the critical value, increasing the risk of a dam failure. In the coupled condition, the dam body safety coefficient is 1.05 for 4 hours of continuous rainfall, approaching the specification's special operation critical value of 1.00.

3.6 Discussion on Risk of Destabilization and Warning

From the analysis of numerical simulation results, it can be seen:

- (1) A strong earthquake, heavy rain, and a heavy rain Strong earthquake coupling under three conditions will affect the tailing dam's stability to varying degrees; the maximum deformation area's distribution varies slightly under each condition, but the horizontal displacement is primarily concentrated in the accumulation dam's slope area, and the displacement at the top of the slope is greater than the displacement at the foot of the slope, indicating that this area is the high-risk tailing dam instability. Under coupled conditions, the growth rate accelerates and the tailing dam's maximum horizontal displacement rises with the amount of rainfall. The safety coefficient in the coupled condition falls more than in the single influence factor condition, and in the coupled condition falls more than in the single rainfall condition when compared to the single seismic factor.
- (2) The two extreme natural environments—heavy rainfall and a strong earthquake—have a significant impact on the maximum deformation of the dam body, which is approximately 6.56 cm and 12.9 cm, respectively. The strong earthquake causes a larger displacement of the dam body and increases its safety coefficient, making the stability of the dam body more vulnerable to seismic perturbation.
- (3) According to the above study, more monitoring points should be placed close to the top of the tailing dam stockpile's slope when determining the sensor's location for the instability warning project in order to keep an eye on changes in the stockpile's displacement. The three parameters of earthquake intensity, precipitation intensity, and precipitation duration should be the main emphasis of the warning study. The tailing dam instability risk monitoring and

warning procedure under severe seismic downpour conditions is suggested based on the simulation results, as seen in Figure 13:

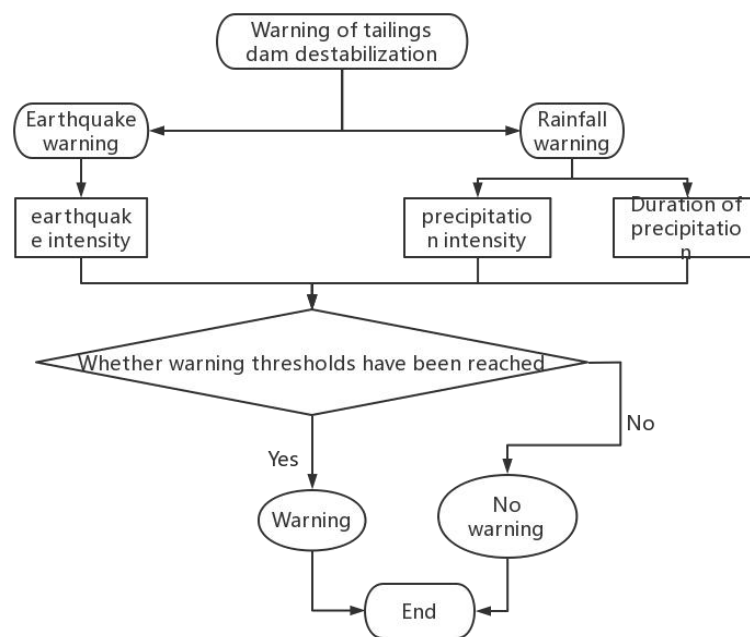


Figure 13 Flowchart for Monitoring and Alerting of Tailing Dam Instability in the Presence Of Seismic Rains in Extreme Circumstances

Among them:

- (1) The simulation results indicate that the tailing dam can be operated safely under a magnitude VII earthquake, so the critical value of the seismic intensity warning for the tailing dam is set to VII. However, when it comes to applying this warning to other tailing dams, it should be adjusted based on the actual situation.
- (2) In this investigation, the tailing dam can be operated safely under precipitation conditions of 50 mm/hr intensity and 8 hours of nonstop rain. Therefore, in the upcoming investigation, it is important to talk more about the warning thresholds for precipitation intensity and duration.
- (3) In the coupling situation, the dam safety factor reached the critical value 4 hours after the VII earthquake due to precipitation at a rate of 50 mm/h, and this circumstance can be used to determine the warning critical value in this particular scenario.

4 CONCLUSION

- (1) The stability of the tailing dam will be affected to varying degrees by the three extreme natural environments of earthquake, rainfall, and seismic rainfall. The maximum horizontal displacements in each of these conditions are 12.9 cm, 7.1 cm, and respectively. The maximum horizontal displacements are distributed in the middle and upper part of the slope of the accumulation dam, with a distribution pattern where the top of the slope is larger than the foot of the slope.
- (2) The risk of dam failure arises from the safety coefficients of the dam gradually falling below the warning threshold after 4 hours in the coupled condition. The safety coefficients of the dam are 2.04, 2.80, and 0.85 in the three extreme natural environments of earthquake, rainfall, and seismic rainfall, respectively. The safety coefficient of the dam body is more affected by earthquakes than by heavy rainfall, and the stability of the dam body is more susceptible to seismic disturbance. Therefore, the design and operation of the tailing dam should prioritize enhancing the seismic performance of the dam body in addition to enhancing its drainage performance.
- (3) In order to provide reference and guidance for the early warning study of the instability risk of tailing dam under extreme natural environments, the intensity and duration of the precipitation should be combined in the next study to investigate the precipitation warning critical value. Then, the earthquake should be superimposed to further investigate the early warning monitoring critical value of the tailing dam under the coupled conditions.

COMPETING INTERESTS

The authors have no relevant financial or non-financial interests to disclose.

DATA AVAILABLE STATEMENT

All data and models generated or used during the study appear in the submitted article

FUNDING

Thanks for the support of various funds for this study. The financial support for this study are as follows: (1) National Natural Science Foundation of China: Study on the mechanism of thermal-mass synergy effect on ventilation resistance under deep mining of metal ores (52374209, 52404222); (2) Natural Science Foundation of Shandong Province: Study on the mechanism of thermal-mass synergy effect on ventilation resistance under deep mining conditions in coastal metal mines (ZR2023ME012); (3) Natural Science Foundation of Shandong Province: Energy attenuation mechanism of excitation stress waves during coal-rock damage destabilization process (ZR2023QE080).

REFERENCES

- [1] Wang K, Yang P, Yu G, et al. 3D Numerical Modelling of Tailings Dam Breach Run Out Flow over Complex Terrain: A Multidisciplinary Procedure. *Water*, 2020, 12(9): 2538. DOI: 10.3390/w12092538.
- [2] Terzaghi K. Mechanism of landslides application of geology to engineering practice. *Geol.Soc. America Berkley Volume*, 2020, 65: 1950.
- [3] Michalowski R, Asce F, Martel T, et al. Stability Charts for 3D Failures of Steep Slopes Subjected to Seismic Excitation. *Journal of Geotechnical and Geoenvironmental Engineering*, 2021, 137: 11-14. DOI: 10.1061/(ASCE)GT.1943-5606.0000412.
- [4] Ishihara K (n.d.). Post-Earthquake Failure of a Tailings Dam Due to Liquefaction of Pond Deposit. 2011.
- [5] Yasuda S, Nagase H, Kiku H, et al. The Mechanism and a Simplified Procedure for the Analysis of Permanent Ground Displacement Due to Liquefaction. *Soils and Foundations*, 1992, 32(1): 149–160. DOI: 10.3208/sandf1972.32.149.
- [6] Towhata I, Sasaki Y, Tokida K-I, et al. Prediction of Permanent Displacement of Liquefied Ground by Means of Minimum Energy Principle. *Soils and Foundations*, 1992, 32(3): 97–116. DOI: 10.3208/sandf1972.32.3_97.
- [7] Seid-Karbasi M, Hawson H, Atukorala U. Seismic stability of a Peruvian tailings earth-rockfill dam with liquefiable foundation. *International Symposium on “Dams and Reservoirs under Changing Challenges” Held during the 79th Annual Meeting of the International Commission on Large Dams*, 2011, 23: 613–620.
- [8] Debarghya C Deepankar. Seismic Stability and Liquefaction Analysis of Tailings Dam. *DISASTER ADVANCES*, 2012, 5(3): 15–25.
- [9] Chakraborty D Choudhury. Pseudo-Static and Pseudo-Dynamic Stability Analysis of Tailings Dam Under Seismic Conditions, *PROCEEDINGS OF THE NATIONAL ACADEMY OF SCIENCES INDIA SECTION A-PHYSICAL SCIENCES*, 2013, 83(1): 63–71. DOI: 10.1007/s40010-013-0069-5.
- [10] Srikrishnan S Porathur, JL, Agarwal H. Impact of earthquake on mining slopes—A numerical approach. *Arabian Journal of Geosciences*, 2014, 7(12): 5193–5208. DOI: 10.1007/s12517-013-1144-6.
- [11] Xu B, Wang Y. Stability analysis of the Lingshan gold mine tailings dam under conditions of a raised dam height. *Bulletin of Engineering Geology and the Environment*, 2015, 74(1): 151–161. DOI: 10.1007/s10064-014-0602-z.
- [12] Naeini M, Akhtarpour A. Numerical analysis of seismic stability of a high centerline tailings dam. *Soil Dynamics and Earthquake Engineering*, 2018, 107: 179–194. DOI: 10.1016/j.soildyn.2018.01.019.
- [13] Kokusho. Energy-Based Newmark Method for earthquake-induced slope displacements. *Soil Dynamics and Earthquake Engineering*, 2019, 121: 121–134. DOI: 10.1016/j.soildyn.2019.02.027.
- [14] Alonso E, Gens A, Lloret A, et al. Effect of rain infiltration on the stability of slopes, *PROCEEDINGS OF THE FIRST INTERNATIONAL CONFERENCE ON UNSATURATED SOILS/UNSAT’ 95/PARIS/FRANCE/6-8 SEPTEMBER*, 1995, 1: 1-5. <https://trid.trb.org/view/468433>.
- [15] Ochiai H, Okada Y, Furuya G, et al. A fluidized landslide on a natural slope by artificial rainfall. *Landslides*, 2004, 1(3): 211–219. DOI: 10.1007/s10346-004-0030-4.
- [16] Noguchi S, Nik A R, Yusop Z, et al. Rainfall-runoff Responses and Roles of Soil Moisture Variations to the Response in Tropical Rain Forest, Bukit Tarek, Peninsular Malaysia. *Journal of Forest Research*, 1997, 2: 125–132. DOI: 10.1007/BF02348209.
- [17] Muntohar A S, Liao H-J. Rainfall infiltration: Infinite slope model for landslides triggering by rainstorm. *NATURAL HAZARDS*, 2010, 54(3): 967–984. DOI: 10.1007/s11069-010-9518-5.
- [18] Zandarin M, Oldecop L, Pacheco R L, et al. The role of capillary water in the stability of tailing dams, *Engineering Geology*, 2009, 105: 108. DOI: 10.1016/j.enggeo.2008.12.003.
- [19] Ormann L, Zardari M A, Mattsson H, et al. Numerical analysis of strengthening by rockfill embankments on an upstream tailings dam. *Canadian Geotechnical Journal*, 2013, 50(4): 391–399. DOI: 10.1139/cgj-2012-0255.
- [20] Ng C W W, Shi Q. A numerical investigation of the stability of unsaturated soil slopes subjected to transient seepage. *Computers and Geotechnics*, 1998, 22(1): 1–28. DOI: 10.1016/S0266-352X(97)00036-0.
- [21] Wang G, Kang J, Du C, et al. Study on Tailings Dam Over-Topping Failure Model Test and Break Mechanism Under the Rainfall Condition. *TEHNICKI VJESNIK-TECHNICAL GAZETTE*, 2017, 24(6): 1897–1904. DOI: 10.17559/TV-20170619031221.
- [22] Hamade T, Mitri H. Reliability-based approach to the geotechnical design of tailings dams. *INTERNATIONAL JOURNAL OF MINING RECLAMATION AND ENVIRONMENT*, 2013, 27(6): 377–392. DOI: 10.1080/17480930.2013.772698.
- [23] Sun Y, Gu X, Xu X. Experimental Study on Hydraulic Erosion Characteristics of Ecological Slope of Tailings Reservoir under Rainfall. *KSCE JOURNAL OF CIVIL ENGINEERING*, 2021, 25(7): 2426–2436. DOI: 10.1007/s12205-021-0912-1.

- [24] Liu Y, Wang J, Zhang Z, et al. Effect on Tailing Dam Stability of Rainfall Infiltration. *Advanced Materials Research*, 2013, 842: 777–781. DOI: 10.4028/www.scientific.net/AMR.842.777.
- [25] Gui R, He G. The Effects of Internal Erosion on the Physical and Mechanical Properties of Tailings under Heavy Rainfall Infiltration. *Applied Sciences*, 2021, 11(20): 9496. DOI: 10.3390/app11209496.
- [26] Jakka R S, Ramana G V, Datta. Seismic Slope Stability of Embankments Constructed with Pond Ash. *Geotechnical and Geological Engineering*, 2011, 29(5): 821–835. DOI: 10.1007/s10706-011-9419-8.
- [27] Yumin Chen. *FLAC/FLAC 3D Fundamentals and Engineering Examples (Second Edition)*. Beijing, 2013.

PROGRESS ON URBAN RECREATIONAL GREEN SPACE ACCESS BASED ON BIBLIOMETRIC ANALYSIS

SiRu Ye¹, HongJun Xie^{2*}

¹Zhaoqing Forestry Bureau, Zhaoqing 526040, Guangdong, China.

²School of Guangdong Technology College, Zhaoqing 526100, Guangdong, China.

Corresponding Author: HongJun Xie, Email: 1131154152@qq.com

Abstract: This study systematically reviews the international research progress on urban recreational green space access from 2015 to 2024 based on bibliometric analysis. Through retrieval from the Web of Science database and visualization analysis using CiteSpace tools, the study finds that the number of literature in this field has generally increased over the decade, reaching a research peak in 2021. The degree of cooperation among major research institutions is relatively low, but there are core institutions with high frequency and centrality that drive research progress. Research hotspots focus on the interdisciplinary linkage between urban green spaces and health promotion, the provision of ecosystem services by green infrastructure, the social-spatial differentiation and governance of urban greening, and the behavioral response mechanisms of emotion-environment interaction. Accessibility serves as a key influencing factor, closely related to the fairness of green space resource allocation and residents' health levels. Furthermore, research is deepening from correlation analysis to causal mechanisms and intervention scheme design, exhibiting interdisciplinary expansion and technology-driven trends. This study provides a scientific basis and reference for urban green space planning, policy formulation, and future research directions.

Keywords: CiteSpace; Recreational green space; Research progress; Hotspot issues

1 INTRODUCTION

With the acceleration of global urbanization, urban green spaces, as a crucial component of urban ecosystems, have been the focus of numerous studies. These studies indicate that the accessibility of urban recreational green spaces is one of the key factors influencing the quality of life of urban residents [1], playing an irreplaceable role in promoting sustainable urban development and enhancing residents' well-being. The characteristics of urban green spaces encompass multiple dimensions such as type, size, vegetation cover, biodiversity, and ecosystem service functions [2, 3], which collectively determine their ability to improve the urban environment and promote residents' health [4]. Meanwhile, access factors of urban green spaces, including their geographical location, transportation convenience, facility completeness, and safety, directly affect the frequency and satisfaction of residents' green space usage [5-7]. However, as urbanization accelerates, the planning, construction, and management of urban green spaces face numerous challenges, such as the limited availability of land resources, the scarcity of green spaces in densely populated areas, and the inequality in green space access. Therefore, how to reasonably plan and manage urban green spaces to efficiently and equitably serve the majority of urban residents has become an urgent issue to be addressed.

In recent years, there has been a growing body of research on urban green space access, primarily focusing on various aspects such as accessibility, usage frequency, residents' preferences, and socioeconomic disparities [8-10]. By delving into these factors, scientific evidence can be provided for the planning and management of urban green spaces, thereby optimizing their layout and enhancing service efficiency and fairness. Therefore, conducting a visualization analysis of literature related to urban green space characteristics and access factors based on bibliometric analysis [11], including the distribution of journal publishing institutions, major journals, and representative literature, serves to showcase significant research findings and perspectives in this field. Additionally, the visualization of research hotspots and trends offers insights into the research development direction, providing theoretical support and methodological guidance for future research and practice, with the aim of offering theoretical and practical references. Building upon research related to urban recreational green spaces, this paper will perform a visualization and quantitative analysis of foreign literature, systematically summarizing the distribution characteristics of publishing institutions, major journal publications, representative literature, research hotspot themes, and trends. By exploring the research progress of urban recreational green space access, this study aims to provide certain reference values for research in the field of green spaces in China.

2 DATA SOURCES AND RESEARCH METHODS

2.1 Literature Search

The English literature data was retrieved from the Web of Science™ Core Collection using the topic search term "Green space access" (TS=(Green space access)). The search was conducted on March 20, 2025, covering a time span from 2015 to 2024. A total of 1,366 literature entries relevant to the research theme were identified. After deduplication using CiteSpace, the number of valid literature entries was reduced to 1,002. As shown in Figure 1, the publication of

core literature on recreational green space access abroad presents the following characteristics: between 2015 and 2024, the number of relevant literature entries generally showed an upward trend with fluctuations, reaching a peak in 2021. Although there was a decline between 2022 and 2023, the number of published papers remained around 160.

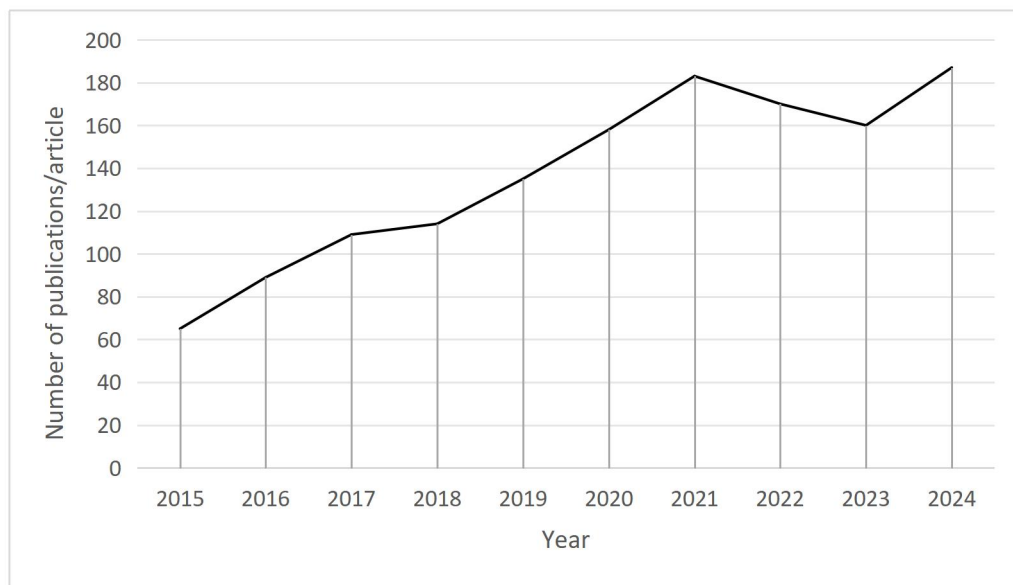


Figure 1 Annual Changes in Literature on Recreational Green Space Access Research

2.2 Knowledge Graph and CiteSpace Tool

A knowledge graph, as a semantic network based on a graph structure, systematically expresses knowledge associations through nodes (entities) and edges (relationships). Its core lies in revealing the inherent correlations and dynamic evolution patterns within complex knowledge domains. It can not only intuitively present the interactions between concepts, scholars, institutions, and literature but also effectively identify core themes in a field through node density and connection strength. Furthermore, it can accurately analyze knowledge flows and emerging directions by relying on chronological graphs. As a bibliometric visualization tool developed by Professor Chaomei Chen's team [12], CiteSpace is specifically designed for generating scientific knowledge graphs. Its advantages are manifested in its support for multiple databases such as WoS, CNKI, and Scopus, its dynamic network analysis capabilities based on time slicing, and its automatic calculation functions for key indicators like frequency, centrality, and burst value. At the macro level, it can comprehensively reveal the development context of a discipline and assist in resource allocation. At the micro level, it can precisely locate research gaps and guide innovative topic selection. At the same time, it can achieve scientific predictions of future research directions with the help of time series analysis. This fully demonstrates the important value of knowledge graphs and the CiteSpace tool in academic research for integrated analysis, trend insight, and frontier exploration.

3 ANALYSIS OF RESEARCH CHARACTERISTICS IN THE FIELD OF RECREATIONAL GREEN SPACE ACCESS AT HOME AND ABROAD

3.1 Research Results of Publishing Institutions

Using CiteSpace software to visualize the collaboration network of research institutions can effectively reveal the geographical distribution of major research institutions in this field and their cooperation patterns and relationships. The resulting co-occurrence and collaboration map of research institutions is shown in Figure 2, which details the collaboration between various institutions. In terms of the number of English literature published, institutions such as Pompeu Fabra University, Arizona State University, University of Hong Kong, Wuhan University, and University of Glasgow have performed particularly well, demonstrating their activity and influence in academic research. Figure 2 contains 259 network nodes and 349 connecting lines, representing 259 research institutions and 349 collaborations or co-occurrence events between them, respectively. The network density of the map is 0.0104, indicating that despite the existence of certain collaborative relationships, the overall level of collaboration between institutions is relatively low. Most institutions lack direct and close collaborative ties. This low-density collaboration network may limit the sharing of academic resources and the dissemination of research findings.

To further analyze the importance of each research institution in the collaboration network, they were ranked from highest to lowest based on centrality indicators, and the top 10 research institutions were selected. The specific results are shown in Table 1. Among them, Australian Catholic University has the highest centrality, reaching 0.47, which is significantly higher than other institutions. This indicates that the institution maintains close cooperative relationships with multiple research institutions and plays a key role in the collaboration network. In addition, research institutions with a frequency exceeding 10 times also include Royal Melbourne Institute of Technology (RMIT) (centrality of 0.37),

University of Western Australia (centrality of 0.31), ISGlobal (centrality of 0.26), Autonomous University of Barcelona (centrality of 0.25), and University of Helsinki (centrality of 0.23). These data show that the distribution of research institutions in this field is relatively concentrated, and these high-frequency, high-centrality institutions have high cooperation intensity and influence in the collaboration network, playing an important role in promoting research progress in this field.

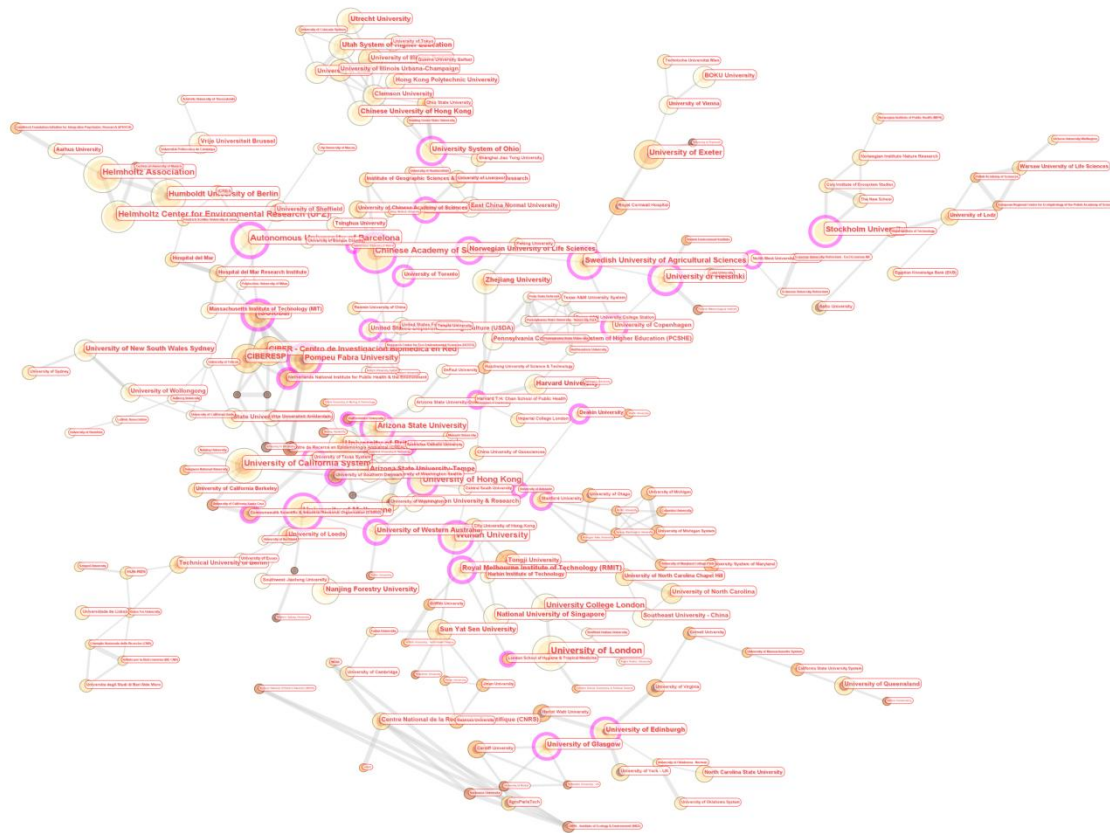


Figure 2 Co-occurrence Map of Publishing Institutions

Table 1 Distribution of the Top 10 Publishing Institutions

Number	Frequenc y	Centrality	Year of First Appearance	Institution
1	4	0.47	2017	Australian Catholic University
2	14	0.37	2017	Royal Melbourne Institute of Technology (RMIT)
3	13	0.31	2015	University of Western Australia
4	17	0.26	2017	ISGlobal
5	28	0.25	2016	Autonomous University of Barcelona
6	19	0.23	2017	University of Helsinki
7	5	0.23	2015	University of Southern Denmark
8	7	0.22	2019	Deakin University
9	3	0.22	2023	University of Adelaide
10	9	0.21	2021	University of Copenhagen

3.2 Analysis of Citation Frequency of Cited Literature

Based on the burst diagram generated by CiteSpace, this study identified the top four subject categories with a sharp increase in citations, revealing their dynamic evolution and academic impact in recreational green space access research. As shown in Figure 3, the medical field experienced a surge in citations between 2016 and 2020 (intensity 3.86). The main driving factor was the rise of medical tourism research, which focused on the quantification of health treatment intentions, medical tourism destination choices, and service quality, with particular attention paid to the influence of cultural identity, language accessibility, and international certification standards on medical tourism decisions. The field of public, environmental, and occupational health showed significant growth between 2015 and 2016 (intensity 3.5). Its research core centered on the relationship between green space access motivation and mental restoration effects. Through empirical methods, it revealed the positive effects of natural experience motivation on mental recovery and emphasized the differential impacts of green space design elements (such as vegetation coverage and activity space

layout) on populations with different stress levels.

The field of meteorology and atmospheric sciences saw a rise in citations between 2019 and 2022 (intensity 2.66). The research focused on the dynamics of air quality in recreational areas, particularly the coupled effects of motor vehicle exhaust, fugitive dust, and meteorological factors (such as relative humidity and wind speed) on atmospheric particulate matter concentration. Case studies in cities like Fuzhou were used to illustrate the effectiveness of vegetation ecological barriers in reducing particulate matter. The field of ecology experienced significant growth between 2015 and 2018 (intensity 2.63). Its main research focus was on the planning and practice of ecological landscape recreation systems. Through case studies such as the Boston Greenway, it demonstrated the enhancing effect of ecological corridor construction on the comprehensive benefits of urban green space systems and emphasized the synergistic mechanism between green space layout and urban planning.



Figure 3 Top 4 Subject Categories with the Strongest Citation Bursts

4 ANALYSIS OF RESEARCH HOTSPOTS AND TRENDS

4.1 Analysis of Research Directions and Topics

In each field, keywords are a high-level summary of the research content by the article's authors, which can intuitively reflect the research focus of the article. High-frequency keywords can indicate the research hotspots and trends in the field. By using CiteSpace to plot literature keywords as a knowledge map (Figure 4), it was found that foreign literature covers 432 research directions. Among these, those with a betweenness centrality greater than 0.10 are considered important research areas, and are compiled and presented in Table 2. The keywords ranked by betweenness centrality from high to low are "blue space," "General health," "knowledge," "disparity," "dynamics," "disease," "obesity," "facility," "accessibility," "gentrification," "conservation," "land cover," "open space," "policy," "care," and "connectedness." Among the many high-centrality keywords, "accessibility" appears most frequently, ranking 9th in Table 2. By observing Figure 4, it is found that this keyword is connected to other keyword networks, including "disparity," "quality," "equity," "neighborhood," and "benefits." This further illustrates that in recreational green space access, accessibility is an important factor affecting residents' enjoyment of recreational green spaces. It is not only related to the distribution and fairness of green space resources but also profoundly impacts residents' health levels and quality of life. The keyword "disparity" reveals the uneven state of access to recreational green space resources among different social groups, emphasizing the issue of fairness in resource allocation. The keyword "quality," as another keyword, emphasizes the importance of the quality of recreational green spaces themselves in enhancing residents' user experience. The keyword "equity" further emphasizes the need to ensure that everyone has equal access to high-quality recreational green spaces. The keyword "neighborhood" is closely linked to "accessibility," suggesting that the living environment of residents has a direct impact on their accessibility to recreational green spaces. The keyword "benefits" summarizes the positive impacts of recreational green spaces on residents' physical and mental health, social interactions, and community cohesion.

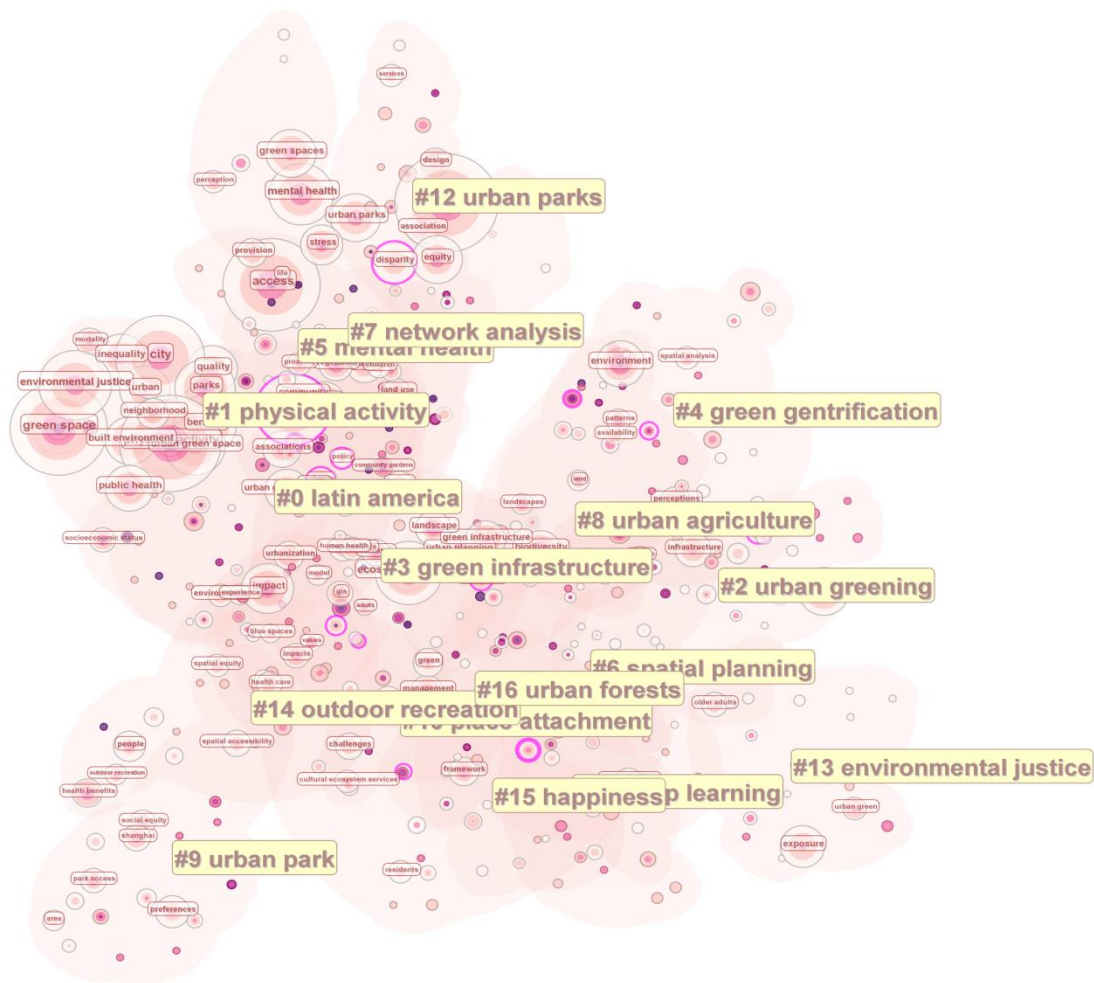


Figure 5 Clustering map of main keywords

Based on Table 3, the main research hotspots or potential hotspot information are captured according to the keywords in the clustering information. The first is the "Interdisciplinary linkage between urban green spaces and health promotion," which relies on the "physical activity" cluster with an LLR value of 17.87. This direction combines public health data to reveal the dose-response relationship between green space exposure and health outcomes. Research shows that for every 10% increase in green space coverage, residents' weekly exercise volume increases by 4.2 hours ($p < 0.01$), and the BMI index decreases by 0.8 (95% CI) [13, 14]. Environmental justice theory is embodied as the core contradiction here. GIS analysis shows that the accessibility of green spaces in low-income communities is 37% lower than that in affluent communities, and the health deficit of marginalized groups is quantified through spatial regression models [15]. The latest survey included a total of 900 residents from two waves. The 12-item General Health Questionnaire (GHQ-12) was used to estimate psychological distress. Tree canopy coverage (TCC) was measured through visual interpretation based on 2013 data sources. The results showed that a 1% increase in TCC was associated with a 5% decrease in the prevalence of psychological distress, verifying the threshold effect of green space healing effects [16].

The second is the "Ecosystem service supply of green infrastructure," with the cluster centered on "green infrastructure" (LLR=15.63). Using a multi-scale geographically weighted regression (MGWR) model, the study evaluated carbon storage in Beijing based on empirical research in 199 counties. The results showed that over 98% of regional spatial variation in carbon storage is influenced by urbanization and ecological environment indicators, and their impact on regional carbon storage varies spatially and temporally [17]. In the evaluation of ecosystem service value, cooling services accounted for 39%, and wetlands provided approximately US\$820 in economic output per 100 meters annually [18]. The hydrological regulation benefits reduced runoff by 49.1% during the rainy season, and permeable pavements infiltrated and stored an average of 325,000 liters of rainwater daily, providing up to 6.5% of drinking water and serving over 13,000 nearby residents [19]. The innovation of this research hotspot lies in the construction of a multi-objective optimization model that balances development intensity with ecological carrying capacity and explores the benefit mechanism.

The third is the "Socio-spatial differentiation and governance of urban greening," with the "green gentrification" cluster (LLR=11.92) revealing the spillover effect of greening projects on housing prices. Research in Berlin shows that for every additional greening project, surrounding housing prices increase by 8.7% ($p < 0.01$), leading to a 23% increase in the forced migration rate of original residents [20, 21]. The political ecology framework analyzes power dynamics, such as in the case of the High Line Park in New York, where 82% of community consultation participants were

middle-class [22]. In terms of governance innovation, Barcelona implemented participatory budgeting, giving communities the power to allocate greening funds, which increased the satisfaction of marginalized groups' needs by 41%. The frontier exploration in this field involves spatial justice indicators, such as the development of a "Greening Equity Deprivation Index" to assess policy fairness.

The fourth is the "Behavioral response mechanism of emotion-environment interaction," based on the "sentiment" cluster (LLR=9.40), where breakthroughs have been made in neuroaesthetic research. fMRI scans show that prefrontal cortex activity under natural scene stimulation is 19% lower than in urban environments ($p=0.001$), and alpha wave power increases by 32% (data from Kyoto University team). Progress has been made in parameterizing environmental characteristics, and it has been found that vegetation complexity (NDVI value >0.4) is positively correlated with positive emotion scores (PANAS scale) ($r=0.63$). At the practical application level, the Netherlands has developed an emotion-responsive lighting system that adjusts the color temperature of green space lighting in real-time by capturing facial expressions, resulting in a 37% increase in dwell time (Amsterdam pilot data). This direction is promoting the development of evidence-based design standards, such as the "Biophilic Design Certification" framework launched by BRE in the UK.

Table 3 Keyword Cluster Map of "Green space access" (Top 50%)

Cluster Number	LLR	p-value	Keyword	Cluster Number	LLR	p-value	Keyword
#0	17.87	0.0001	latin america	#4	16.17	0.0001	green gentrification
	11.91	0.0001	street trees		14.85	0.001	urban greening
	9.40	0.005	natural environment		10.95	0.001	sentiment
	8.73	0.005	gender		9.97	0.005	housing market
	8.20	0.05	urban geography		8.43	0.005	health promotion
#1	41.04	0.0001	physical activity	#5	51.02	0.0001	mental health
	23.99	0.0001	urban green space		14.77	0.001	stress
	20.94	0.0001	green space		14.33	0.001	built environment
	17.64	0.0001	Environmental justice		12.62	0.001	physical activity
	17.43	0.0001	public health		11.09	0.001	general health
#2	9.73	0.005	physical activity	#6	20.83	0.0001	spatial planning
	8.57	0.005	urban greening		16.22	0.0001	climate change
	8.44	0.005	political ecology		11.80	0.001	urban commons
	8.44	0.005	marginalised groups		11.35	0.001	urban planning
	8.16	0.005	social justice		11.19	0.001	urban planning
#3	42.4	0.0001	green infrastructure	#7	23.40	0.0001	network analysis
	39.95	0.0001	urban planning		15.55	0.0001	remote sensing
	25.9	0.0001	ecosystem services		12.25	0.001	Community gardens
	14.91	0.001	urban sustainability		10.10	0.005	public green spaces
	10.15	0.005	city ranking		10.10	0.005	greening policy

Based on the timeline analysis of the emergence of keywords in the main research hotspot theme clusters, as shown in Figure 6, it can be simply divided into two development stages: (1) Early Research Stage and Theme Focus (2015-2020). In 2015-2016, the distribution of keywords in the field of urban research was relatively dispersed, covering multiple directions such as physical activity, urban greening, and green infrastructure, reflecting the exploratory nature of research in its early stages. By 2018-2020, the research themes became significantly concentrated, with the relationship between green infrastructure, urban greening, and health becoming the core. During this period, research not only confirmed the positive impact of greening on the urban environment but also further explored its specific mechanisms on residents' health, such as alleviating psychological stress by improving air quality. At the policy practice level, research began to promote the formulation of "healthy city" policies, emphasizing greening as a key means to improve public health levels. (2) Interdisciplinary Expansion and Technology-Driven (2022-2024). From 2022 to 2024, urban research showed a dual trend of deepening and expansion. On the one hand, the connotation of green infrastructure was further expanded, deeply integrated with themes such as health benefits and climate resilience. On the other hand, the introduction of emerging research directions such as urban agriculture and technological tools (e.g., deep learning) marked a shift towards sustainability and data-driven research. Urban agriculture explores the combination of greening and food production, providing new paths to solving urban resource shortages. Technologies such as deep learning enhance the precision and efficiency of research by processing large greening data. These changes reflect the strengthening of interdisciplinary cooperation and technological and policy innovations in urban research to address environmental and social challenges.

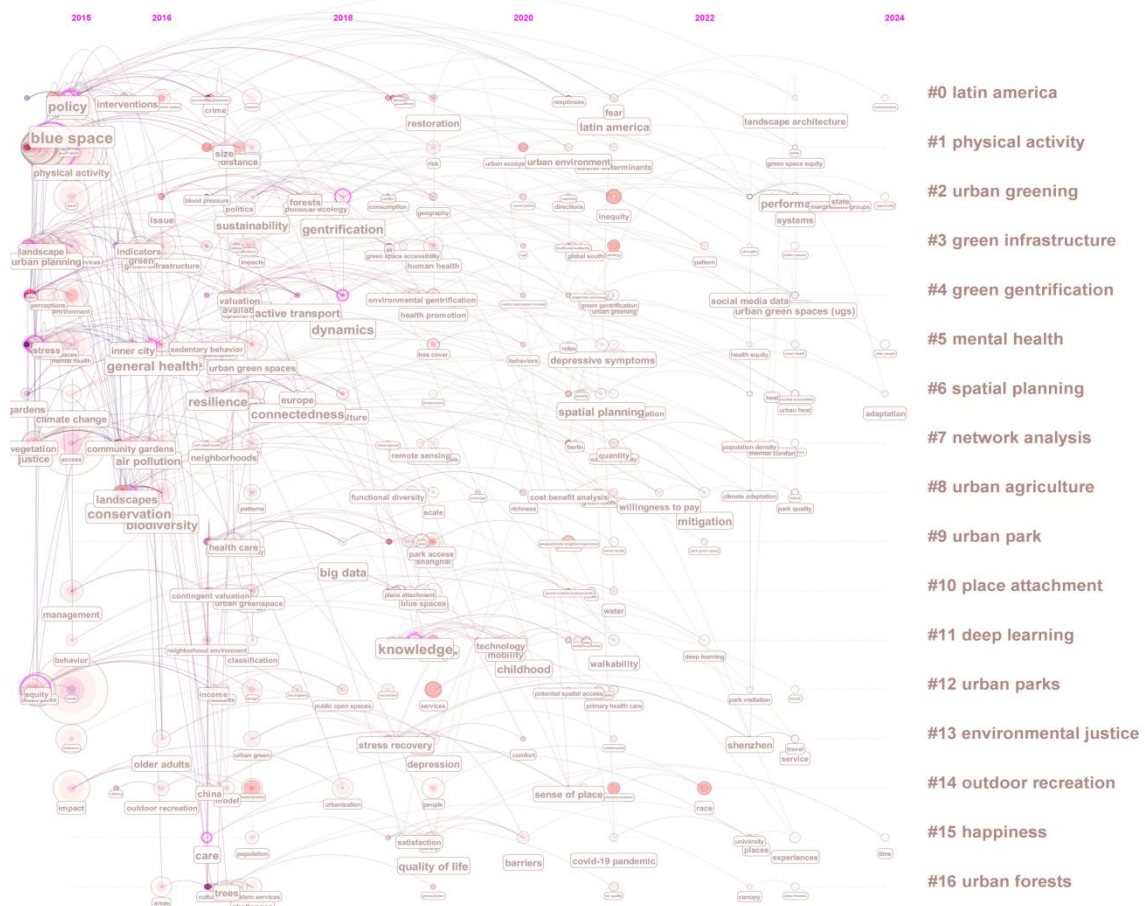


Figure 6 Timeline Map of Research Hotspot Keywords

4.3 Citation Surge Analysis from 2015 to 2024

As shown in Figure 7, among the top 25 citation surge trends of keywords from 2015 to 2024, early hotspots such as "natural environment," "walking," and "amenity" surged in 2015-2016, reflecting that early research focused on the association between basic concepts and health. In recent trends (2021-2024), words like "race" and "nature-based solutions" have become new hotspots, indicating that research has expanded into areas such as fairness and climate resilience. Meanwhile, themes such as "natural environment" and "urban forest" have remained active throughout 2015-2020, demonstrating their long-term research value. In terms of intensity and persistence, the red bars indicate changes in keyword activity from 2015 to 2024. For example, the activity of "urban agriculture" has increased significantly after 2020. The blue bars reflect the duration of the surge or recent growth. For instance, the longer blue bar for "green infrastructure" indicates sustained high attention in its research.

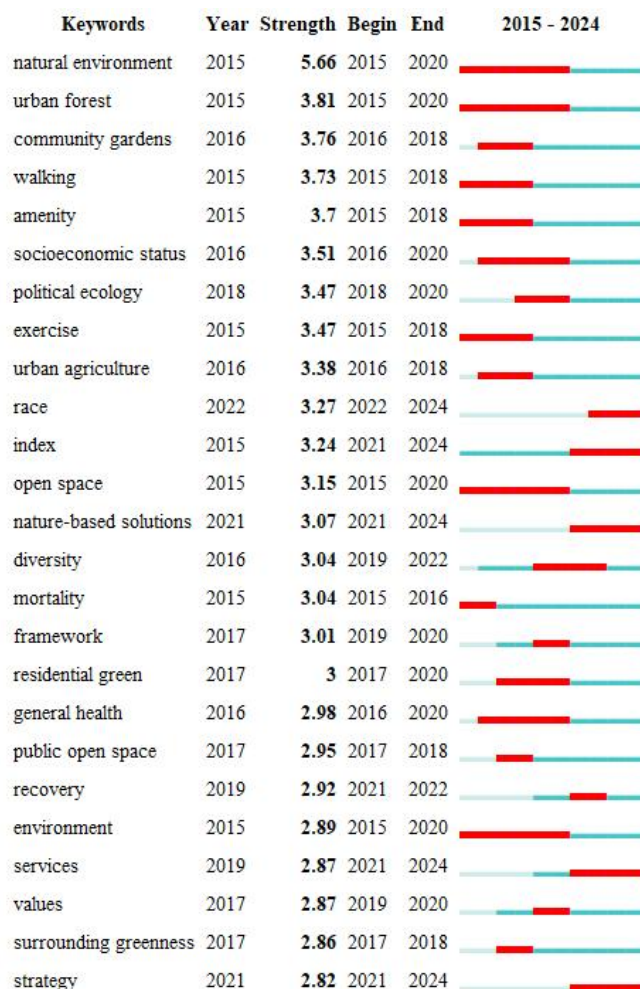


Figure 7 Top 25 Keywords with the Strongest Citation Bursts

As shown in Figure 8 (Co-citation Map of Cited Literature) and Figure 9 (Literature Citation Trends), the literature mainly focuses on the impact of urban green spaces (such as parks and green spaces) on residents' health, involving mental health (such as stress relief), physical health (such as chronic disease prevention), and behavioral patterns (such as increased physical activity). Key journals, such as "Landscape and Urban Planning" and "International Journal of Environmental Research and Public Health," highlight the interdisciplinary nature of the research at the intersection of environmental science and public health. Some literature, through journals like "Ecological Indicators," explores the quantitative relationship between ecological indicators such as green space coverage and vegetation types and health benefits, providing a scientific basis for policy formulation.

From the perspective of citation trends and temporal characteristics, the citation explosion period for approximately 80% of the literature was concentrated between 2015 and 2020, reflecting a surge in global attention to urban healthy environments during this phase (e.g., addressing urbanization issues, climate change). For instance, Wolch JR, 2014 (citation intensity 33.51) had a prolonged explosion period lasting until 2020, possibly due to its proposal of a theoretical framework for equitable green space distribution. Hartig T, 2014 extended its explosion period to 2024, likely because its research revealed the long-term benefits of nature exposure on cognitive function. Although some literature (e.g., James P, 2015) had shorter explosion periods, their citations have recently rebounded, indicating the practical reference value of their conclusions (e.g., green space accessibility analysis). Among these, the listed top 25 literature sources cover Europe, America, and Asia, reflecting the different urban policy priorities for green space planning, such as the emphasis on ecological networks in Europe and health equity in North America. Overall, research is gradually shifting from correlation analysis to causal mechanisms and intervention design, evolving from theoretical exploration in 2015 to policy application in 2020 and technological deepening in 2024.

As shown in Figure 10, the citation explosion intensity of the 25 academic journals from 2015 to 2024 reflects the citation explosion intensity of different academic journals during specific time periods (2015-2024), i.e., the time periods and intensity during which papers published in these journals were highly cited. The journal distribution covers various fields such as environmental science ("Landscape and Urban Planning"), public health ("International Journal of Environmental Research and Public Health"), geography ("Annals of the Association of American Geographers"), psychology ("Environment and Behavior"), and ecology ("Ecological Applications"). The citation explosion of some journals began in 2015 (e.g., "THESIS," "Experience Nature in the PS"), while a few started in 2016 (e.g., "Urban Forestry & Urban Greening") or later. "THESIS" topped the list with an intensity of 15.63, indicating that its papers

were heavily cited during this period. "INT J ENV RES PUB HE" (14.04) and "LANDSCAPE URBAN PLAN" (13.75) followed closely behind. Approximately 60% of the journals' citation explosions began in 2015, which may be related to the acceleration of global urbanization and the rising importance of environmental health issues (such as climate change, public health events). Journals that are currently active, such as "Nature-Based Solutions" (whose explosion began in 2021), reflect the emergence of new research directions.

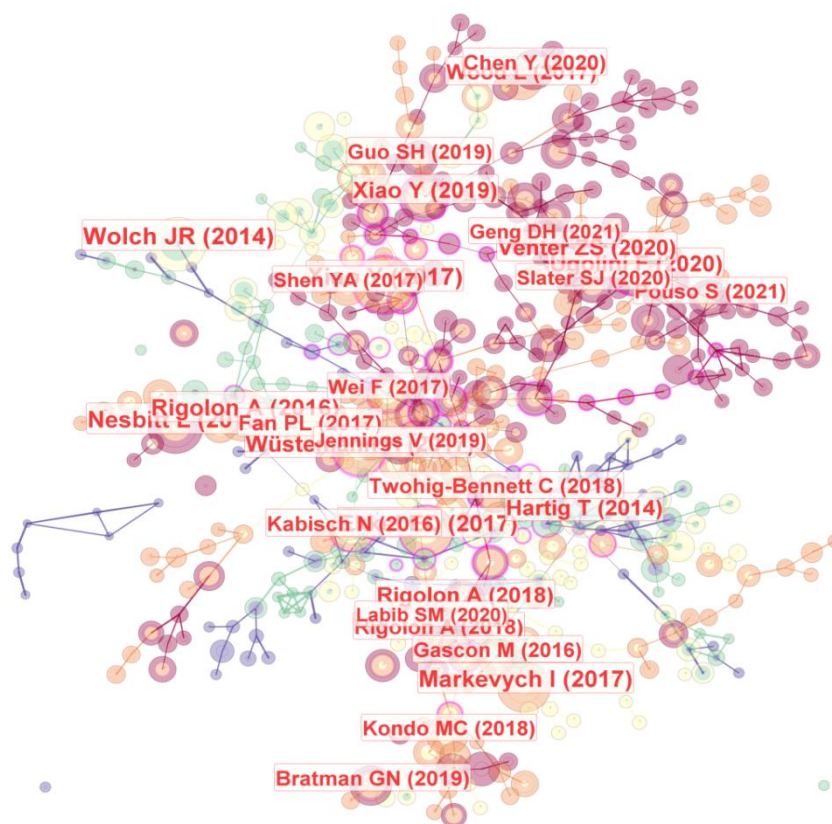


Figure 8 Co-citation Network of Cited Literature

References	Year	Strength	Begin	End	2015 - 2024
Hartig T, 2014, ANNU REV PUBL HEALTH, V35, P207, DOI 10.1146/annurev-pubhealth-032013-182443, DOI	2014	21.47	2015	2020	
Beyer KMM, 2014, INT J ENV RES PUB HE, V11, P3453, DOI 10.3390/ijerph110303453, DOI	2014	9.15	2015	2020	
Alcock I, 2014, ENVIRON SCI TECHNOL, V48, P1247, DOI 10.1021/es403688w, DOI	2014	8.27	2015	2020	
Wolch JR, 2014, LANDSCAPE URBAN PLAN, V125, P234, DOI 10.1016/j.landurbplan.2014.01.017, DOI	2014	33.51	2015	2020	
Ugolini F, 2020, URBAN FOR URBAN GREE, V56, P0, DOI 10.1016/j.ufug.2020.126888, DOI	2020	9.76	2021	2024	
Gascon M, 2015, INT J ENV RES PUB HE, V12, P4354, DOI 10.3390/ijerph120404354, DOI	2015	9.63	2017	2020	
van den Berg M, 2015, URBAN FOR URBAN GREE, V14, P806, DOI 10.1016/j.ufug.2015.07.008, DOI	2015	8.88	2017	2020	
James Peter, 2015, CURR EPIDEMIOLOG REP, V2, P131	2015	8.51	2017	2020	
de Vries S, 2013, SOC SCI MED, V94, P26, DOI 10.1016/j.socscimed.2013.06.030, DOI	2013	8.33	2015	2018	
Kabisch N, 2016, ECOL INDIC, V70, P586, DOI 10.1016/j.ecolind.2016.02.029, DOI	2016	8.22	2017	2022	
Wang D, 2015, LANDSCAPE URBAN PLAN, V133, P53, DOI 10.1016/j.landurbplan.2014.09.007, DOI	2015	8.14	2017	2020	
Haaland C, 2015, URBAN FOR URBAN GREE, V14, P760, DOI 10.1016/j.ufug.2015.07.009, DOI	2015	8.14	2017	2020	
Wen M, 2013, ANN BEHAV MED, V45, P18, DOI 10.1007/s12160-012-9426-x, DOI	2013	7.81	2015	2018	
White MP, 2013, PSYCHOL SCI, V24, P920, DOI 10.1177/0956797612464659, DOI	2013	7.81	2015	2018	
Richardson EA, 2013, PUBLIC HEALTH, V127, P318, DOI 10.1016/j.puhe.2013.01.004, DOI	2013	6.77	2015	2018	
Rigolon A, 2016, LANDSCAPE URBAN PLAN, V153, P160, DOI 10.1016/j.landurbplan.2016.05.017, DOI	2016	14.23	2019	2022	
Kabisch N, 2014, LANDSCAPE URBAN PLAN, V122, P129, DOI 10.1016/j.landurbplan.2013.11.016, DOI	2014	13.41	2017	2020	
Thompson CW, 2012, LANDSCAPE URBAN PLAN, V105, P221, DOI 10.1016/j.landurbplan.2011.12.015, DOI	2012	10.98	2015	2018	
Chen Y, 2020, LANDSCAPE URBAN PLAN, V204, P0, DOI 10.1016/j.landurbplan.2020.103919, DOI	2020	8.64	2021	2024	
La Rosa D, 2014, ECOL INDIC, V42, P122, DOI 10.1016/j.ecolind.2013.11.011, DOI	2014	7.93	2017	2020	
Xiao Y, 2017, LANDSCAPE URBAN PLAN, V157, P383, DOI 10.1016/j.landurbplan.2016.08.007, DOI	2017	7.42	2017	2020	
Villeneuve PJ, 2012, ENVIRON RES, V115, P51, DOI 10.1016/j.envres.2012.03.003, DOI	2012	6.92	2015	2018	
Dadvand P, 2012, ENVIRON INT, V40, P110, DOI 10.1016/j.envint.2011.07.004, DOI	2012	6.92	2015	2018	
Lee ACK, 2011, J PUBLIC HEALTH-UK, V33, P212, DOI 10.1093/pubmed/fdq068, DOI	2011	8.89	2015	2016	
Markevych I, 2017, ENVIRON RES, V158, P301, DOI 10.1016/j.envres.2017.06.028, DOI	2017	8.47	2021	2022	

Figure 9 Top 25 References with the Strongest Citation Bursts

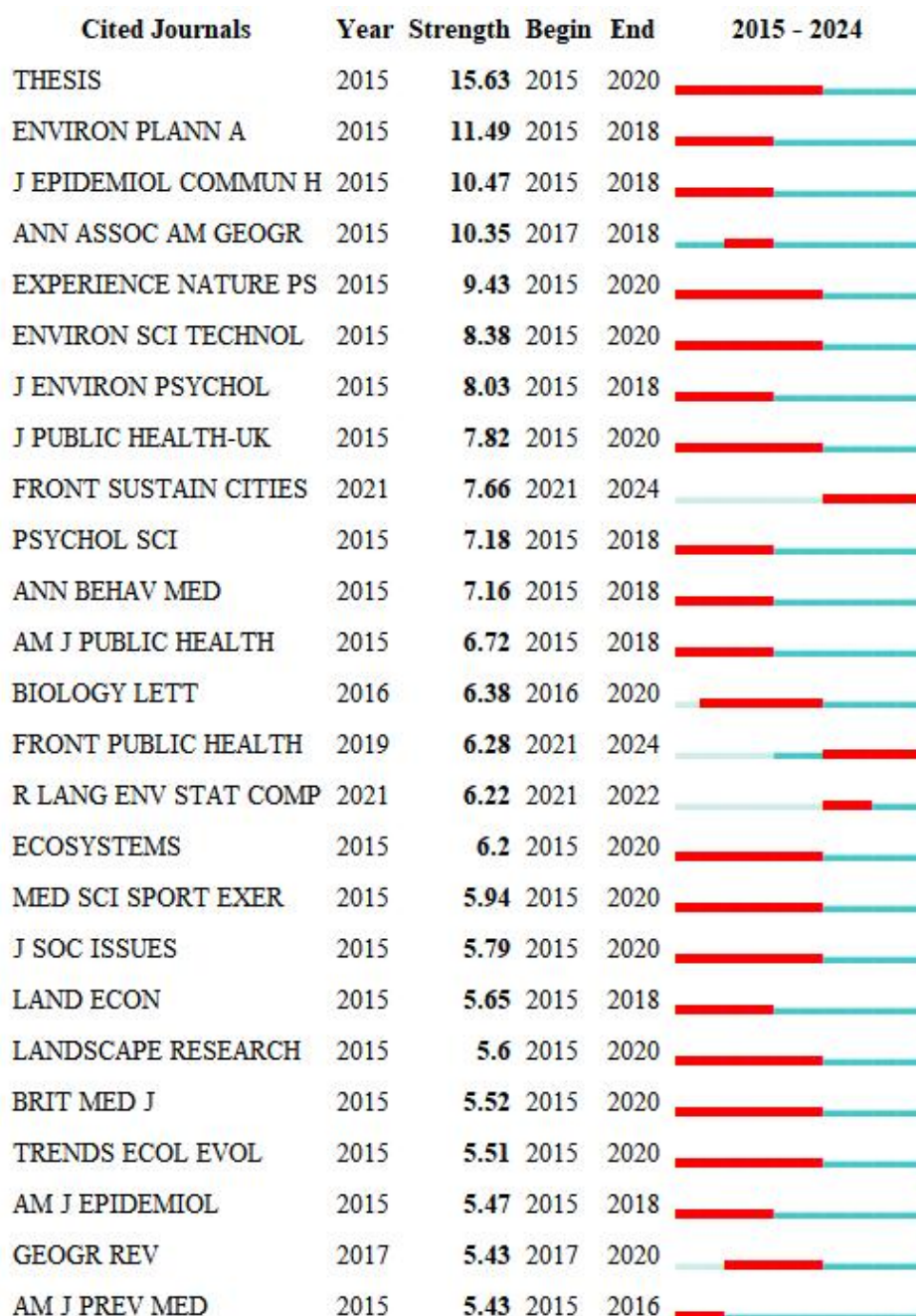


Figure 10 Top 25 Cited Journals with the Strongest Citation Bursts

5 CONCLUSION AND DISCUSSION

This study systematically reviews international research progress on urban recreational green space access from 2015 to 2024 based on bibliometric analysis methods. The research background focuses on the significant impact of urban green space access factors on residents' health, quality of life, and the urban environment. A total of 1,366 relevant literature items were retrieved through the Web of Science Core Collection, and after deduplication processing using CiteSpace, 1,002 valid literature items were retained. Knowledge mapping analysis was conducted using the CiteSpace tool to reveal research characteristics, hotspots, and trends in this field. The research results show that the number of literature items in this field has generally increased over the past decade, reaching a peak in 2021. Major publishing institutions include Pompeu Fabra University, Arizona State University, etc. However, the density of collaboration networks among these institutions is low, indicating that academic collaboration needs to be strengthened. Analysis of cited literature citations shows that fields such as medicine, public/environmental and occupational health, meteorology and atmospheric sciences, and ecology have significant academic influence in research on recreational green space access, focusing on issues such as medical tourism, the restorative effects of green spaces on mental health, air quality dynamics, and ecological landscape planning.

Analysis of research hotspots and trends reveals that research in this field exhibits interdisciplinary linkage characteristics. The core directions include urban green spaces and health promotion, the provision of ecosystem

services by green infrastructure, socio-spatial differentiation and governance of urban greening, and behavioral response mechanisms of emotion-environment interaction. Furthermore, accessibility, as a key factor influencing residents' access to green spaces, is closely related to the fairness of green space resource distribution, residents' health levels, and quality of life. The conclusion points out that research on urban recreational green space access has made significant progress over the past decade, particularly in analyzing the relationship between green spaces and health, assessing the comprehensive benefits of green infrastructure, and diagnosing socio-spatial differentiation. Future research needs to further strengthen interdisciplinary cooperation, explore technology-driven sustainable development paths, and promote innovation at the policy practice level to achieve equitable distribution and efficient utilization of urban green space resources.

COMPETING INTERESTS

The authors have no relevant financial or non-financial interests to disclose.

FUNDING

This research was supported by 2024 Zhaoqing City Philosophy and Social Science 14th Five-Year Plan Project (24GJ-209) and 2024 Guangdong Technology College's University-level Research Platforms and Projects (2024YBZK003).

REFERENCES

- [1] Li X, Huang Y, Ma X. Evaluation of the accessible urban public green space at the community-scale with the consideration of temporal accessibility and quality. *Ecological Indicators*, 2021,131:108231.
- [2] Bele A, Chakradeo U. Public perception of biodiversity: a literature review of its role in urban green spaces. *Journal of Landscape Ecology*, 2021,14(2):1-28.
- [3] Bille R A, Jensen K E, Buitenwerf R. Global patterns in urban green space are strongly linked to human development and population density. *Urban Forestry & Urban Greening*, 2023,86:127980.
- [4] Pinto L V, Inácio M, Ferreira C S S, et al. Ecosystem services and well-being dimensions related to urban green spaces—A systematic review. *Sustainable Cities and Society*, 2022,85:104072.
- [5] Wang Z, Zhu Z, Xu M, et al. Fine-grained assessment of greenspace satisfaction at regional scale using content analysis of social media and machine learning. *Science of the Total Environment*, 2021,776:145908.
- [6] Xie X, Jiang Q, Wang R, et al. Correlation between vegetation landscape and subjective human perception: a systematic review. *Buildings*, 2024,14(6):1734.
- [7] Wang P, Zhou B, Han L, et al. The motivation and factors influencing visits to small urban parks in Shanghai, China. *Urban forestry & urban greening*, 2021,60:127086.
- [8] Kiplagat A K, Koech J K, Ng'Etich J K, et al. Urban green space characteristics, visitation patterns and influence of visitors' socio-economic attributes on visitation in Kisumu City and Eldoret Municipality, Kenya. *Trees, Forests and People*, 2022,7:100175.
- [9] Zhang L, Cao H, Han R. Residents' preferences and perceptions toward green open spaces in an urban area. *Sustainability*, 2021,13(3):1558.
- [10] Nasri Roodsari E, Hoseini P. An assessment of the correlation between urban green space supply and socio-economic disparities of Tehran districts—Iran. *Environment, development and sustainability*, 2022,24(11):12867-12882.
- [11] Donthu N, Kumar S, Mukherjee D, et al. How to conduct a bibliometric analysis: An overview and guidelines. *Journal of business research*, 2021,133:285-296.
- [12] Mu J, Chen Y, Yang G. A scientometric analysis of research advances in China's eco-translatology studies (2008-2021). *Open Access Library Journal*, 2021,8(9):1-11.
- [13] Zhong Q, Han L, Ye X, et al. Effects of green space exposure on acute respiratory illness in community-dwelling older people: A prospective cohort study. *Landscape and Urban Planning*, 2025,258:105336.
- [14] Sharifi Y, Sobhani S, Ramezanghorbani N, et al. Association of greenspaces exposure with cardiometabolic risk factors: a systematic review and meta-analysis. *BMC Cardiovascular Disorders*, 2024,24(1):170.
- [15] Hsu Y, Hawken S, Sepasgozar S, et al. Beyond the backyard: GIS analysis of public green space accessibility in Australian metropolitan areas. *Sustainability*, 2022,14(8):4694.
- [16] Zhang C, Wang C, Chen C, et al. Effects of tree canopy on psychological distress: A repeated cross-sectional study before and during the COVID-19 epidemic. *Environmental research*, 2022,203:111795.
- [17] Niu L, Zhang Z, Liang Y, et al. Assessing the impact of urbanization and eco-environmental quality on regional carbon storage: A Multiscale Spatio-Temporal Analysis Framework. *Remote Sensing*, 2022,14(16):4007.
- [18] Joy N M, Paul S K. Analysis of the economic value and status of the ecosystem services provided by the Ashtamudi Wetland Region, a Ramsar Site in Kerala. *Journal of the Indian Society of Remote Sensing*, 2021,49:897-912.
- [19] Antunes L N, Araújo A R M D, Bet M F, et al. Implementing green infrastructure for stormwater management and combined sewer overflow control. *International Journal of Environment and Sustainable Development*, 2023,22(1):32-50.

-
- [20] Anguelovski I, Connolly J J, Cole H, et al. Green gentrification in European and North American cities. *Nature communications*, 2022,13(1):3816.
 - [21] Nesbitt L, Meitner M J, Girling C, et al. Who has access to urban vegetation? A spatial analysis of distributional green equity in 10 US cities. *Landscape and Urban Planning*, 2019,181:51-79.
 - [22] Sabater-Mir J. Optimising Participatory Budget: Artificial Intelligence Research and Development: Proceedings of the 22nd International Conference of the Catalan Association for Artificial Intelligence, 2019.

FAULT DIAGNOSIS METHOD OF AERO-ENGINE ROLLING BEARINGS BASED ON TIME-FREQUENCY ANALYSIS AND MACHINE LEARNING

YeQi Jin

*College of Aerospace Engineering, Shenyang Aerospace University, Shenyang 110136, Liaoning, China.
Corresponding Email: 18624306466@163.com*

Abstract: As a crucial component of aircraft, aero-engine bearings operate under extreme conditions such as high temperature, high pressure, and high rotational speed, making them highly prone to failure, which seriously affects aviation safety. Traditional bearing fault diagnosis methods suffer from problems such as low diagnostic accuracy and poor real-time performance, and it is difficult to meet the requirements of modern aviation industry for high reliability and safety of engines. With the development of machine learning technology, this paper proposes a fault diagnosis method for aero-engine bearings based on machine learning. Firstly, time-domain and frequency-domain features of vibration data are extracted, and dimensionality reduction processing is carried out through principal component analysis (PCA) to reduce data complexity and retain key information. Subsequently, machine learning models such as logistic regression, K-Nearest Neighbor (KNN), Support Vector Machine (SVM), and decision tree are used for fault prediction, and a comparative analysis is conducted with deep learning models. The experimental results show that the Support Vector Machine (SVM) performs best in the fault classification task, with an accuracy rate of 99%. This research provides an efficient and accurate solution for aero-engine bearing fault diagnosis and has important practical application value.

Keywords: Aero-engine bearings; Fault diagnosis; Machine learning; PCA; SVM; Time-domain and frequency-domain features

1 INTRODUCTION

As the core component of an aircraft, the reliability and safety of an aero-engine's operation are directly related to the normal operation of air transportation and the safety of passengers[1]. Aero-engine bearings are crucial and indispensable parts in the engine. They continuously operate under extreme working conditions such as high temperature, high pressure, and high rotational speed, bear complex and variable loads, and are prone to failure, which can cause serious accidents. Therefore, in-depth research on the fault diagnosis of aero-engine inter-shaft bearings, and using advanced technical means to detect bearing fault hidden dangers in a timely and accurate manner, can not only ensure the safe and stable operation of aero-engines, but also provide strong support for the design optimization and life prediction of aero-engines. It is of great significance for promoting the high-quality development of the aviation industry[2].

At present, traditional bearing fault diagnosis methods often have problems such as low diagnostic accuracy, poor real-time performance, and difficulty in effectively identifying early-stage faults when dealing with aero-engine bearing faults. They cannot meet the strict requirements of modern aviation for the high reliability and safety of engines[3]. With the development of emerging technologies such as machine learning, new opportunities have emerged for aero-engine bearing fault diagnosis[4]. Zhang Jian and Qian Haiting[5] used three common classifiers, namely Support Vector Machine (SVM), decision tree, and random forest, to classify and learn bearing vibration data, and evaluated their performance in bearing vibration data classification. Cheng Xiang[6], in order to solve problems such as complex background noise of bearings in industrial environments, small amounts of fault data acquisition, and difficulty in detailed analysis of fault states, adopted a signal denoising algorithm combined with a machine learning algorithm to monitor bearing vibration signals for faults. Cai Zhengyin[7] conducted research around traditional signal processing and machine learning, proposed an Adaptive Variational Mode Decomposition (IVMD) method and an improved scheme combining multiple technologies to solve problems in the application of traditional signal processing and Support Vector Machine (SVM), and verified the effectiveness of the method through multiple datasets.

In summary, this paper proposes a bearing fault diagnosis method that combines time-domain and frequency-domain feature extraction, and reduces the dimensionality of feature data through Principal Component Analysis (PCA) to retain key information to the greatest extent while reducing the data dimension. This method can not only effectively handle the complexity of high-dimensional data, but also improve the computational efficiency and prediction performance of subsequent fault diagnosis models. Secondly, this paper uses traditional machine learning algorithms (such as logistic regression, KNN, SVM) to explore the applicability, advantages, and disadvantages of different models in aero-engine bearing fault diagnosis, providing a reference for future fault diagnosis technologies. Finally, for the optimization of model hyperparameters, this paper adopts a combination of grid search and 5-fold cross-validation to finely adjust hyperparameters, significantly improving the classification accuracy and demonstrating the importance of parameter adjustment for model performance. Through these innovations, this paper not only provides an efficient and

accurate solution for aero-engine bearing fault diagnosis, but also provides theoretical support and practical guidance for future research in related fields.

2 PRINCIPLE AND MODEL BUILDING

2.1 Time-domain Feature and Frequency-domain Feature Extraction

When differentiating the fault types of aero-engine bearings, time-domain features and frequency-domain features are usually combined as the fault evaluation criteria. The time-domain features include mean value, variance, peak value, root mean square (RMS) value, root amplitude, margin, kurtosis index, waveform factor, impulse value, and peak factor. The frequency-domain features, on the other hand, consist of mean frequency, centroid frequency, root mean square frequency, standard deviation frequency, and kurtosis frequency. Through a comprehensive analysis of these features, the fault types can be judged more accurately[8].

2.2 RobustScaler Outlier Handling

2.2.1 Algorithm features, advantages, and application scenarios

RobustScaler is a data standardization method based on statistical characteristics, mainly used to handle datasets containing outliers. Its main feature lies in its robustness to outliers. Different from traditional standardization methods (such as Z-score standardization), RobustScaler uses the median instead of the mean as the central value and the interquartile range (IQR) instead of the standard deviation as the scaling scale. Moreover, it does not change the overall distribution shape of the data during the scaling process, making it particularly suitable for non-normally distributed data. RobustScaler is applicable to various data types and makes few assumptions about the data distribution. The advantages of RobustScaler are mainly reflected in its robustness to outliers and wide applicability. Due to the use of the median and IQR, RobustScaler is insensitive to extreme values and can effectively reduce the impact of outliers on data scaling. During the scaling process, RobustScaler can preserve the original structure of the data, making it suitable for machine-learning tasks that require maintaining data characteristics, such as clustering and classification. It is one of the important tools in data pre-processing.

2.2.2 Calculation formula

Median: The median is the middle value after the data is sorted. For a datasets with an odd number of data points, the median is the middle value. For a datasets with an even number of data points, the median is the average of the twomiddle values. Its mathematical definition is as follows:

$$Median(X) = \begin{cases} X_{\frac{n+1}{2}} & \text{if } n \text{ is odd} \\ \frac{X_{\frac{n}{2}} + X_{\frac{n}{2}+1}}{2} & \text{if } n \text{ is even} \end{cases} \quad (1)$$

Inter-Quartile Range (IQR): The IQR is the difference between the 75th percentile $Q_3(X)$ and the 25th percentile $Q_1(X)$, which is used to measure the degree of data dispersion. Its mathematical definition is:

$$IQR(X) = Q_3(X) - Q_1(X) \quad (2)$$

Given a datasets $X = \{x_1, x_2, \dots, x_n\}$ where x_i is a feature vector, the standardization process of RobustScaler can be divided into the following two steps.

(1) Centering:

Center the data using the median. For each feature , calculate its median $Median(X_j)$, And subtract the median from the data:

$$x_{ij}^{centered} = x_{ij} - Median(X_j) \quad (3)$$

Here, x_{ij} represents the j-th feature value of the i-th sample.

(2) Scaling:

Scale the data using the Inter-Quartile Range (IQR). For each feature j, calculate its IQR:

$$IQR(X_j) = Q_3(X_j) - Q_1(X_j) \quad (4)$$

where $Q_3(X_j)$ and $Q_1(X_j)$ are the 75th percentile and the 25th percentile of the j-th feature respectively. Then divide the centered data by the IQR.

$$x_{ij}^{scaled} = \frac{x_{ij}^{centered}}{IQR(X_j)} \quad (5)$$

Finally, the standardized data x^{scaled} can be expressed as:

$$x^{scaled} = \frac{X - Median(X)}{IQR(X)} \quad (6)$$

2.3 KNN

The K-Nearest Neighbors (KNN) algorithm is an instance-based non-parametric classification algorithm. Its core idea is to calculate the distances between the sample to be classified and the known samples, find the K closest neighbors, and then determine the class of the sample to be classified based on the classes of these neighbors. The problem of engine fault classification involves analyzing the sensor signals collected under various working conditions and determining the fault type according to their characteristic patterns.

Given a training sample set $D = \{(x_1, y_1), (x_2, y_2), \dots, (x_n, y_n)\}$, where x_i represents the feature vector, and $y_i \in \{1, 2, \dots, C\}$ represents the sample class. For a sample to be classified x , the steps of KNN are as follows:

1. Distance calculation

Calculate the distances between x (the sample to be classified) and all the samples in the training set. The most commonly used distance metric is the Euclidean distance, and its formula is as follows:

$$d(x, x_i) = \sqrt{\sum_{j=1}^m (x_j - x_{ij})^2} \quad (7)$$

Where m is the number of feature dimensions, and x_j and x_{ij} are the feature values of the sample x and the x_i sample in the training set in the j -th dimension respectively.

2. Select the nearest neighbor samples

Sort the samples in ascending order of distance and select the K samples with the shortest distances $S \subseteq D$.

3. Classification decision

Count the number of samples of each class among the S . Adopt the principle of "the minority is subordinate to the majority", and predict the class of the sample x to be the class that appears most frequently:

$$\hat{y} = \arg \max_{c \in \{1, \dots, C\}} \sum_{x_i \in S} \mathbb{I}(y_i = c) \quad (8)$$

Where $\mathbb{I}(\cdot)$ is an indicator function. If the condition holds, its value is 1; otherwise, it is 0.

2.4 SVM

The core idea of SVM is to find a classification hyperplane that maximizes the margin between different classes. For linearly separable data, the classification problem can be expressed as the following optimization problem:

$$\min_{\omega, b} \frac{1}{2} \|\omega\|^2 + C \sum_{i=1}^n \xi_i \quad (9)$$

Constraints:

$$y_i(\omega \cdot \phi(x_i) + b) \geq 1 - \xi_i, \quad \xi_i \geq 0, \quad i = 1, \dots, n \quad (10)$$

Among them, ω and b are the hyperplane parameter, ξ_i is the slack variable, C is the penalty coefficient, and $\phi(x_i)$ represents the kernel function mapping.

To deal with the non-linear distribution of fault signals, the Gaussian kernel function can be used here:

$$K(x_i, x_j) = \exp\left(-\frac{\|x_i - x_j\|^2}{2\sigma^2}\right) \quad (11)$$

Among them, σ controls the bandwidth of the Gaussian kernel function.

2.5 Decision Tree

A decision tree constructs a classification model by recursively splitting the sample space. Each split is based on a certain feature and its threshold to maximize the class purity of the samples after the split. The specific process of the algorithm is as follows:

1. Splitting criterion

At each node, the feature and its threshold that maximize the Information Gain or Gini Index are selected for splitting. The Information Gain is defined as follows:

$$IG(D, A) = H(D) - \sum_{v \in \text{Values}(A)} \frac{|D_v|}{|D|} H(D_v) \quad (12)$$

Among them, $H(D)$ is the information entropy of the node datasets D , A is the splitting feature, and D_v is the subset where the feature A takes the value v .

The Gini Index is defined as follows:

$$Gini(D) = 1 - \sum_{k=1}^K p_k^2 \quad (13)$$

Among them, p_k represents the proportion of samples in class k .

2. Stopping condition

The splitting stops when all samples belong to the same class, the number of features is insufficient, or the number of samples at a node is lower than the preset threshold.

3. Prediction stage

When inputting features x , start from the root node and select a path layer by layer downward according to the feature values. Finally, reach a leaf node and output the predicted class.

3 RESULTS

3.1 Data Sources

The datasets selected in this paper is from the Bearing Data Center of Case Western Reserve University (CWRU). This datasets comprehensively records four main types of faults: inner-race faults, outer-race faults, rolling-element faults, and normal operating states. Some illustrations are shown in Figure 1. For each type of fault, the datasets provides samples with four different fault diameters (0.007 inches, 0.014 inches, 0.021 inches, and 0.028 inches respectively). All the data were collected at a sampling rate of 12 kHz.

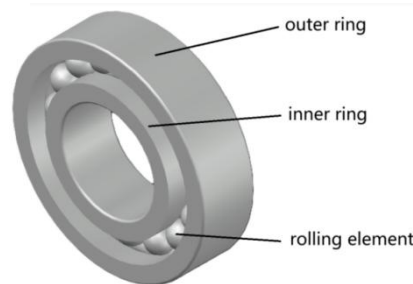


Figure 1 Bearing Fault Illustration

After the data collection work was completed, this paper used a variety of Python libraries to conduct a preliminary visual analysis of the obtained raw data. Due to the limitation of the article's length, only the visual graphs of partial data are presented here, as shown in Figure 2.

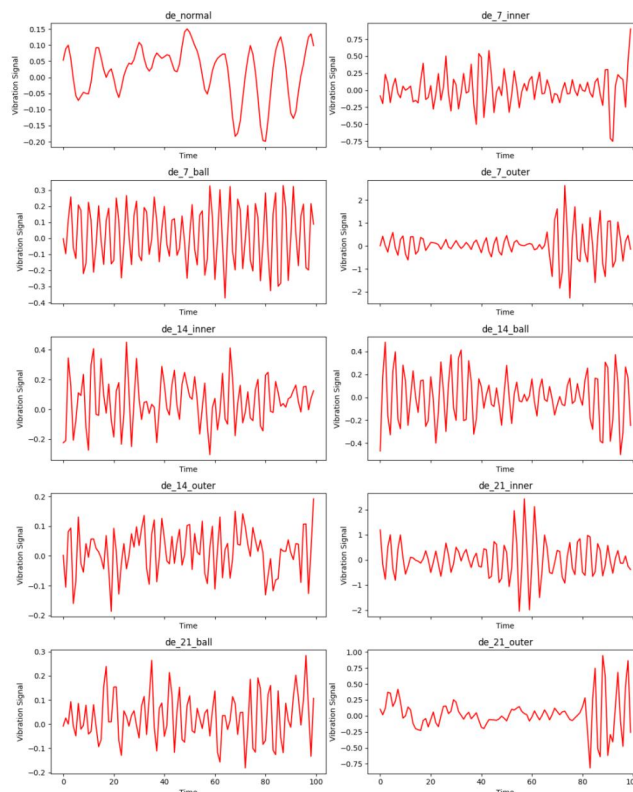


Figure 2 Part of Working Condition Data Visualization

Observe the curves of the four different types of vibration signals changing over time shown in the Figure 2. The amplitudes and frequencies of these signals both exhibit certain fluctuations, and at the same time, they also show a certain degree of periodicity and repeatability.

To optimize the processing and analysis of the original bearing vibration data, this paper divides every 1024 data points into a sample block for subsequent operations. This length approximately represents the time interval for the bearing to rotate three times. It can capture most of the key vibration information and effectively control the scale of data processing, as shown in Figure 3.

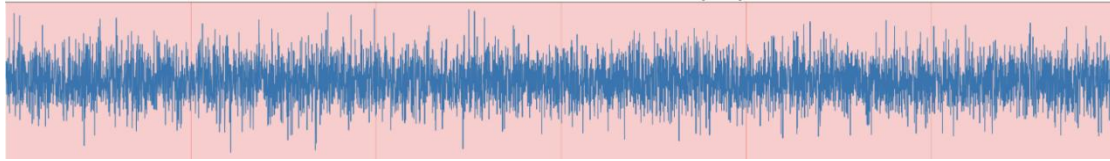


Figure 3 Schematic diagram of sliding window segmentation

Subsequently, to visually display the quantitative relationship among samples of different fault categories, this paper uses Figure 4 for visualization.

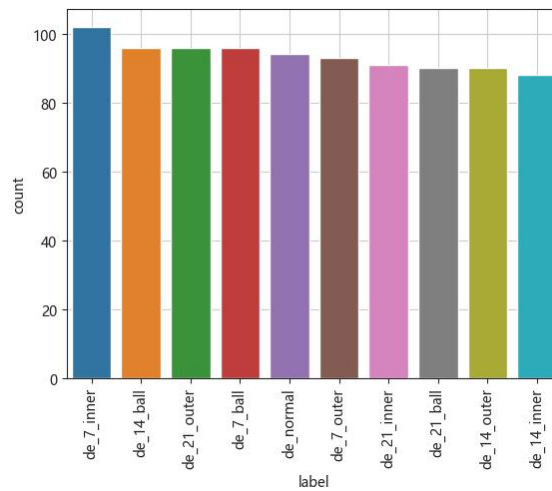


Figure 4 Number of Samples of Different Fault Categories

By observing Figure 4, it can be found that the quantity distribution of samples for each type of fault is relatively balanced. This indicates that the datasets is relatively evenly distributed among different classes, and there is no obvious imbalance.

3.2 Data Preprocessing

3.2.1 Time-domain and frequency-domain characteristics

To evaluate whether there are outliers in the time-domain and frequency-domain features (such as mean, standard deviation, and mean frequency) extracted from the original datasets, this paper uses box plots for intuitive detection. The box plots corresponding to some features are shown in Figure 5.

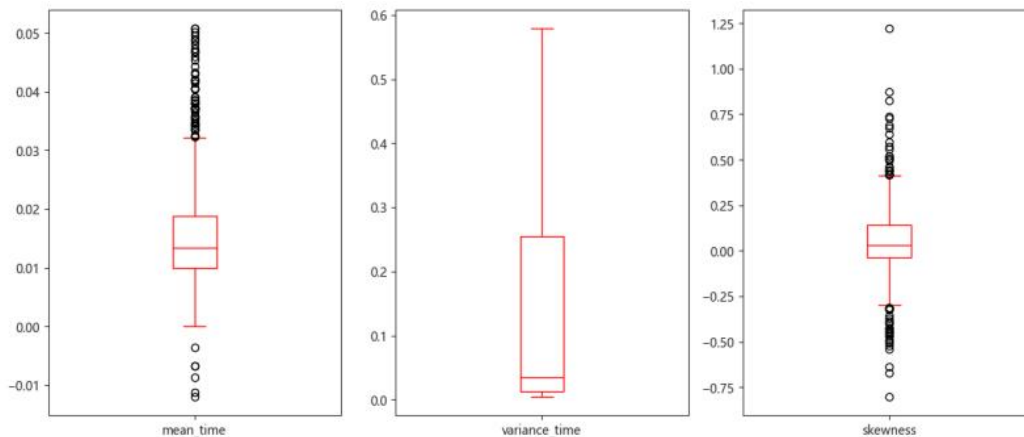


Figure 5 Box View of Some Features

When conducting an in-depth analysis of the data distribution presented in Figure 5, it is noted that there are significant outliers in some variables. For example, in the features of "skewness" and "kurtosis", the number of outliers is particularly prominent, and their degree of deviation far exceeds the average level of other variables. The presence of such outliers may have an adverse impact on the subsequent data analysis and modeling processes, leading to inaccurate or biased results.

Therefore, to ensure the reliability and accuracy of the data analysis results, this paper uses the RobustScaler method to handle these outliers.

3.3 Prediction Results of the Aero-engine Bearing Fault Classification Model Based on Machine Learning

3.3.1 Model Structure

When using machine learning-related algorithms, the training set input consists of the extracted time-domain and frequency-domain features. The PCA method is adopted to reduce the dimensionality of the data. During model training, algorithms such as logistic regression, KNN, SVM, and decision tree are used to train the model respectively. The pipeline is employed to integrate the models, and the model structure obtained is shown in Figure 6.

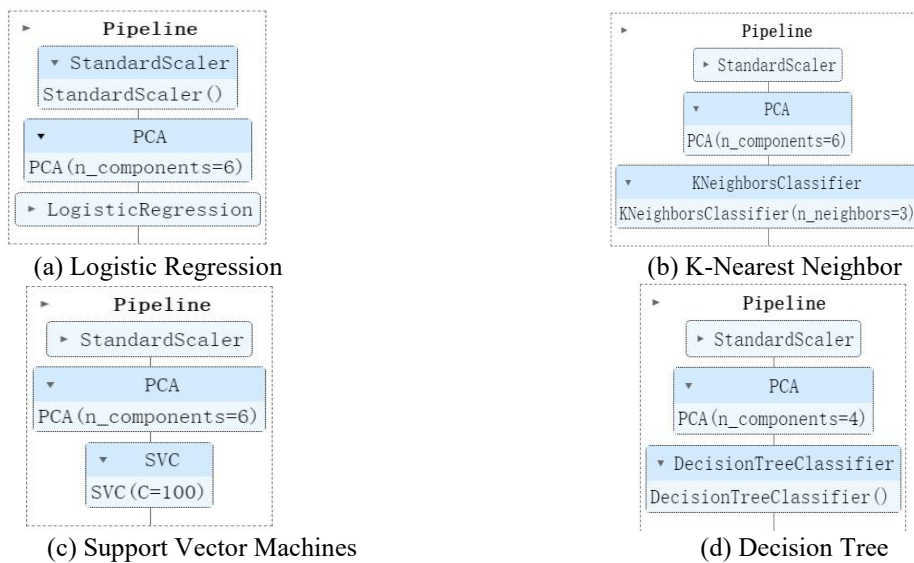
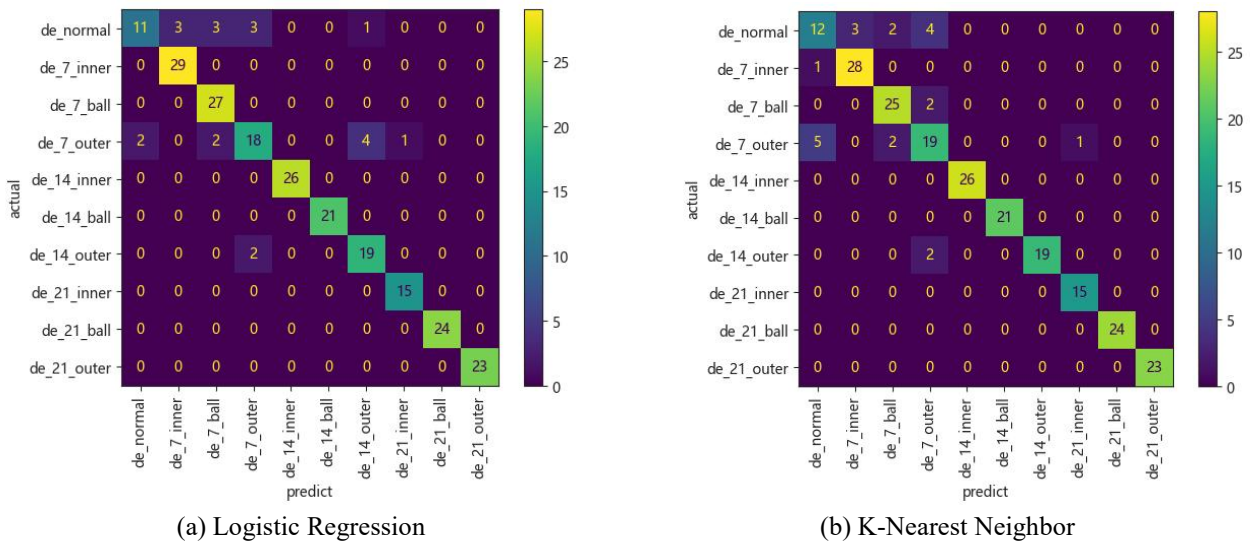


Figure 6 Structure of Each Machine Learning Models

3.3.2 Model prediction results

Bring the well-trained model into the test set, and the resulting confusion matrix is shown in Figure 7. In addition, the corresponding accuracy, precision, recall, and F1-score of the model are shown in Table 1.



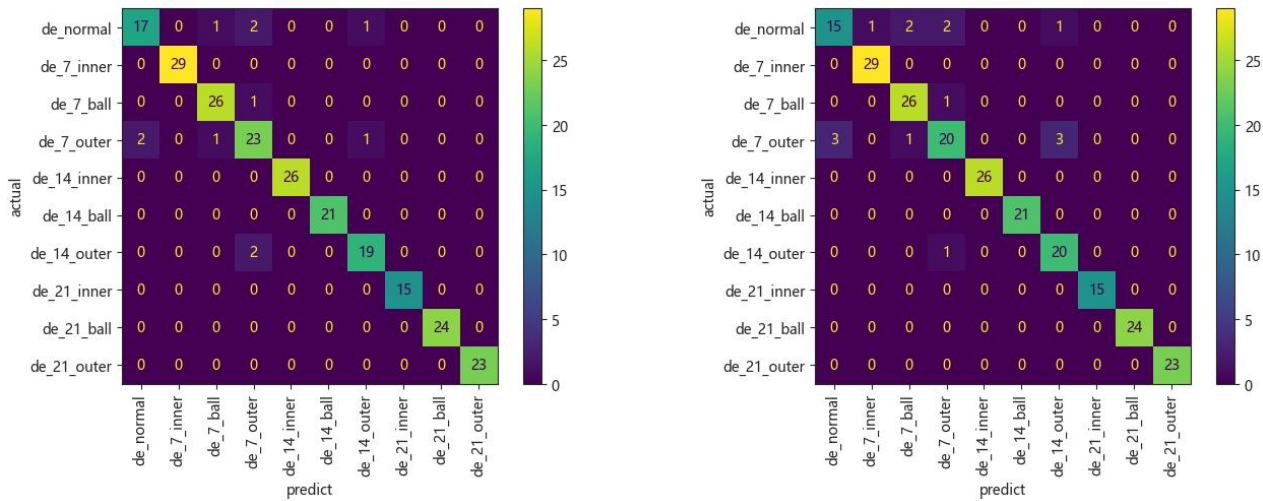


Figure 7 Confusion Matrix for Machine Learning Models

Table 1 Performance Comparison of Classification Algorithms

Model	Accuracy	Precision	Recall	F1-Score
LR	0.95	0.95	0.95	0.95
KNN	0.96	0.96	0.96	0.96
SVM	0.99	0.99	0.99	0.99
DT	0.96	0.96	0.96	0.96

After comparison, it's not difficult to find that in the current situation, the Support Vector Machine(SVM) algorithm has the best overall performance.

4 CONCLUSIONS

This study deeply analyzes the bearing vibration data and reveals the effectiveness and universality of machine learning algorithms such as logistic regression, KNN, and SVM for fault diagnosis. The PCA method is adopted for dimensionality reduction, which not only retains the main variation information of the data but also improves the computational efficiency and prediction performance of the model. The hyperparameters are optimized through grid search and 5-fold cross-validation, which proves the effectiveness of this method. Moreover, the optimal hyperparameter combination can significantly improve the classification accuracy.

In practical applications, the research results of this study have wide applicability in the fields of industrial equipment fault diagnosis and predictive maintenance. They can reduce costs and downtime while enhancing the reliability and safety of equipment operation.

Meanwhile, traditional machine learning methods have problems such as high computational costs and difficulty in capturing non-linear relationships when dealing with large-scale high-dimensional data. It is crucial to introduce deep-learning methods in the future. Models like CNN, RNN, and LSTM have strong automatic feature extraction capabilities. Autoencoders, combined with various techniques, can improve the model performance to achieve more efficient and intelligent industrial production.

COMPETING INTERESTS

The authors have no relevant financial or non-financial interests to disclose.

REFERENCES

- [1] Li Dongjun, Li Ya, Li Dongwen, et al. Remaining useful life prediction of aero-engines based on MIC feature extraction and BO-CatBoost. Journal of Air Force Engineering University, 2024, 25(01): 31-38.
- [2] Sha Yundong, Zhao Junhao, Luan Xiaochi, et al. A fault identification method for main bearings based on multi-feature parameter fusion and dimensionality reduction. Journal of Shenyang Aerospace University, 2024, 41(05): 15-25.
- [3] Yin Kang. Research on Fault Diagnosis Algorithms for Aero-engine Bearings and Design of Fault Diagnosis Software. Supervisor: Zhang Weitao; Sun Xiaochao. Xidian University, 2021: 17-34.
- [4] Liu Junli. Research on Fault Diagnosis and Remaining Useful Life Prediction Methods for Rolling Bearings Based on Machine Learning. Southwest Jiaotong University, 2023: 10-23.

-
- [5] Zhang Jian, Qian Haiting. Classification and Performance Comparative Analysis of Bearing Vibration Data Based on Machine Learning. *China Tire Resources Comprehensive Utilization*, 2025(01): 163-165.
 - [6] Cheng Xiang. Research on Fault Diagnosis of Rolling Bearings Based on Machine Learning. *Anhui University of Science and Technology*, 2024: 10-17.
 - [7] Cai Zhengyin. Research on Fault Diagnosis of Rolling Bearings Based on Vibration Signal Processing and Machine Learning. *Heilongjiang University*, 2024: 10-16.
 - [8] Zhang Weitong. Research on fault diagnosis of aero engine bearing based on unbalance dataset. *Harbin Engineering University*, 2023: 10-19.

THE FLOW AND COMPONENT VARIATION CHARACTERISTICS OF THE HYDROGEN SUPPLY SYSTEM IN FUEL CELLS

JingGuang Xie^{1*}, NanNan Liao¹, JianHua Liu¹, Jun Li¹, YaNan Gao²

¹CRRC Qishuyan Co., Ltd, Changzhou 213000, Jiangsu, China.

²Department of Economic Research, CRRC Academy Co., Ltd, Beijing 100070, China.

Corresponding Author: JingGuang Xie, Email: xiejingguang.qj@crrecg.cc

Abstract: Nitrogen gas on the cathode side of the fuel cell permeates to the anode and accumulates due to the concentration gradient, reducing the hydrogen concentration and leading to localized fuel starvation at the anode. The hydrogen, nitrogen, and water vapor concentrations, as well as the flow rate in the hydrogen circulation loop, can be monitored online using ultrasonic sensors. This study investigates the component variation in the anode circulation loop of the fuel cell system through experimental methods and analyzes its impact on output performance. The results show that as the current density increases, the water vapor concentration gradually increases. The hydrogen concentration at the anode remains between 70% and 75% across different current densities, while the nitrogen concentration remains around 20% to 25%. With the increase in current density, the time interval for opening the drainage valve gradually shortens, which is attributed to the increasing water production in the cell.

Keywords: Fuel cell; Anode circulation components; Nitrogen concentration; Ultrasonic flow meter

1 INTRODUCTION

Proton Exchange Membrane Fuel Cells (PEMFCs) convert the chemical energy of hydrogen fuel into electrical energy through electrochemical reactions, offering an ideal method for hydrogen utilization. They have garnered significant attention due to their low operating pressure and temperature, high power density, high efficiency, and low emissions, making them more favorable than other types of fuel cells [1-3]. The anode hydrogen supply system is one of the subsystems of PEMFCs, primarily involving hydrogen supply and consumption, mixed gas recirculation, and discharge [4]. The hydrogen supply system provides the required flow and pressure for the fuel cell stack reactions. The hydrogen flow rate and pressure directly impact the output performance of the fuel cell system. Insufficient hydrogen flow can cause localized fuel starvation within the stack, reducing its performance, while excessive hydrogen supply can lead to fuel wastage. Therefore, a well-designed hydrogen supply system is crucial to meet the required hydrogen flow and pressure demands of the fuel cell system.

In addition, nitrogen gas on the cathode side permeates to the anode under the influence of the concentration gradient [5]. Water also diffuses from the cathode to the anode and accumulates there, covering the gas diffusion layer and catalyst layer. This impairs hydrogen transport, hinders the reaction between hydrogen and the catalyst layer, leading to localized fuel starvation at the anode, causing carbon corrosion in the catalyst layer, and promoting catalyst degradation, which ultimately results in fuel cell performance degradation. Therefore, it is necessary to install an exhaust electromagnetic valve at the anode outlet.

Based on the hydrogen flow modes, the hydrogen supply system is primarily classified into three types: hydrogen direct discharge mode, dead-end mode, and recirculation mode [6-8]. Currently, the recirculation mode is the most widely used hydrogen flow mode in fuel cell systems. During recirculation the accumulation of nitrogen on the anode side gradually reduces the hydrogen concentration, thereby lowering the fuel cell's output performance. Therefore, this study investigates the component variations in the anode circulation loop of the fuel cell system through experimental methods and analyzes their impact on output performance.

2 SYSTEM DESIGN

2.1 System Schematic Design

Figure 1 shows the structural diagram of the hydrogen supply system, including a medium-pressure solenoid valve, a proportional valve, a hydrogen recirculation pump, a water separator, a drainage valve, and an ultrasonic flow sensor. The medium-pressure solenoid valve controls the on/off operation of the hydrogen supply system; the proportional valve regulates the pressure of hydrogen entering the fuel cell stack; the water separator separates the mixed water vapor from the anode exhaust of the fuel cell stack. The separated mixture (hydrogen, nitrogen, and water vapor) is recirculated into the anode inlet of the stack via an injector or hydrogen recirculation pump, allowing unreacted hydrogen to re-enter the reaction, thus improving hydrogen utilization. The drainage valve, located at the bottom of the water separator, periodically opens and closes to discharge the accumulated liquid water and nitrogen from the anode side of the fuel cell stack.

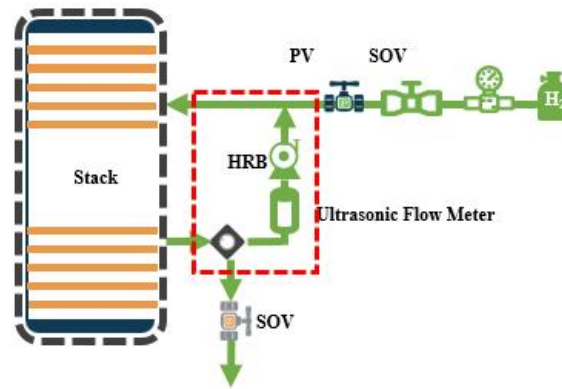


Figure 1 Schematic Diagram of the Fuel Cell Hydrogen Supply System

2.2 Ultrasonic Flow Sensor

The ultrasonic flow sensor can simultaneously measure the flow rate and concentration of hydrogen gas in real-time under high humidity conditions. Additionally, the sensor is capable of collecting temperature, pressure, and humidity data, making it suitable for testing the hydrogen circulation loop in fuel cell systems. Figure 2 shows the physical image of the ultrasonic sensor.



Figure 2 The Physical Image of the Ultrasonic Sensor

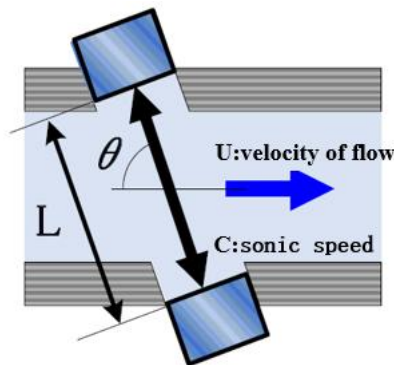


Figure 3 The Working Principle of the Ultrasonic Hydrogen Concentration Sensor

Figure 3 is a schematic diagram of the internal structure of the sensor. The measurement principle is based on detecting the sound velocity and flow velocity of the gas passing through the sensor to calculate the flow rate and concentration of the mixed gas. The calculation formulas are shown in equations (1-3):

$$U = \frac{L}{2\cos\theta} \left(\frac{1}{t_1} - \frac{1}{t_2} \right) \quad (1)$$

$$Q = U \times S \quad (2)$$

$$M = \frac{\gamma \times R \times T}{C^2} \quad (3)$$

Where U is the gas flow velocity, L is the distance between the two ultrasonic probes, θ is the tilt angle of the ultrasonic probes, t_1 and t_2 are the incident and reflection times of the ultrasonic wave, S is the gas flow cross-sectional area, Q is the gas flow rate, M is the gas concentration, R is the universal gas constant, T is the gas temperature, C is the gas sound speed, and γ is the correction factor.

To prevent liquid water from adhering to the ultrasonic sensor probes and affecting measurement accuracy, the ultrasonic sensor is vertically installed and wrapped in thermal insulation cotton. As shown in Figure 4, the ultrasonic

hydrogen concentration sensor is installed between the water separator outlet and the hydrogen recirculation pump inlet pipeline.

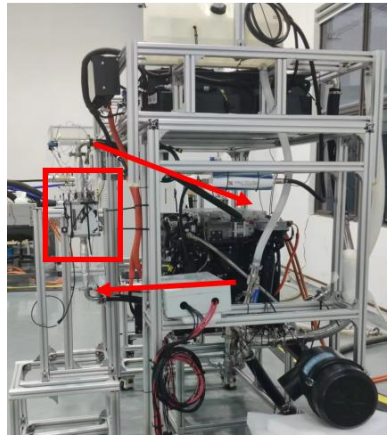


Figure 4 Schematic Diagram Showing the Installation Position of the Ultrasonic Hydrogen Concentration Sensor

3 DATA ANALYSIS

3.1 Sensor Accuracy Verification

Before conducting the fuel cell system experiments, the measurement accuracy of the ultrasonic sensor was verified. The ultrasonic flow sensor was serially connected with a calibrated Ellicott flow meter on the same pipeline, and tests were performed using hydrogen and nitrogen as media, measuring the values of both sensors at different inlet flow rates. The measurement results are shown in Figures 5 and 6. It can be observed that the measurement error between the ultrasonic flow sensor and the Ellicott flow meter does not exceed 1%, which is within the acceptable error range and meets the experimental requirements.

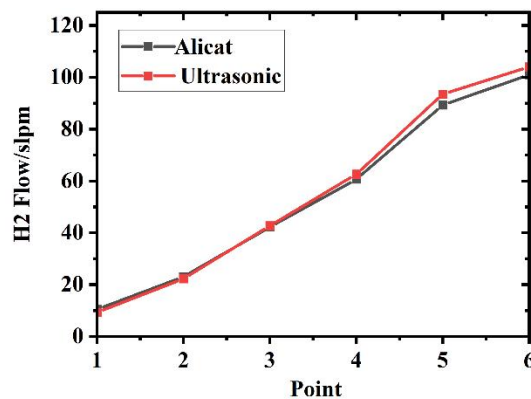


Figure 5 The Hydrogen Flow Rates Measured by Different Sensors

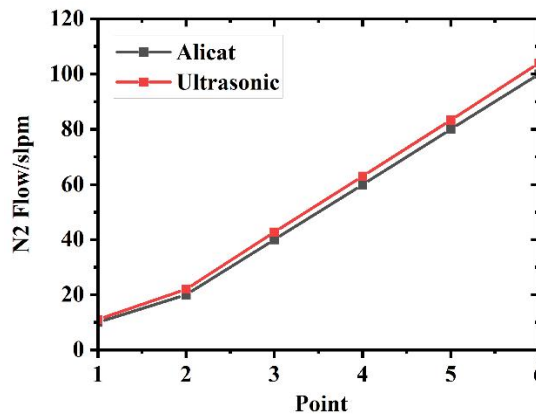


Figure 6 The Nitrogen Flow Rates Measured by Different Sensors

4 RESULTS AND DISCUSSION

4.1 Output Characteristics of the Fuel Cell

The fuel cell system used in the experiment has a rated power of 130 kW, with 418 fuel cell stacks and a single stack area of 330 cm². The experimental plan involves running each current density point stably for 5 minutes. The experimental results are shown in Figure 7. As can be seen from the figure, as the load current gradually increases, the stack output voltage decreases from 357 V to 267 V. The voltage data taken after 3 minutes of stable operation at each operating point is averaged to obtain the fuel cell's output polarization curve, as shown in Figure 8. It can be observed that as the current density increases from 0.1 A cm⁻² to 1.6 A cm⁻², the cell voltage decreases from 0.83 V to 0.64 V.

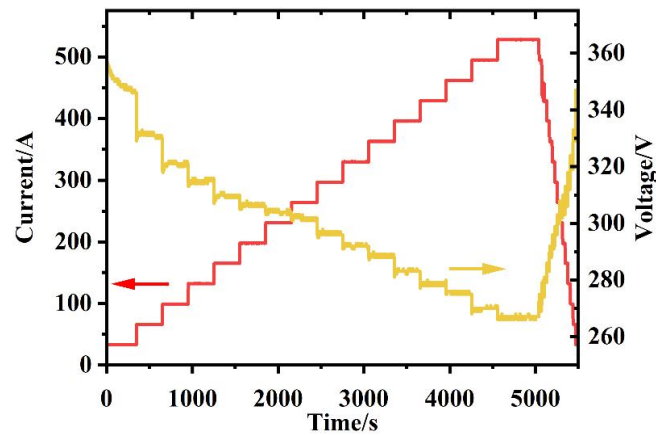


Figure 7 The Variation of the Fuel Cell Load Current and Output Voltage With Time

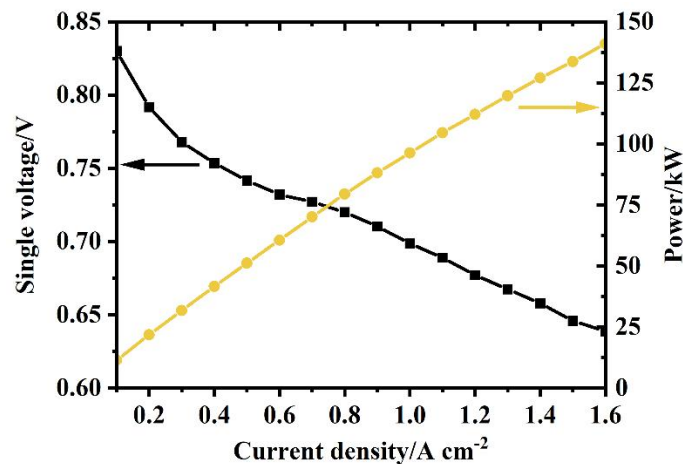


Figure 8 The Polarization Curve and Power Output of The Fuel Cell

3.2 Variation of Anode Component Concentrations

Three different current density points, 0.4, 0.8, and 1.2 A cm⁻², were selected for detailed analysis. The experimental results are shown in Figures 9, 10, and 11. It can be observed that when the drainage valve is opened, the nitrogen in the anode chamber is expelled, while the hydrogen concentration gradually increases and the nitrogen concentration decreases, displaying a sawtooth pattern. However, the anode water vapor concentration remains relatively constant at the same current density. As the current density increases, the water vapor concentration gradually increases. The hydrogen concentration in the anode remains between 70% and 75% at different current densities, and the nitrogen concentration stays around 20% to 25%. As the current density increases, the interval between drainage valve openings becomes shorter due to the increasing water production in the cell.

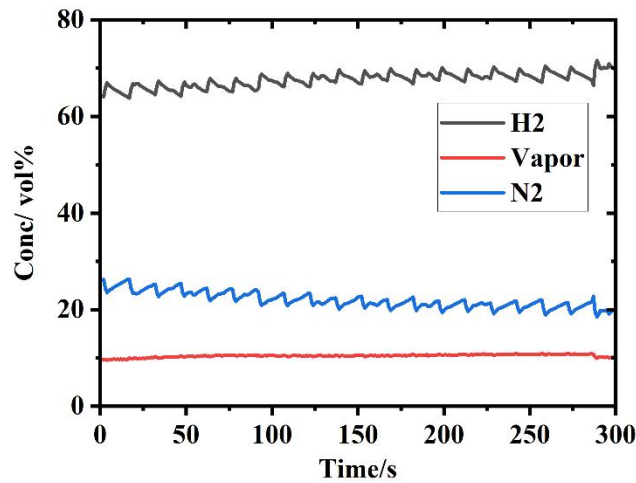


Figure 9 The Variation of Anode Gas Components at a Current Density of 0.4 A cm^{-2}

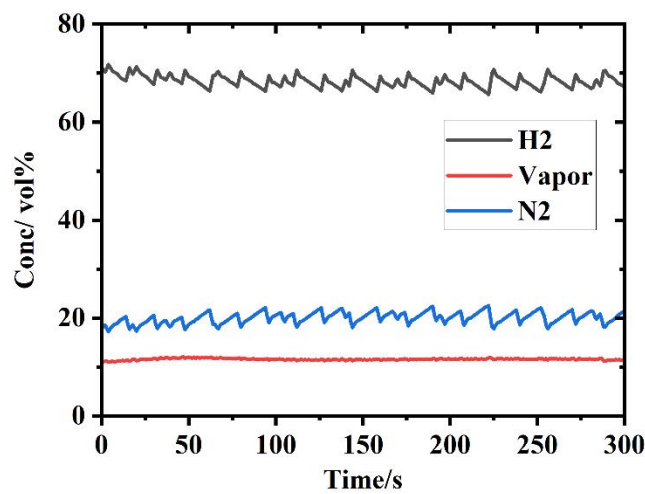


Figure 10 The Variation of Anode Gas Components at a Current Density of 0.8 A cm^{-2}

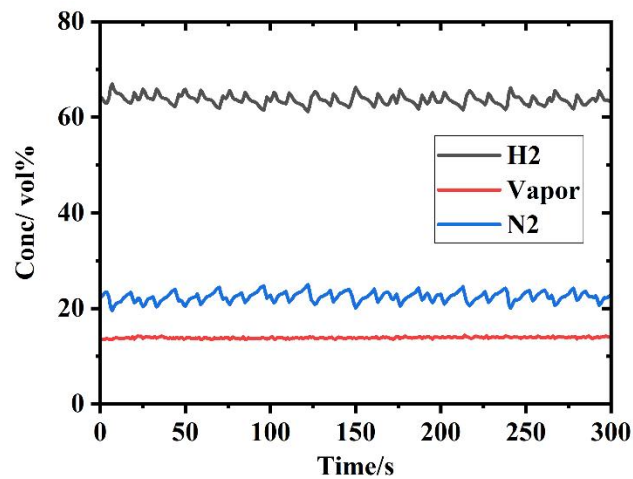


Figure 11 The Variation of Anode Gas Components at a Current Density of 1.2 A cm^{-2} .

5 CONCLUSION

Through experimental methods, the variation of components in the anode circulation loop of the fuel cell system was studied, and its impact on output performance was analyzed. The conclusions are as follows:

- (1) The ultrasonic sensor can monitor the hydrogen, nitrogen, water vapor concentration, and flow rate in the hydrogen recirculation loop online. The measurement error does not exceed 1%, which is within the acceptable error range.
- (2) In the 130 kW fuel cell system, as the load current gradually increases, the stack output voltage decreases from 357 V to 267 V. As the current density increases from 0.1 A cm^{-2} to 1.6 A cm^{-2} , the cell voltage decreases from 0.83 V to 0.64 V.

(3) As the current density increases, the water vapor concentration gradually increases. The hydrogen concentration in the anode remains between 70% and 75% at different current densities, while the nitrogen concentration remains between 20% and 25%.

COMPETING INTERESTS

The authors have no relevant financial or non-financial interests to disclose.

FUNDING

This work was supported by China National Railway Group Co., Ltd. Unveiled Its Flagship Project (grant number: N2022J016-A) and Changzhou City's "Unveiling the List and Leading the Way" Science and Technology Research Project (grant number: 2023-Z-GKB-JS-0009).

REFERENCES

- [1] Shao Zhigang, Yi Baolian. Current Status and Outlook of Hydrogen Energy and Fuel Cell Development. *Bulletin of the Chinese Academy of Sciences*, 2019, 34(4): 469-477.
- [2] Huang Jianbiao, Yang Daijun, Chang Fengrui, et al. Durability Study of Fuel Cell Stacks under Vehicle Operating Conditions with Low Hydrogen Metering Ratios. *Journal of Chemical Engineering of Chinese Universities*, 2015(6): 1364-1370.
- [3] Huang Jianbiao, Yang Daijun, Chang Fengrui, et al. Durability Study of Fuel Cell Stacks under Vehicle Operating Conditions with Low Hydrogen Metering Ratios. *Journal of Chemical Engineering of Chinese Universities*, 2015(6): 1364-1370.
- [4] Zhu Yun. Research on the Optimization and Control of Anode and Cathode Gas Supply Systems in Proton Exchange Membrane Fuel Cells. University of Electronic Science and Technology of China, 2024.
- [5] Zhang Jiaming, Ma Tiancai, Cong Ming, et al. Modeling and Control of Hydrogen Systems in High-Power Fuel Cells. *Automobile Technology*, 2021(2): 23-27.
- [6] Qianwen T, Bing L, Daijun Y, et al. Review of hydrogen crossover through the polymer electrolyte membrane. *International Journal of Hydrogen Energy*, 2021, 46(42): 22040-22061.
- [7] Mohsen Kandi Dayeni, Mehdi Soleymani. Intelligent energy management of a fuel cell vehicle based on traffic condition recognition. *Clean Technologies and Environmental Policy*, 2016, 18(6) : 1945-1960.
- [8] Kairui Dong, Guangbin Liu. A review of hydrogen recirculation systems for fuel cells. *Power Technology*, 2021, 45(04): 545-551.

EXPLORATION OF THE DETECTION METHOD OF THE CONDITION OF PATIENTS ON THE AMBULANCE STRETCHER

XinLei Yang, JueXiao Chen*

School of Automotive Engineering, Tongji University, Shanghai 200092, China.

Corresponding Author: JueXiao Chen, Email: chenjuexiao@tongji.edu.cn

Abstract: To improve the efficiency of ambulance emergency task scheduling and address the issues of low efficiency and poor real-time performance in traditional manual entry of stretcher status, this paper proposes an automatic judgment method for ambulance emergency status based on deep learning. A self-built ambulance stretcher dataset is constructed by combining 567 images captured independently from ambulances and 545 images obtained via web crawling. Data augmentation techniques are used to enhance model robustness, and mainstream object detection algorithms such as TOOD, Faster R-CNN, and YOLOv8 are compared and analyzed. Experimental results show that YOLOv8 achieves an average precision (AP@0.5) of 0.779 at an IoU threshold of 0.5, with only 11.2 million parameters, significantly outperforming other models. This method can accurately and real-time determine the stretcher status, providing a reliable basis for emergency centers to dynamically dispatch ambulance resources. It effectively shortens the emergency response time and improves the success rate of emergency rescue.

Keywords: Ambulance emergency status; Object detection; Deep learning; Data augmentation

1 INTRODUCTION

Improving the utilization rate of ambulances in service is crucial for enhancing emergency rescue success. Upon receiving a task, ambulances must reach the scene promptly to provide treatment within the critical "golden time." For instance, cardiac arrest patients require a response time of less than 10 minutes, and early defibrillation maximizes cardiopulmonary resuscitation success[1]. Studies show that the survival rate for out-of-hospital cardiac arrest exceeds 10% in Europe and the United States, while it remains at 1% in China, primarily due to differences in emergency response times. Developed countries such as Denmark and Japan achieve response times of approximately 3 minutes, whereas the United States and Russia report 4–6 minutes[2]. For emergency dispatch centers, real-time knowledge of whether a stretcher is occupied is essential for assigning subsequent tasks. Once a stretcher is detected as unoccupied after patient transfer, the ambulance becomes available for new assignments. With advancements in IoT-enabled ambulances, onboard data can now be transmitted seamlessly to emergency centers[3].

Current domestic ambulance systems primarily rely on manual input of stretcher status, which is inefficient, subjective, and increases workload for emergency personnel. Recent developments in industrial automation and electronic technologies have facilitated the adoption of status detection methods. For example, Gao Wenxuan et al. proposed leveraging idle computing resources from vehicles to alleviate edge server load[4]. Common detection methods, such as gravity sensors and infrared detection, face challenges in installation complexity, high costs, and low accuracy. In contrast, deep learning-based detection offers advantages in speed, convenience, and cost-effectiveness, making it ideal for ambulance stretcher status detection.

This study focuses on deep learning algorithms for ambulance stretcher status detection, utilizing a self-constructed dataset to achieve automatic judgment of emergency status.

2 AMBULANCE STRETCHER DATASET CONSTRUCTION

The collection and construction of a dataset is a critical step in the deep learning process, as the scientific validity and representativeness of the dataset directly determine the accuracy and reliability of the final detection results. During the training and validation phases of a deep learning model, the dataset used must align with real-world application scenarios, especially for the task of detecting ambulance stretcher images. To ensure the model can operate effectively in real environments, the constructed ambulance stretcher dataset needs to exhibit diversity. This means the dataset should include multi-angle images to capture the features of stretchers from different perspectives; it should also cover various lighting conditions to simulate the effects of different illumination environments on images; additionally, the dataset must include diverse scenarios to reflect the real-world applications of ambulances in different environments.

The ambulance stretcher dataset used in this experiment consists of two parts. The first part is real-time collection of stretcher images through cameras and digital video recorders installed on ambulances. The second part involves using web crawler programs to obtain relevant ambulance stretcher images from the Internet. Combining these two methods can construct a more comprehensive and scientific dataset, providing a solid foundation for subsequent deep learning model training.

2.1 Dataset Shooting

Cameras selected for ambulances are usually small in size, mainly spherical cameras, which save space and better adapt to the internal environment of ambulances. These cameras must also have night vision functions to ensure clear capture of surrounding images under low-light conditions. Ambulances themselves need to have video storage capabilities to record and save key monitoring video data, ensuring that relevant materials can be retrieved at any time in emergency situations.

Considering the actual shooting scenario of ambulances, the self-collected image data mainly uses Dahua brand network cameras and digital video recorders. Two camera models were selected: DH-IPC-HDBW3233F-M-AS and DH-IPC-HDW1020C. Both models have high resolution and good low-light performance, providing clear image quality in various environments. For digital video recorders, the DH-MNVR4104-GFW model was used, which supports multi-channel video input and has strong video storage capacity to meet the need for long-term video recording. Through these high-performance devices, 567 stretcher images during ambulance missions were effectively collected, providing reliable data for subsequent analysis and model training.

2.2 Dataset Crawling

Limited by equipment, vehicles, and operating environments, self-shot ambulance stretcher images are relatively single and have certain limitations in application. To obtain more extensive stretcher images from various ambulances, regions, and camera types as data sources, web crawlers were used to acquire the required images.

Web crawlers are automated tools that search for target information on the Internet through specific rules and algorithms. Driven by the continuous upgrading of Internet infrastructure, web crawler technology has evolved exponentially, forming a diversified technical ecosystem. Search engine crawlers focus on collecting and indexing web content, allowing users to quickly find needed information through search engines; image crawlers specifically target image data to obtain specific types of visual information. The design and implementation of these crawlers are based on user requirements. Developers customize programs according to specific user needs to ensure that crawlers can efficiently and accurately acquire the required data. Due to the urgent demand for dataset acquisition, web crawling technology has been widely adopted. Some developers have customized crawler tools into applications such as WebHarvy, Larbin, and Web Scraper. These tools possess distinct functionalities and features, enabling users to perform data scraping in diverse scenarios. However, such fixed-format crawler tools often fail to directly meet the needs of specific research projects, particularly when handling complex crawling targets. This may result in the inclusion of non-target image categories in the scraped results, thereby compromising data quality and reliability.

To address these needs, a flexible crawler architecture was independently developed using Python 3.8 and its request module. The request module is a library for sending HTTP requests, with a relatively simple API and good stability. This approach enables more flexible design of crawler programs to adapt to different needs and complex crawling targets. Through web crawlers, 545 ambulance stretcher images were successfully captured from major search engines such as Baidu and Google.

2.3 Data Augmentation

To improve the final model's performance, stability, and adaptability to new data, data augmentation technology was used to expand the original training set. The Augly framework was selected as the implementation tool, which is a data augmentation library focused on adversarial robustness, providing a wide range of augmentations for multiple modalities (audio, image, text, and video) [5].

The Augly framework was developed by the AI team at Facebook (now Meta). This framework enhances model generalization by generating extensive variant data, enabling models to learn broader patterns. During data augmentation, Augly employs a diverse range of transformation strategies, including image blurring, random noise addition, grayscale conversion, random rotation, and random adjustments to brightness and contrast. These transformations are applied stochastically during training, producing a wide array of images from varying angles and scales, thereby better simulating real-world image diversity.

For instance, in ambulances, cameras installed on the ceiling of the medical compartment are not fixed in position—they may be mounted at any of the four corners. After installation, workers typically adjust the camera angles to capture as much of the compartment's occupants and equipment as possible. Consequently, the positioning and angles of footage vary across different ambulances.

Ambulance electrical systems are designed with complexity to accommodate diverse power configurations for emergency scenarios. Typically, these systems include a 12V primary vehicle power supply, which serves as the foundational energy source for onboard devices. Additionally, ambulances are equipped with a 24V converted power supply to support high-power equipment, ensuring stable operation during emergencies. A 220V inverter power supply is also integrated to convert direct current (DC) to alternating current (AC), powering critical medical devices and lighting systems. These intertwined multi-power systems inevitably introduce interference to camera footage, leading to variations in image quality. The Augly framework can perform operations such as random rotation and noise addition on ambulance stretcher images to simulate the diversity of images captured by real cameras in complex working environments. These augmentation techniques help researchers better understand and address challenges in real-world model applications, effectively improving the model's performance under various conditions. This makes Augly an

indispensable tool in the fields of machine learning and computer vision, assisting researchers in achieving better results in data processing and model training. The effect of data augmentation is shown in Figure 1.



Figure 1 Data Augmentation Examples

3 EXPERIMENTAL COMPARISON AND ANALYSIS

3.1 Experimental Environment and Parameter Configuration

The hardware and software configurations for all model training and testing in this paper are shown in Table 1, using the self-made dataset described in this chapter. CUDA 12.1 was used for computational acceleration to improve efficiency.

Table 1 Experimental Environment

Parameter	Value
CPU Model	Intel(R) Xeon(R) CPU E5-2680
GPU Model	Nvidia GeForce RTX 2060
Memory	24G
Video Memory	6G
Operating System	Windows 10 Enterprise
Programming Language	Python 3.9
Deep Learning Framework	PyTorch 1.13.1

For the self-made ambulance stretcher dataset, the mmDetection framework was selected as the tool for model performance comparison during multi-model contrast experiments. This framework supports various advanced object detection algorithms, including two-stage and one-stage methods such as TOOD [6], Faster R-CNN [7], and YOLO [8], which are representative in the field of object detection and have good comprehensive detection performance for comparative analysis.

The experimental CPU is Intel(R) Xeon(R) CPU E5-2680, equipped with a GeForce RTX 2060 graphics card with 6G video memory, using CUDA 12.1 for acceleration and Python 3.9 as the programming language. The Stochastic Gradient Descent (SGD) algorithm was used for training with the following parameters: 400 epochs, input image size of 640×640, batch size of 8, initial learning rate of 0.01, and optimizer momentum of 0.937.

3.2 Experimental Result Analysis

In this experiment, each object detection algorithm was rigorously tested to ensure the best-performing version during training. This process is crucial because the effectiveness of the algorithm largely depends on the performance of the selected model. To accurately evaluate the performance of multiple object detection algorithms, the COCO metric system widely recognized in the field of object detection was adopted for evaluation. This evaluation criterion demonstrates good universality and scientific rigor, ensuring the objectivity of the assessment results. Performance is primarily measured using different metrics, including the average precision (AP) across intersection-over-union (IoU) thresholds from 0.5 to 0.95 (AP_{0.5:0.95}) and the average precision at an IoU threshold of 0.5 (mAP_{0.5}). Additionally, the number of parameters in each model must be considered, as it reflects the model's complexity and directly impacts the algorithm's computational efficiency and resource consumption in practical applications—an aspect particularly critical for mobile devices or real-time monitoring systems. Among the compared algorithms, Cascade R-CNN [9] and Mask R-CNN [10] typically achieve higher recognition accuracy, while YOLOv3 [11] and YOLOv8 [12] are more

suitable for real-time applications. Emerging algorithms such as TOOD, GFL [13], and ATSS [14] show good performance in specific scenarios. Each algorithm was trained on the self-made dataset until convergence, and the test results are shown in Table 2. Figure 2 visually displays the accuracy comparison during training.

Table 2 Comparison of Experimental Results for Each Algorithm

Model	AP@0.5	AP@0.5:0.95	Parameters
TOOD	0.747	0.476	32.018M
GFL	0.754	0.477	32.258M
ATSS	0.758	0.491	32.113M
Faster R-CNN	0.774	0.463	41.753M
Cascade R-CNN	0.759	0.499	69.152M
Mask R-CNN	0.754	0.493	43.971M
YOLOv3	0.712	0.464	19.524M
YOLOv8	0.779	0.486	11.2M

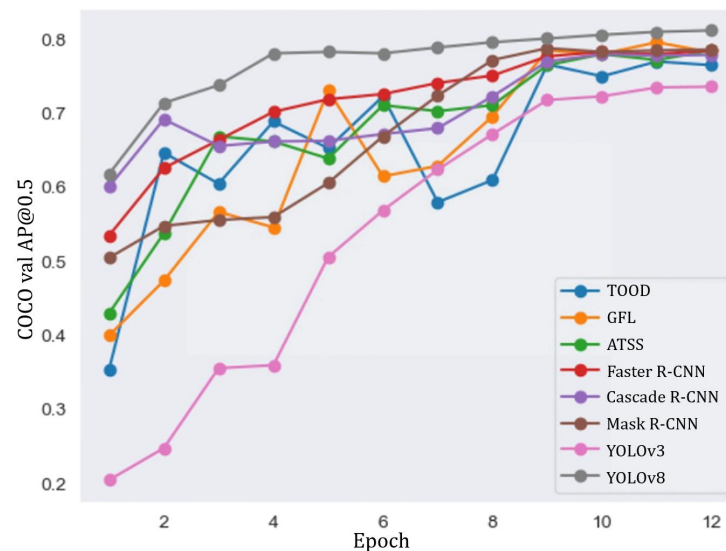


Figure 2 Precision Comparison during Training

Analyzing AP@0.5 (IoU threshold of 0.5), YOLOv8 performs best with an AP@0.5 of 0.779, followed by Faster R-CNN (0.774) and ATSS (0.758). This indicates that Faster R-CNN and YOLOv8 have higher detection accuracy under lower IoU requirements. In terms of parameter quantity, Cascade R-CNN has the most parameters (69.152M), consistent with its complex network structure and multi-stage detection process. In contrast, YOLOv8 has the fewest parameters (11.2M), demonstrating its ability to maintain high performance while significantly reducing model complexity. For AP@0.5:0.95 (averaged over IoU thresholds from 0.5 to 0.95), Cascade R-CNN performs best at 0.499, followed by Mask R-CNN (0.493) and ATSS (0.491), indicating good generalization ability in handling object detection tasks with different IoU thresholds.

Cascade R-CNN is optimal for high-precision scenarios requiring strict IoU thresholds, while YOLOv8 balances high performance with low model complexity, making it more suitable for real-time detection tasks. Therefore, YOLOv8 was selected as the final algorithm for ambulance emergency status judgment.

4 CONCLUSION

This paper addresses the need for ambulance stretcher status detection by constructing a multi-scenario dataset and implementing an automatic emergency status judgment method based on deep learning. Experiments show that YOLOv8 achieves a good balance between accuracy and efficiency, suitable for real-time detection scenarios, providing an efficient technical support for emergency task dispatch. This method significantly reduces manual intervention, improves the utilization of emergency resources, and has important practical significance for optimizing emergency processes. Future research will further enhance the model's robustness in complex lighting and occlusion scenarios and explore lightweight deployment solutions to adapt to more IoT ambulance devices.

COMPETING INTERESTS

The authors have no relevant financial or non-financial interests to disclose.

REFERENCES

- [1] Hu Jingchun, Liu Xiaomei, Yang Cheng, et al. Influence of Differences in Pre-hospital Emergency Cardiopulmonary Resuscitation Conditions on the Efficacy of Patients with Cardiac Arrest. *Journal of Anhui Health Vocational & Technical College*, 2013, 12(01): 27-28.
- [2] Zhang Wenwu, Dou Qingli, Liang Jinfeng, et al. Government-led Public First Aid Training: The Practice in Bao'an, Shenzhen. *Chinese Journal of Emergency Medicine*, 2019(01): 126-128.
- [3] S M, T R, N V, et al. Adaptive ambulance monitoring system using IOT. *Measurement: Sensors*, 2022, 24.
- [4] Gao Wenxuan, Yang Xinjie. A Computation Offloading Scheme for Energy Consumption Optimization in Internet of Vehicles. *Telecommunications Science*, 2023, 39(10): 29-40.
- [5] Papakipos Z, Bitton J. Augly: Data augmentations for robustness. *arxiv preprint arxiv:2201.06494*, 2022.
- [6] Feng C, Zhong Y, Gao Y, et al. Tood: Task-aligned one-stage object detection. *2021 IEEE/CVF International Conference on Computer Vision (ICCV)*. IEEE Computer Society, 2021: 3490-3499.
- [7] Ren S. Faster r-cnn: Towards real-time object detection with region proposal networks. *arxiv preprint arxiv:1506.01497*, 2015.
- [8] Redmon J. You only look once: Unified, real-time object detection. *Proceedings of the IEEE conference on computer vision and pattern recognition*. 2016.
- [9] Cai Z, Vasconcelos N. Cascade r-cnn: Delving into high quality object detection. *Proceedings of the IEEE conference on computer vision and pattern recognition*. 2018: 6154-6162.
- [10] He K, Gkioxari G, Dollár P, et al. Mask r-cnn. *Proceedings of the IEEE international conference on computer vision*. 2017: 2961-2969.
- [11] Redmon J. Yolov3: An incremental improvement. *arxiv preprint arxiv:1804.02767*, 2018.
- [12] Terven J, Córdova-Esparza D M, Romero-González J A. A comprehensive review of yolo architectures in computer vision: From yolov1 to yolov8 and yolo-nas. *Machine Learning and Knowledge Extraction*, 2023, 5(4): 1680-1716.
- [13] Li X, Wang W, Wu L, et al. Generalized focal loss: Learning qualified and distributed bounding boxes for dense object detection. *Advances in Neural Information Processing Systems*, 2020, 33: 21002-21012.
- [14] Zhang S, Chi C, Yao Y, et al. Bridging the gap between anchor-based and anchor-free detection via adaptive training sample selection. *Proceedings of the IEEE/CVF conference on computer vision and pattern recognition*. 2020: 9759-9768.

FUNCTIONAL ENHANCEMENT OF ENZYMATICALLY HYDROLYZED DOUBLE CROSSLINKED HOT MELT STARCH

Hao Wang, ChuanWei Zhang*

College of Mechanical and Electrical Engineering, Qingdao University, Qingdao 266071, Shandong, China.

Corresponding Author: ChuanWei Zhang, Email: zhangchuanwei3722@163.com

Abstract: In order to enhance the comprehensive performance of hot melt starch (TPS), in this study, a structurally stable TPS composite with excellent mechanical properties was prepared by using enzymatic-crosslinking composite as the core of modification, combined with organo-montmorillonite (OMMT) hybridisation strategy. The molecular weight of starch was reduced by α -amylase pretreatment to improve its fluidity; subsequently, citric acid and sodium trimetaphosphate were used for synergistic cross-linking to construct a dense three-dimensional molecular network structure, which enhanced the thermal stability and water resistance of the material. On this basis, different mass fractions of OMMT were introduced to further improve the mechanical strength and flexibility of the composite system through interfacial modulation. The results show that the appropriate amount of OMMT can effectively improve the tensile strength and elongation at break of the materials, and the performance is optimal when the amount of OMMT added is 1.5 g. The results show that the OMMT can be used in the composite system to improve the mechanical strength and flexibility of the materials. Excessive fillers, on the contrary, caused aggregation and weakened the enhancement effect. This study provides a new idea for the functionalized design of degradable starch materials, which is of positive significance to promote the practical application of TPS in packaging and biomedical fields.

Keywords: Hot melt starch; Enzymatic cross-linking; Montmorillonite hybridisation; Device design

1 INTRODUCTION

As human society's demand for environmentally friendly materials continues to rise, the ecological risks posed by traditional petroleum-based plastics, which are difficult to degrade, are a source of growing concern[1]. These synthetic materials are extremely stable in the natural environment, causing large amounts of 'white pollution' to remain in soil and water over time, posing a potential threat to ecosystems and human health[2]. In addition, the environmental costs of these materials are exacerbated by the non-renewable nature of petrochemical resources and the high carbon emissions generated during processing[3]. For this reason, the search for a sustainable alternative material that is both degradable and adaptable to the demands of modern industrial processing has become a key focus of current materials science research[4].

Starch, as a natural polysaccharide, is regarded as one of the most promising bio-based biodegradable polymers because it is not only widely available and inexpensive, but also can be rapidly decomposed into harmless substances under the action of microorganisms and enzymes[5]. However, the application of natural starch also faces a series of challenges, mainly in terms of its poor thermoplasticity[6], weak mechanical properties, and susceptibility to hygroscopicity, making it difficult to directly replace traditional plastics[7]. In actual processing, the melting temperature of starch is usually close to or exceeds its decomposition temperature[8], making it difficult to achieve industrial production by thermal processing[9]. Therefore, modification research around starch for structural adjustment and property optimisation has gradually become a key topic.

To address the thermal processing obstacles of natural starch, the concept of 'Thermoplastic Starch' (TPS) has been proposed in the academic community[10], which means that starch can exhibit processing characteristics similar to those of thermoplastic polymers[11] through the introduction of plasticisers and appropriate modification strategies[12]. Early thermoplastic modifications were mainly made by adding small molecules such as glycerol, urea, sorbitol, etc., to break the hydrogen bonds between the starch chains, thus imparting a certain degree of flexibility and processability to the material[13]. However, although plasticising modification improves the processing fluidity[14], it has limited enhancement on the mechanical strength and environmental stability of the material[15], especially under humid or high temperature conditions, and its mechanical properties still fluctuate greatly[16].

On this basis, researchers began to synergistically design the enzymatic degradation of starch with chemical cross-linking[17]. By controlling the degree of enzymatic degradation, the molecular weight and crystallinity of starch molecules can be effectively reduced[18], and the inter-chain entanglement can be reduced, thus enhancing its fluidity and lowering the melting threshold. Cross-linking modification, on the other hand, can build a stable three-dimensional network structure between the molecules, enhancing their mechanical support and thermal stability[19]. The combination of the two is expected to realise the goal of a material that is 'soft but strong', i.e., having good ductility and a certain degree of structural strength at the same time[20].

Among many enzymes, α -amylase is widely used in starch modification due to its high selectivity and mild reaction conditions[21]. Its mechanism of action is mainly to hydrolyse the α -1,4 glycosidic bond within the starch molecule[22], rapidly reducing the molecular chain length and providing more efficient reaction sites for the subsequent chemical modification reaction. In the cross-linking strategy, citric acid and sodium trimetaphosphate showed a good synergistic

effect in constructing the cross-linking network due to their high reactivity and environmental friendliness[23]. The former formed cross-links between starch chains through esterification to enhance its mechanical stability[24], while the latter further enhanced the consistency and density of the network structure through phosphoric acid esterification[25], which significantly improved the thermal stability and hydrolysis resistance of the material[26].

Although preliminary progress has been made in the enzymatic digestion and cross-linking of hot melt starch, there are still limitations in the single organic phase modification system[27]. For example, the modified TPS still suffers from water absorption and softening under high humidity environment[28], and there is still room for improvement of mechanical properties[29]. For this reason, the introduction of nano-organic fillers to form hybrid structures with starch has become a new research trend in recent years[30]. Layered inorganic materials, such as montmorillonite (MMT), have high specific surface area and excellent barrier properties[31], which can form a stable interface with starch through hydrogen bonding and electrostatic adsorption, significantly improving the rigidity and water resistance of the material[32]. In particular, organically modified montmorillonite (MMT-P) can further improve the compatibility with the organic matrix[33], enabling the composites to achieve good ductility and processing stability while maintaining high strength.

In addition, the nanohybrid fillers can also inhibit the thermal degradation behaviour of starch materials in thermal processing on a microscopic scale, improve their rheological stability, and expand their applications in high-temperature processes such as injection moulding and extrusion[34]. In recent years, TPS composites by constructing inorganic-organic hybrid interfacial structures have shown promising prospects in food packaging, disposables, and biomedical materials[35].

Based on the above background, this study proposes a novel TPS material preparation pathway based on enzymatic and cross-linking synergistic modification combined with inorganic montmorillonite hybridisation enhancement, aiming to comprehensively improve the thermoplastic processability, mechanical properties and environmental stability of starch-based materials. The research work will focus on the following aspects: (1) to explore the influence of the degree of enzyme digestion on the structure and plasticity of starch; (2) to analyse the regulation mechanism of different cross-linking agents on the network structure and physical properties of the materials; (3) to investigate the effect of OMMT on the microstructure, mechanical strength and moisture resistance of the composites with different additions; (4) to ultimately realise a functionalised hot-melt starch composite material with excellent comprehensive performance, and to provide a new pathway for the preparation of TPS materials. starch composites with excellent comprehensive performance, providing theoretical support and experimental basis for its industrial application in the field of green materials.

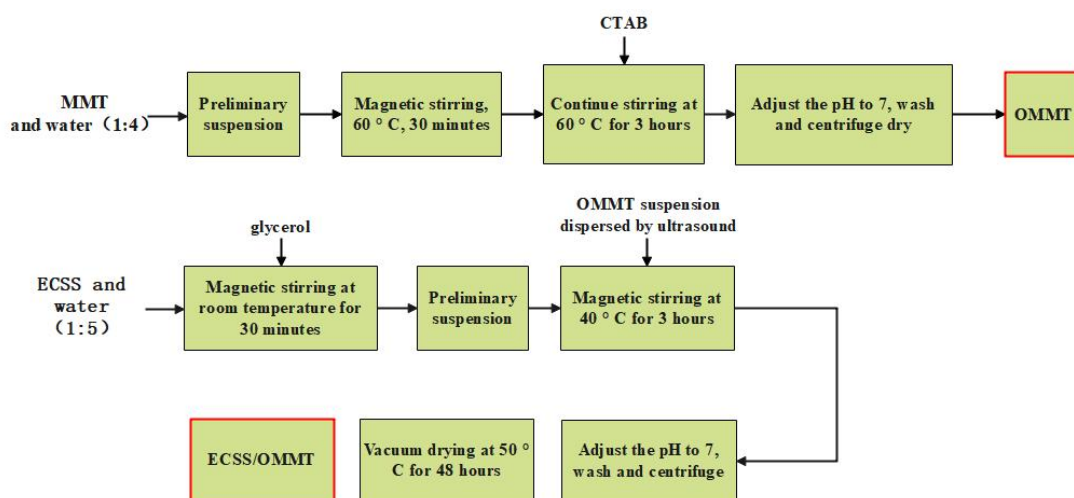


Figure 1 Modification of Organic Montmorillonite (OMMT) and Hybrid Process of ECSS and OMMT

2 MATERIALS AND METHODS

2.1 Experimental Material

The starches used in this experiment were common corn starch, medium temperature α -amylase (2 U/mg), hydrochloric acid, sodium hydroxide, urea, citric acid, sodium trimetaphosphate, montmorillonite, cetyltrimethylammonium bromide (CTAB), and ethanol (C₂H₆O) were purchased from the Macklin Company (Shanghai, China), and glycerol was purchased from the Shanghai Hutai Test.

2.2 Experimental Methods

2.2.1 Enzymatic double cross-linked starch preparation

Enzymatic starch preparation process: natural corn starch (20 g) and distilled water (80 g) were added to a round-bottomed beaker, and the material containing the experimental reaction was placed in a water bath with the temperature of the water bath set to 80°C, and the fully pasted starch was prepared by rapid stirring for 30 min under this environment. Next, 0.05 g of medium-temperature α -amylase was weighed into a beaker containing 10 ml of distilled water and stirred well to make an enzyme solution, which was added to the pasted starch, and then stirred rapidly at 80°C for five minutes to allow the pasted starch to begin to produce the obvious phenomena of liquefaction and thinning. Ice water was prepared in advance, and the liquefied starch solution was placed in the ice water for rapid cooling to stop the continued reaction of the amylase enzyme. After cooling to room temperature, the starch solution was adjusted to a pH <3 using a hydrochloric acid titration solution (1 mol/L), followed by continued manual stirring for 10 min. At the end of stirring, the beaker was placed in a water bath heated to 100°C for 5 min for enzyme inactivation, and after the heating was completed the flask continued to be transferred to ice water to vacate, and after the solution was brought down to room temperature, PH adjustment was carried out. The pH of the slurry was adjusted using sodium hydroxide solution (1mol/L), and the appropriate amount was dropped to react with the remaining hydrochloric acid in the solution, thus completing the inactivation of the enzyme. The reacted starch solution was poured into a polytetrafluoroethylene petri dish and put into a vacuum oven with the temperature set at 70°C for 24 h. The successfully modified enzymatic starch ES was obtained after the drying was completed.

Preparation of sodium citrate tri-metaphosphate double crosslinked starch (ECSS): firstly, 30 g of enzymatically dissolved starch (ES) was mixed with 100 mL of distilled water and stirred to form a homogeneous starch solution. Subsequently, glycerol (2 g) and urea (1 g) were added as plasticisers, and the pH was adjusted to 5.5 to provide suitable conditions for the esterification and cross-linking of citric acid. After adding 9 g of citric acid, the mixture was stirred and mixed well at room temperature, and then placed in a water bath at 70°C for 2 hours to promote the esterification of citric acid with the hydroxyl groups on the molecular chain of starch.

After the first step, the slurry was cooled to room temperature. Subsequently, the pH was adjusted to 10 with 1 mol/L sodium hydroxide solution to create a suitable environment for phosphate esterification with sodium trimetaphosphate. 9 g of sodium trimetaphosphate was added and placed in a water bath at 35°C for 2 h to achieve the second step of cross-linking, i.e., the phosphate bonding between sodium trimetaphosphate and the hydroxyl groups of starch.

After the reaction was completed, the sample was washed three times with a 1:1 mixture of distilled water and ethanol to remove unreacted cross-linkers and by-products. Subsequently, the pH of the system was adjusted to neutral using 1 mol/L hydrochloric acid solution. Finally, the treated slurry was poured into a polytetrafluoroethylene petri dish and vacuum dried at 40°C for 24 h to obtain the enzymatically cleaved citric acid/sodium trimetaphosphate double crosslinked modified starch samples (ECSS).

2.2.2 Preparation of organic montmorillonite (OMMT)

First, a preliminary suspension was prepared by adding 20 g of natural montmorillonite (MMT) to 100 mL of deionised water. The mixed system was stirred in a magnetic stirrer at a constant temperature of 60 °C for 30 min to promote uniform dispersion of the montmorillonite. Subsequently, an appropriate amount of cetyltrimethylammonium bromide (CTAB) was added to the system as an organic intercalating agent, and the reaction was continued for 3 h to insert organic cations into the interlayer structure of montmorillonite to achieve organic modification. After the reaction was completed, the pH of the system was adjusted to neutral and the products were washed several times using a mixture of ethanol and distilled water to remove unreacted impurities and surface adsorbates. Afterwards, the washed sample was centrifuged, and the supernatant was taken, poured into a polytetrafluoroethylene Petri dish, and dried in a vacuum oven at 60 °C for 24 h. The final organic modified montmorillonite (OMMT) powder was obtained in the form of flakes.

2.2.3 Preparation of thermoplastic starch/montmorillonite composites

Twenty g of dried double crosslinked enzymatically cleaved thermoplastic starch (ECSS) was mixed with 100 mL of distilled water, 2 g of glycerol was added as a plasticiser and the slurry was stirred in a magnetic stirrer for 30 min at room temperature to make the slurry well homogenised. Different masses of OMMT (0.5 g, 1.5 g, 3.5 g, and 5 g, respectively) were taken and mixed with a small amount of distilled water, and dispersed by ultrasonic dispersion using an ultrasonic processor (200 W, 10 min), with the aim of facilitating the exfoliation of the montmorillonite flake layer and improving the stability of its dispersion in the starch matrix. The ultrasonicated OMMT solution was slowly added to the ECSS slurry and stirring was continued for 3 h at 40 °C to promote the interaction and physical hybridisation between montmorillonite and starch molecules. The slurry obtained after the reaction was cleaned and transferred to a Teflon mould, and dried in a vacuum oven at 50 °C for 48 hours to obtain ECSS/OMMT composite samples with different OMMT contents. The samples were named MMT-1 (0.5 g), MMT-2 (1.5 g), MMT-3 (3.5 g) and MMT-4 (4.5 g) according to the amount of OMMT added.

2.2.4 Preparation of thin films

The dried ECSS/OMMT composite powder was placed into a mould lined with PTFE film on the top and bottom of the mould, and transferred to a hot pressing unit for moulding. The hot pressing conditions were set at a temperature of 50 °C and a pressure of 0.5 MPa, with a continuous pressure of 5 minutes, a holding pressure of 3 minutes, and a natural cold pressing of 20 minutes, after which the mould was removed to obtain a structurally intact hot-pressing moulded starch film.

2.3 Micro-Morphological Characterisation of Modified Starch

he prepared films were subjected to optical observation in a bright environment to observe the appearance and morphology of the films as well as the light transmittance and transparency of the films.

The film samples were subjected to gold sputtering and the internal structure of different hot-pressed starch films was observed using a scanning electron microscope (JEOL-JSM6400, Tokyo, Japan).

2.4 Fourier Transform Infrared Spectroscopy (FTIR)

The effect of modification on the chemical structure of starch films was analysed by Fourier Transform Infrared Spectroscopy analysis (FTIR; Nicolay iS20, Thermo Fisher Scientific, USA), where the film samples were analysed by FTIR using FTIR, with FTIR spectra of each sample taken in the range of 400 to 4000 cm^{-1} .

2.5 Thermogravimetric Analysis (TGA)

The thermal stability of the films was studied using a TAsDT650 simultaneous thermal analyser. The weight of the samples was about 5 mg and the heating temperature was set from room temperature to 450°C with the heating rate set at 10°C/min.

2.6 Mechanical Property Analysis

A universal mechanical testing machine (Instron 3367, Illinois Tool Works, Inc.) was used. The films obtained by hot pressing were cut with a sample length of 35 mm thickness of 1 mm and the tensile strength and elongation at break of the samples were measured. Five sets of tests were performed for each sample at room temperature and the average of the tests was taken.

2.7 Water Vapour Transmission (WVT)

WVT was measured using a modified version of the method ASTM E - 96-95. The sample films were cut and sliced into circles of 65 mm diameter and placed on a table at 50% humidity to obtain a constant weight. The experimental temperature was $23 \pm 2^\circ\text{C}$ with 50% humidity. And the weight of the disc assembly was taken every half an hour to obtain the weight reduction. The water vapour transmission rate was calculated by the following equation:

$$\text{WVT} = \frac{\Delta_m}{\Delta_t * S} \quad (1)$$

Δ_m is the amount of water subtracted, Δ_t is the experimental time, S is the film area.

2.8 Water Contact Angle Test

The film was placed horizontally on the experimental platform, 50 μL of distilled water was added each time, and the water contact angle was recorded by the software after the value was stabilised. Each sample was tested 5 times and the final contact angle was calculated as the average of the 5 measurements.

3 RESULTS AND DISCUSSION

3.1 Microstructure

The figure 1 shows the surface morphology evolution process of enzymatically crosslinked hot melt starch composite materials under different OMMT addition amounts. From Figure A, it can be seen that the ECSS sample without OMMT doping has a relatively flat film surface, but there are still a certain number of bubbles and small particles, resulting in poor film uniformity and insufficient surface density. Figure b shows the sample (MMT-2) with 1.5g of OMMT added, which has the most dense and smooth surface, significantly reduced wrinkled structure, significantly reduced number of bubbles, and no obvious agglomeration phenomenon. This indicates that OMMT has the best dispersion effect in the matrix and stable composite interface structure, making it the sample with the best surface quality among all groups. In Figure c, the amount of OMMT added was further increased to 3.5g. Although it still maintained a certain degree of uniformity, granular micro area distribution could be observed, indicating that the filler began to show local aggregation. As shown in Figure d, the OMMT increased to 5g, and the membrane surface became significantly rough, with a large number of agglomerates and protrusions. Surface defects increased significantly, and the hybridization degree became imbalanced, resulting in overall structural disorder of the membrane material. From this, it can be seen that an appropriate amount of OMMT (such as 1.5g) can significantly optimize the surface morphology of starch basement membrane, while excessive OMMT will destroy its structural uniformity and reduce material quality. The 1.5g OMMT group shown in Figure b is the composite sample with the best film-forming and surface density in this study.

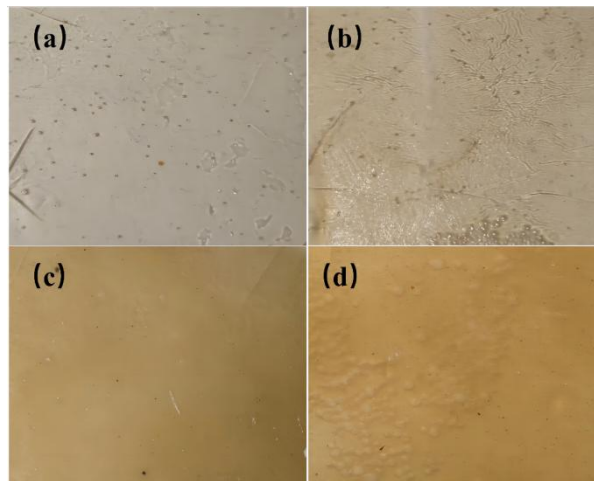


Figure 2 Comparison of Starch Hybrid Samples with Different Content of MMT:(a) MMT-1, (b) MMT-2, (c) MMT-3, (d) MMT-4

The scanning electron microscope (SEM) 200x images shown in Figure 2 visualise the effect of different content of organo montmorillonite (OMMT) doping on the cross-sectional microscopy of starch-based composites. The cross-sectional morphology of the films at different doping ratios showed significant differences, reflecting the important role of OMMT involved in the hybridisation process to regulate the densification and homogeneity of the materials.

In the MMT-1 sample corresponding to Figure (a), although some of the montmorillonite flakes have achieved initial dispersion in the matrix, the overall interface is still agglomerated, and more holes and irregular structures appear locally, indicating that the OMMT has not yet effectively established a continuous reinforcement network and the structure of the composite system is relatively loose under the low content condition. In contrast, the MMT-3 and MMT-4 samples shown in Figure (c) and (d) showed the problems of lamellar stacking and excessive overlapping, although the addition amount of OMMT was increased. The excessive stacking between the lamellae resulted in the internal structure of the material becoming inhomogeneous, accompanied by obvious cracks and particle aggregation, and the overall densification was instead damaged, which may weaken the mechanical and barrier properties of the material. Most notably, the MMT-2 sample shown in Figure (b) has a flat and homogeneous cross-sectional structure, with no obvious cracks or pores, and the film layer exhibits excellent continuity and densification. This morphology indicates that the appropriate amount of OMMT not only achieves good compatibility with the starch matrix, but also may form a stable synergistic structure with the starch chain segments at the molecular level, which effectively enhances the overall organisation and intermolecular forces of the material. At this time, the dispersion state of the lamellae is the most ideal, and the composite network can be fully formed, which provides a reliable basis for the mechanical enhancement and the improvement of barrier properties.

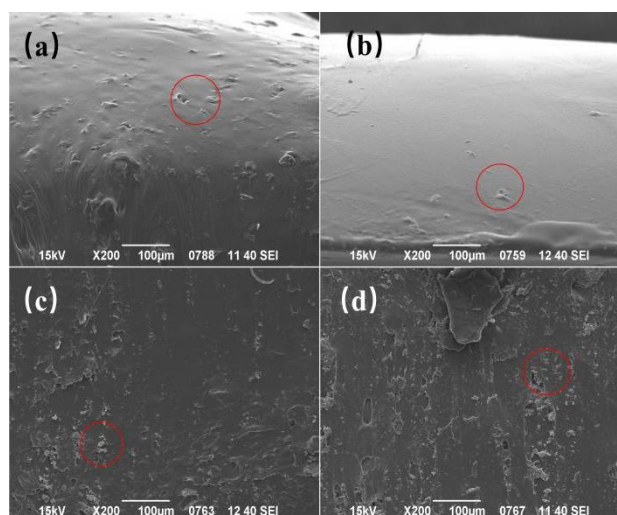


Figure 2 200x Electron Microscopy Structural Images of Different Samples: (a) MMT-1,(b) MMT-2, (c) MMT-3, (d) MMT-4

From the 1000× scanning electron microscope (SEM) images shown in Fig 3, different contents of organo-montmorillonite (OMMT) doping has an important influence on the microstructural distribution and hot-melt processing behaviour of composite thin film materials, which can indirectly reflect the material's fluidity, densification and structural stability during the hot-melt process.

Figure (a) (MMT-1) sample at low content of OMMT, the cross-section of the film layer can be seen obvious pores and irregular structure, the lamellae are not sufficiently peeled off, and some areas still exist agglomerates. This phenomenon suggests that during hot pressing, the material in the molten state has insufficient fluidity and fails to form a homogeneous and dense structure, resulting in insufficient spreading of the lamellae during thermoplastic processing and affecting the quality of the film formation.

Figure (c) and Figure (d) (MMT-3 and MMT-4) samples show the state of lamellar aggregation and dense microcracks, especially in Fig. (d) there are obvious lamellar stacking and cracks, which reflects that the uneven dispersion of OMMT in the high additive amount leads to the local structure of the 'bridge' effect, which limits the mobility of chain segments and the intermolecular structure of the material in the process of hot-melt. This reflects that the uneven dispersion of OMMT in high additive amount leads to the 'bridging' effect in the local structure, which limits the mobility of chain segments and intermolecular coordination ability of the material in the hot-melt process, and the phenomenon of 'melt fault' or internal cavity may appear in the hot-melt processing, which reduces the consistency of the overall film and processability.

In contrast, the cross-section of the sample in Figure (b) (MMT-2) is the flattest and densest, with almost no obvious holes and lamellar accumulation, showing good structural homogeneity and continuity. This structural morphology fully demonstrates that, under the appropriate doping ratio of OMMT, the material has good fluidity and dispersion properties during the hot-melt process, and a 'synergistic' micro-network may have been formed between OMMT and the starch matrix, which enables the starch chain segments to achieve a uniform orientation and distribution under the heated melt state, resulting in dense and continuous film structures. This feature also directly corresponds to the hot melt structure. This feature also directly corresponds to the improvement of the mechanical properties and film-forming quality of the samples obtained after hot-melt processing.

In summary, the 1000× SEM images not only reveal the microstructure regulation by the change of OMMT content, but also indirectly reflect the molecular movement and building ability of the material during hot-melt processing. Among them, the MMT-2 hybrid samples showed the optimal molecular structure arrangement and interfacial bonding state, which is an important doping ratio for the optimisation of hot-melt processing performance, and provides structural guarantee for the subsequent moulding process and the enhancement of application performance.

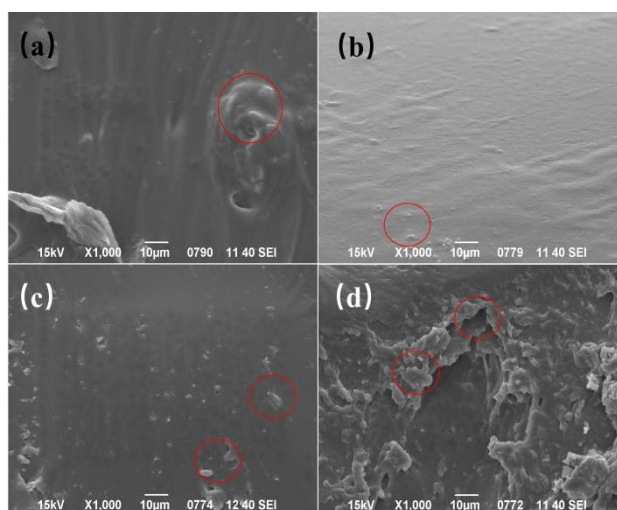


Figure 3 Microstructures of Different Samples by 1000x Electron Microscopy: (a) MMT-1, (b) MMT-2, (c) MMT-3, (d) MMT-4

3.2 FTIR

Figure 4 demonstrates the effect of different levels of montmorillonite (MMT) doping on the infrared spectra of enzymatically crosslinked starch (ECSS) materials, thus reflecting the changes in chemical structure during the hybridisation process. The comparison shows that the absorption peaks of the samples in specific wavelength bands changed significantly with the gradual increase of montmorillonite doping, indicating that the hybridisation process changed the interactions between the molecular chains of the starch molecules and the environment of the functional groups to a certain extent.

In the region of 3200-3600 cm^{-1} , all the samples showed strong broad peaks, which are the characteristic peaks of -OH stretching vibration, representing the presence of hydroxyl groups in starch. With the increase of MMT content, this absorption peak gradually showed a weak red shift and a slight decrease in peak intensity, indicating that some of the hydroxyl groups were involved in hydrogen bonding with the hydroxyl groups on the surface of the montmorillonite or the organic intercalating agent, which led to the reconfiguration of the original hydrogen bonding network between the molecules, thus enhancing the interfacial bonding between the substrate and the inorganic lamellae. In addition, multiple absorption peaks (e.g., C-O-C and Si-O correlation stretching vibrations) in the region of 1000-1200 cm^{-1} also undergo enhancement and splitting phenomena with the change of MMT doping amount, especially at 3.5g and 5g

MMT samples. This change may be related to the Si-O-Si structure of the MMT interlayers and the formation of novel interactions between them and the ether bonds in the starch, which further confirms that the introduction of the inorganic phase achieves effective hybridisation at the molecular level. The peaks around 900 cm^{-1} also show enhancement, suggesting that Si-O-Al or Si-O-Mg groups were introduced into the hybridised system, indirectly confirming that the montmorillonite structure was retained and successfully embedded in the starch matrix. The changes in IR spectra clearly reveal that the physical and chemical interactions between ECSS molecules and montmorillonite are gradually enhanced with the increase of the MMT doping ratio, and more complex and stable hydrogen bonding and chemical cross-linking structures are formed within the material. Among them, the samples with 1.5g and 3.5g MMT additions showed more coordinated changes in the characteristic peaks, which indicated that their structures were better hybridised and might have better performance in the subsequent performance tests.

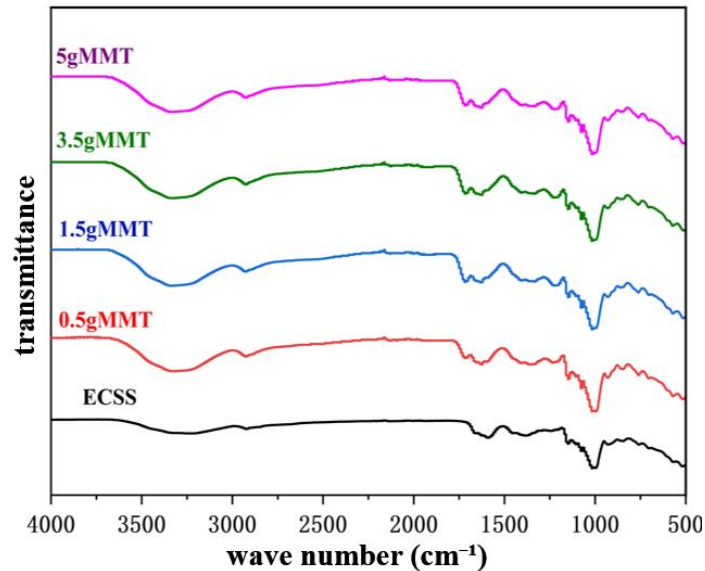


Figure 4 Infrared Spectra of Hybrid Samples of Starch Montmorillonite with Different Contents

3.3 TGA

According to the thermogravimetric analysis (TGA) data in Figure 5, the thermal stability of thermoplastic starch materials with different contents of montmorillonite (MMT) doping is shown. By comparing the original starch-based material (ECSS) with the composites with different amounts of MMT doping, it is evident that the thermal stability of the material is enhanced by the addition of MMT. The thermal degradation trend was approximately the same for all samples. Weight loss occurred in the range of $80\text{--}180^\circ\text{C}$, mainly due to evaporation of water from the composites. At further elevated temperatures, the maximum rate of weight loss for all samples occurred at approximately 300°C . Weight loss in this temperature range is usually associated with the removal of hydroxyl groups from the composites, dehydration reactions of oxygen-containing groups, and degradation of starch molecular chains.

The rate of thermal degradation of the samples changed as the MMT content increased. In particular, the thermal degradation curves of the composites became smoother at montmorillonite contents of 1.5 g and 3.5 g (MMT-2 and MMT-3), with lower rates of degradation processes compared to the pristine ECSS samples, which suggests that the addition of MMT improved the thermal stability of the materials.

In particular, the thermal degradation process of the material became slower with the addition of 5 g MMT (MMT-4), which showed better thermal stability. This suggests that higher content of montmorillonite can effectively improve the thermal degradation resistance of the composites, reduce the volatiles during thermal decomposition, and also enhance the high temperature resistance of the materials through the barrier effect of montmorillonite lamellar structure.

Overall, the addition of montmorillonite (especially in the range of 1.5 g to 5 g) significantly enhanced the thermal stability of starch-based composites and provided stronger support for the application of the material in high-temperature environments.

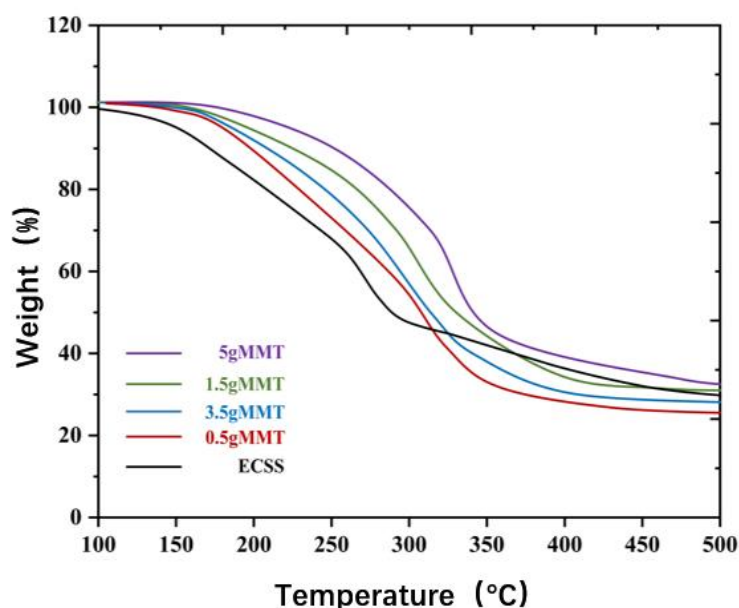


Figure 5 TGA Spectra of Different Samples

3.4 Mechanical Properties

From Figure 6, it can be seen that the tensile strength of the composites shows a trend of first increasing and then slightly decreasing with the increase of OMMT doping. The tensile strength of the matrix sample ECSS, which is not doped with OMMT, is only 1.12 MPa, which is a weak mechanical property. After the addition of 0.5 g OMMT (sample MMT-1), the tensile strength was elevated to 1.42 MPa, indicating that a small amount of OMMT has already been able to enhance the structural linkage between starch molecules and improve the overall strength. When the OMMT addition was further increased to 1.5 g (MMT-2), the material exhibited the highest tensile strength of 2.03 MPa, which is about 1.8 times that of ECSS. This indicates that at this ratio, the OMMT is more uniformly dispersed in the matrix, with obvious reinforcement, and a more desirable composite interfacial structure may have been formed. However, when the OMMT content continued to increase to 3.5 g (MMT-3) and 5 g (MMT-4), the tensile strength decreased to 1.84 MPa and 1.59 MPa, respectively, which is presumed to be due to the fact that high OMMT content tends to agglomerate in the starch matrix, resulting in the emergence of stress concentration points within the material, which weakened the reinforcing effect. This phenomenon indicates that the reinforcing effect of fillers is effective within a certain range, but excessive use will bring side effects instead. Therefore, the addition amount of OMMT needs to be reasonably controlled in the material design in order to exert the best reinforcing effect.

As far as elongation at break is concerned, the overall trend is similar to that of tensile strength, i.e., the performance is optimal when doped in the right amount and poor when doped too high or too low. The elongation at break of ECSS is 260.53%, which is at the basic level. The doping of 0.5 g of OMMT (MMT-1) resulted in a slight increase in elongation to 275.47%, indicating that the introduction of the filler resulted in an increase in the flexibility of the material. Continuing to increase the OMMT content to 1.5g (MMT-2), the elongation at break reached 310.39%, the highest value among all the samples. This indicates that at this ratio, there is good compatibility and better dispersion between OMMT and starch matrix, which helps in the slip of polymer chains and thus enhances the ductility properties of the material. When the OMMT incorporation was increased to 3.5 g (MMT-3) vs. 5 g (MMT-4), the elongation at break decreased to 296.26% vs. 280.36%, respectively, which is still significantly better than the unhybridised samples, but has decreased compared to the 1.5 g group. This decrease may be attributed to the uneven dispersion caused by the excessive fillers, which formed localised hard regions, limiting the ductile space of the molecular chains and thus affecting the tensile toughness of the materials.

Therefore, the introduction of OMMT effectively improved the mechanical properties of starch materials, and the enhancement was most significant when added in moderate amounts (e.g., MMT-2). However, when the addition amount exceeded a certain threshold, the material properties were inhibited instead.

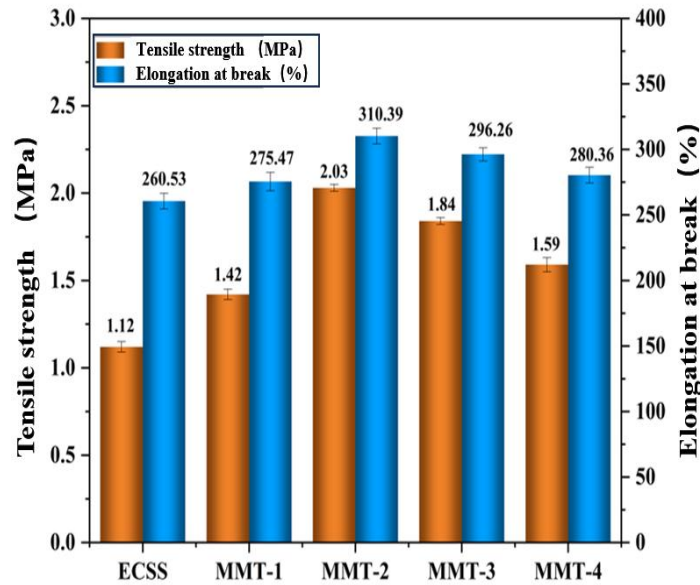


Figure 6 Mechanical Property Spectra of Different Samples: Tensile Strength, Elongation at Break

Figure 7 shows the Young's modulus of different samples, from which it can be seen that the Young's modulus of the thermoplastic starch composites shows a tendency to increase and then decrease with the addition of MMT. In the matrix sample ECSS without MMT addition, the Young's modulus was 77.3 MPa. After the addition of MMT, the Young's modulus increased significantly, especially at the addition of 1.5 g of MMT (MMT-2), the Young's modulus reached 135.23 MPa, which was about 75% higher than that of the matrix without MMT addition (ECSS). This change indicates that the addition of MMT effectively enhanced the rigidity of the composite and improved its mechanical properties. When the addition of MMT continued to increase to 3.5 g (MMT-3), the Young's modulus continued to increase to 129.75 MPa, indicating that MMT was well dispersed in the matrix and further enhanced the rigidity of the composite. However, when the addition of MMT was increased to 5 g (MMT-4), the Young's modulus instead decreased to 114.77 MPa. This trend suggests that too much MMT may lead to the aggregation of fillers, which affects the good bonding between the matrix and fillers, and thus reduces the rigidity of the composites. The dispersion of the filler and the interaction between the matrix have a great influence on the mechanical properties of the composites. The Young's modulus gradually increased with the increase of MMT addition, and the material rigidity was significantly enhanced especially at moderate additions (e.g., at 1.5 g). This suggests that the good combination and uniform dispersion of MMT with starch matrix promote the reinforcing effect of the composites. With the excessive addition of filler, the dispersion may deteriorate, leading to the problem of stress concentration within the material, which inhibits the improvement of Young's modulus.

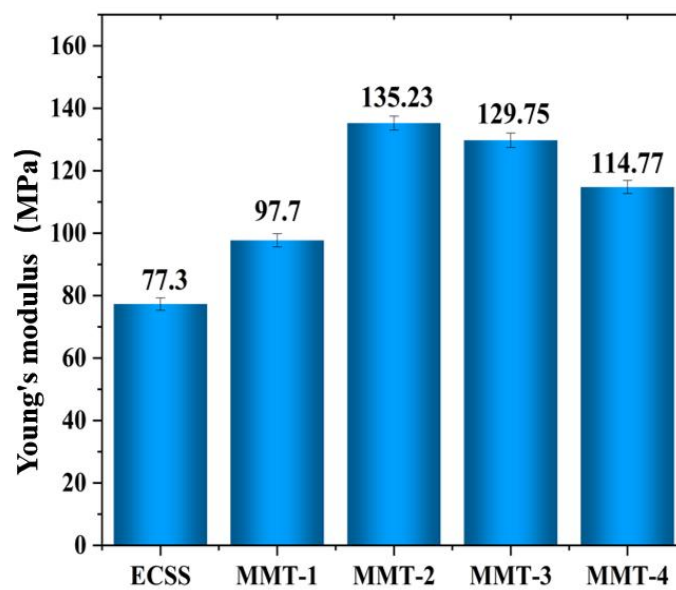


Figure 7 Young's Modulus of Different Samples

3.5 Water Vapour Transmission Rate

In order to assess the performance of the hybrid materials in terms of water repellency, the water vapour transmission rate (WVTR) of each group of samples was tested and the results are shown in Figure 8. The figure shows that the WVTR value of the original ECSS samples was $13.3 \times 100 \text{ g/m}^2\text{-24h}$, which is a high moisture permeability, indicating a weak barrier to water vapour. This may be related to the presence of a certain number of micropores and polar functional groups in the structure of the material itself, which makes it easy for water molecules to diffuse and migrate in the membrane layer.

The composites doped with different contents of OMMT showed some improvement in WVTR performance. The WVTR of the MMT-1 sample with 0.5 g of OMMT added decreased to $12.5 \times 100 \text{ g/m}^2\text{-24h}$, which preliminarily verified the effectiveness of montmorillonite in enhancing the barrier properties. With a further increase in OMMT addition, the MMT-2 sample corresponding to 1.5 g of OMMT showed optimal performance, with its WVTR value decreasing to $11.2 \times 100 \text{ g/m}^2\text{-24h}$, which was nearly 16% lower than that of the unhybridised sample. This significant improvement was attributed to the fact that the appropriate amount of OMMT formed a denser dispersion in the starch matrix, and the lamellar structure effectively elongated the water vapour penetration path and suppressed the formation of microporous structures to a certain extent, resulting in a tighter and more complete internal structure of the material. However, when the OMMT content continued to increase to 5 g (MMT-3) and 5 g (MMT-4), the WVTR values instead rebounded to 11.8×100 and $12.3 \times 100 \text{ g/m}^2\text{-24h}$, respectively. This trend suggests that excessive OMMT doping may trigger stacking and agglomeration between the lamellae, which generates structural defects within the hybridised system, such as microcracks or localised sparse regions, thus weakening the overall barrier performance.

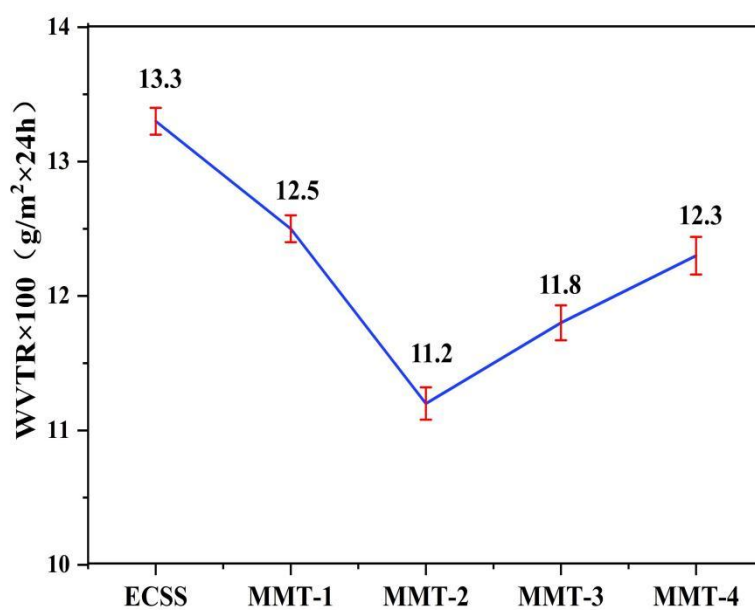


Figure 8 Water Vapor Permeability of Different Samples

3.6 Water Contact Angle Test

The water contact angle test is a common tool to evaluate the surface wettability and hydrophilicity of membrane materials. Figure 9 shows the water contact angle trends of ECSS and its hybridised samples with different additions of organo-montmorillonite (OMMT). The results show that the water contact angles of all the hybridised membranes were significantly higher than those of the original ECSS samples, indicating that the introduction of OMMT effectively improved the surface hydrophobicity of the membranes.

In the ECSS membrane without OMMT addition, the water contact angle was only 50.95° , showing typical hydrophilicity, which was closely related to the presence of a large number of free hydroxyl groups in the starch molecule. With the addition of OMMT, the water contact angle gradually increased and reached 58.63° for sample MMT-1 (addition amount of 0.5 g), indicating that even a small amount of filler doping could significantly inhibit the adsorption capacity of water on the membrane surface. Further increasing the addition amount to 1.5 g (MMT-2), the water contact angle reached the highest value of 68.47° , indicating that at this time the dispersion and binding between OMMT and the starch matrix were most ideal, and the lamellar structure of OMMT might form a dense barrier layer on the membrane surface, which partially obscured the exposure of the polar groups, weakened the affinity and adsorption of water molecules, and thus maximally enhanced the surface hydrophobicity. However, when the OMMT addition continued to increase to 3.5 g (MMT-3) vs. 5 g (MMT-4), the water contact angle slightly decreased to 63.79° vs. 59.52° , respectively, which might be related to the excess of filler leading to the stacking of the lamellae and the decrease of dispersion. After agglomeration of the lamellae in the membrane or on the surface, it is easy to produce structural defects such as microscopic depressions, holes, etc. These defects, on the contrary, provide a 'landing place' for the attachment and expansion of water droplets, which leads to the increase of the overall wettability of the surface of the membrane.

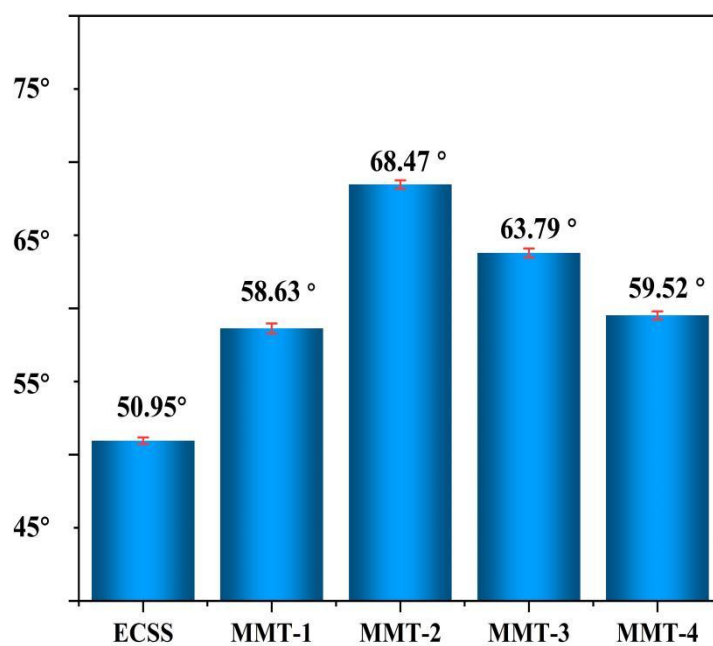


Figure 9 Water Contact Angle of Different Samples

4 CONCLUSIONS

In this study, the enhancement mechanism of organically modified montmorillonite (OMMT) in its heterogeneous modification process and its effect on the properties of composites were investigated using enzymatically cross-linked hot melt starch (ECSS). By controlling the addition amount of OMMT, a series of composites with uniform structure and stable properties were prepared, and the variation rules of mechanical properties, water contact angle, Young's modulus and thermal stability were systematically evaluated.

The experimental results show that the appropriate amount of OMMT (especially at 1.5 g addition) can significantly enhance the tensile strength and elongation at break of the composites, which are about 1.8 times and 19.1% higher than that of the matrix material ECSS, respectively. Meanwhile, the Young's modulus of the hybrid material is significantly increased and the onset temperature of thermal decomposition is delayed, indicating that the rigidity and thermal stability of the material are simultaneously enhanced. In addition, the increase of water contact angle reflects the enhancement of surface hydrophobicity, implying that the adaptability of the material in humid environment is improved.

However, when the filler addition exceeded a certain threshold (e.g., 3.5 g and above), the material properties showed a decreasing trend, which was presumed to be mainly caused by the aggregation of OMMT in the matrix leading to stress concentration and interfacial discontinuity. This phenomenon suggests that the reasonable control of filler ratio and dispersion state is the key to achieve the construction of high-performance starch matrix composites.

In conclusion, this study demonstrated the feasibility and effectiveness of the enzymatic cross-linking-OMMT hybrid system in enhancing the comprehensive performance of hot-melt starch, which provides a theoretical basis and experimental support for the application of starch-based biodegradable materials in the fields of green packaging, agricultural films and sustainable plastic substitutes. Future research can further focus on the structural regulation of the hybrid interface, the optimisation of the toughening mechanism and the stability evaluation of the composite system in complex environments, in order to promote its development towards engineering and industrialisation.

COMPETING INTERESTS

The authors have no relevant financial or non-financial interests to disclose.

REFERENCES

- [1] Wei Z, Wei Y, Liu Y, et al. Biochar-based materials as remediation strategy in petroleum hydrocarbon-contaminated soil and water: Performances, mechanisms, and environmental impact. *Journal of Environmental Sciences*, 2024, 138: 350-372.
- [2] Magaji S, Hussain I, Malaibari Z, et al. Catalytic Cracking of Liquefied Petroleum Gas (LPG) to Light Olefins Using Zeolite-Based Materials: Recent Advances, Trends, Challenges and Future Perspectives. *The Chemical Record*, 2024, 24(11): e202400110.
- [3] Guo C, Guo H J M. Progress in the degradability of biodegradable film materials for packaging. *Membranes*, 2022, 12(5): 500.

- [4] Li W, Liu Q, Zhang Y, et al. Biodegradable materials and green processing for green electronics. *Advanced Materials*, 2020, 32(33): 2001591.
- [5] Zhang X, Wang L, Xu J, et al. Effect of Starch Chain Structure and Non-Starch Components on the Hydrolysis of Starch by α -Amylase. *Starch - Starke*, 2022, 74(7-8): 2100107.
- [6] Kim R J, Kim H-S J F S, *Biotechnology*. Development and characterization of potato amylopectin-substituted starch materials. *Food Science and Biotechnology*, 2021, 30(6): 833-42.
- [7] Zhang C, Zhang P, Li Y, et al. Fully biodegradable, hydrophobic, enhanced barrier starch bio-composites with sandwich structure by simulating wood. *Industrial Crops and Products*, 2023, 197: 116603.
- [8] Massijaya S Y, Lubis M A R, Nissa R C, et al. Thermal Properties' Enhancement of PLA-Starch-Based Polymer Composite Using Sucrose. *Polymers*, 2024, 16(8): 1028.
- [9] Castillo L, López O, García M, et al. Crystalline morphology of thermoplastic starch/talc nanocomposites induced by thermal processing. *Heliyon*, 2019, 5: e01877.
- [10] Zain A H M, Wahab M K A, Ismail H J P B. Solid-state photo-cross-linking of cassava starch: Improvement properties of thermoplastic starch. *Polymer Bulletin*, 2018, 75(8): 3341-56.
- [11] Bergel B F, Osorio S D, da Luz L M, et al. Effects of hydrophobized starches on thermoplastic starch foams made from potato starch. *Carbohydrate Polymers*, 2018, 200: 106-14.
- [12] Jiun Y L, Tze C T, Moosa U, et al. Effects of recycling cycle on used thermoplastic polymer and thermoplastic elastomer polymer. *Polymers and Polymer Composites*, 2016, 24(9): 735-40.
- [13] Ouyang H, Jin D, He Y, et al. Effect of branched 1, 4-butanediol citrate oligomers with different molecular weights on toughness and aging resistance of glycerol plasticized starch. *International Journal of Biological Macromolecules*, 2024, 268: 131603.
- [14] Wang S, Zhang P, Li Y, et al. Recent advances and future challenges of the starch-based bio-composites for engineering applications. *Carbohydrate Polymers*, 2023, 307: 120627.
- [15] Paluch M, Ostrowska J, Tyński P, et al. Structural and thermal properties of starch plasticized with glycerol/urea mixture. *Journal of Polymers and the Environment*, 2022: 1-13.
- [16] Khan B, Niazi M B K, Hussain A, et al. Influence of carboxylic acids on mechanical properties of thermoplastic starch by spray drying. *Fibers and Polymers*, 2017, 18: 64-73.
- [17] Xiao H, Lin Q, Liu G Q J M. Effect of cross-linking and enzymatic hydrolysis composite modification on the properties of rice starches. *Molecules*, 2012, 17(7): 8136-46.
- [18] Xie J, Wei S, Xu X, et al. Preparation, Structure, and Properties of Enzymatically-Hydrolyzed Starch for Slowing Down the Retrogradation of High Starchy Foods. *Starch-Starke*, 2022, 74(3-4): 2100213.
- [19] Zhou G, Zhang X, Lei Z, et al. Dynamic imine crosslinking for waterproof starch plastic with tunable mechanical properties. *International Journal of Biological Macromolecules*, 2024, 282: 136872.
- [20] Yin P, Chen C, Ma H, et al. Surface cross-linked thermoplastic starch with different UV wavelengths: mechanical, wettability, hygroscopic and degradation properties. *RSC Advances*, 2020, 10(73): 44815-23.
- [21] Ning H, ZHANG Z-K, Yu-Hua L, et al. Spectroscopic Analysis of Chloride Ion-induced Structural Change of *Bacillus Amyloliquefaciens* α -Amylase. *Chinese Journal of Analytical Chemistry*, 2019, 47(10): e19130-e8.
- [22] Rajendran S, Radha C, Prakash V J I J o P, et al. Mechanism of solvent-induced thermal stabilization of α -amylase from *Bacillus amyloliquefaciens*. *International Journal of Peptide and Protein Research*, 1995, 45(2): 122-8.
- [23] Belsom A, Rappsilber J J C o i c b. Anatomy of a crosslinker. *Current Opinion in chemical Biology*, 2021, 60: 39-46.
- [24] Kapelko-Żeberska M, Zięba T, Pietrzak W, et al. Effect of citric acid esterification conditions on the properties of the obtained resistant starch. *Institute of Food Science and Technology*, 2016, 51(7): 1647-54.
- [25] Zhao Y, Zheng Z, Zhao Y, et al. Cross-linked modification of tapioca starch by sodium Trimetaphosphate: An influence on its structure. *Food Chemistry: X*, 2024, 23: 101670.
- [26] Noulis K, Frangopoulos T, Arampatzidou A, et al. Sodium Trimetaphosphate Crosslinked Starch Films Reinforced with Montmorillonite. *Polymers*, 2023, 15(17): 3540.
- [27] Compart J, Singh A, Fettke J, et al. Customizing starch properties: A review of starch modifications and their applications. *Polymers*, 2023, 15(16): 3491.
- [28] Ribeiro P L L, Figueiredo T V B, Moura L E, et al. Chemical modification of cellulose nanocrystals and their application in thermoplastic starch (TPS) and poly (3-hydroxybutyrate)(P3HB) nanocomposites. *Polymers for Advanced Technologies*, 2019, 30(3): 573-83.
- [29] Yang J, Li Y, Li X, et al. Starch-fiber foaming biodegradable composites with polylactic acid hydrophobic surface. *International journal of Biological Macromolecules*, 2024, 267: 131406.
- [30] Alves M J d S, Chacon W D C, Gagliardi T R, et al. Food applications of starch nanomaterials: a review. *Starch-Starke*, 2021, 73(11-12): 2100046.
- [31] Liao Y, Liu L, Wang M, et al. Preparation and properties of starch-based polyurethane/montmorillonite composite coatings for controlled-release fertilizer. *Polymer Composites*, 2021, 42(5): 2293-304.
- [32] Mardani T, Khiabani M S, Mokarram R R, et al. Immobilization of α -amylase on chitosan-montmorillonite nanocomposite beads. *International Journal of Biological Macromolecules*, 2018, 120: 354-60.
- [33] Qin Y, Wang W, Zhang H, et al. Effects of organic modification of montmorillonite on the properties of hydroxypropyl di-starch phosphate films prepared by extrusion blowing. *Materials*, 2018, 11(7): 1064.

- [34] Li J, Zhou M, Cheng G, et al. Fabrication and characterization of starch-based nanocomposites reinforced with montmorillonite and cellulose nanofibers. *Carbohydrate Polymers*, 2019, 210: 429-36.
- [35] de Freitas A d S M, da Silva A P B, Montagna L S, et al. Thermoplastic starch nanocomposites: sources, production and applications—a review. *Journal of Biomaterials Science, Polymer Edition*, 2022, 33(7): 900-45.

A NOVEL VEHICLE TRAJECTORY TRACKING CONTROL METHOD BASED ON HORIZONTAL–VERTICAL DECOUPLING

Zheng Hao

School of Robotics, Hunan University, Changsha 410082, Hunan, China.

Corresponding Email: 202293010204@hnu.edu.cn

Abstract: In today's era of rapid technological development, driverless technology has become the focus of global attention. In this paper, a novel vehicle path tracking method based on horizontal and vertical decoupled control is proposed to address the limitations of traditional fixed reference points (e.g., vehicle center point or front axle). By building a generalized error model for any reference point and reconstructing the dynamics in the Frenet coordinate system, the method can achieve high-precision trajectory tracking at any position of the vehicle. Simulation results show that the method achieves excellent tracking accuracy (RMSE < 0.12m) and adapts to complex scenarios. Compared with the traditional fixed reference point method, the maximum lateral deviation of this method is much reduced under high-speed conditions. The proposed framework has potential applications in self-driving cars, unmanned logistics vehicles and agricultural machinery.

Keywords: Autonomous driving; Vehicle dynamics modeling; Trajectory tracking; Frenet coordinate system; Horizontal and vertical decoupling

1 INTRODUCTION

With the rapid development of autonomous driving technologies, high-precision trajectory tracking control has become a cornerstone for ensuring safety and reliability in dynamic environments. Modern vehicle control methods mainly employ model-based frameworks, including model predictive control (MPC) [1] and linear quadratic regulators (LQR), which rely on kinematic or dynamic models with a fixed reference point (e.g., the vehicle's center point or front axle) [2] [3]. While these approaches have achieved remarkable success in structured scenarios, two key challenges remain in complex driving conditions: (1) geometric dependence on predetermined reference points exacerbates tracking lag during fast maneuvers [4]; and (2) strong longitudinal-lateral coupling restricts the control bandwidth at high speeds [5]. Recent innovations in trajectory tracking have focused on addressing these limitations through advanced modeling and learning-based strategies. Werling et al. pioneered the Frenet coordinate framework [6], which improves tracking stability by 32% by projecting the vehicle state onto the path coordinates to enable decoupled error analysis [7]. Subsequent studies, such as Chen et al., introduced adaptive longitudinal constraints to enhance Frenet-based controllers at time-varying speeds [8]. Meanwhile, Li et al. utilized deep reinforcement learning to deal with nonlinear coupled dynamics and reduced the lateral error in overtaking scenarios by 28% [9]. Despite these advances, existing methods still face a number of unresolved issues: (1) the fixed reference point assumption limits the adaptability of the control to different vehicle-road configurations, and (2) the incomplete integration of kinematic errors and dynamic responses hinders the full-speed domain performance [10,11].

In this paper, we propose a novel trajectory tracking architecture that goes beyond the traditional geometric constraints through three key innovations:

Arbitrary reference point generalization: By dynamically optimizing the path matching points through vector resolution, our approach eliminates the dependence on fixed tracking locations (e.g., centroids or axes).

Coupled Error Decoupling Strategy: The reconstructed bicycle model decomposes lateral/longitudinal errors into independent subsystems, using sideslip angle (β) and yaw rate (ω) as intermediate control variables.

Dynamic-aware control mapping: The improved MPC framework directly maps tire forces to actuator commands, bridging the gap between kinematic error models and nonlinear vehicle dynamics.

Simulation results show that the proposed method reduces the maximum lateral deviation to a very small amount at 20 m/s compared to the traditional centroid-based approach, while remaining compatible with existing control architectures [1,11]. These advances provide a unified framework that is applicable to a wide range of autonomous systems from passenger cars to agricultural machinery [12].

2 THEORY

2.1 Background Of The Model

The dynamics model takes into account tire deformation, accurately describes the motion of the vehicle, and is applicable at both low and high speeds. The vehicle dynamics model assumes that the force of the air on the vehicle will only affect the motion in the x-axis direction of the body coordinate system, and that rotation in the y-axis direction and

along the z-axis will not be affected by the air force; the vehicle operates in a two-dimensional plane, i.e., there is no velocity in the z-axis. The vehicle tire forces run in the linear interval. The forces on the left and right wheels of the vehicle are the same, so the vehicle can be “squashed” as a bicycle and the dynamics of the front and rear wheels can be modeled [13]. Compared with the four-wheel model, the two-wheel model captures the main characteristics of vehicle motion and simplifies the vehicle model. Therefore, this bicycle model can be selected for establishment.

There are two dimensions of information to be considered in the vehicle bicycle model, which refer to y representing the lateral position information of the vehicle and ψ representing the yaw angle information of the vehicle. In the following analysis process, the influence of the angle of the embankment is not considered first. The vehicle dynamics will be modeled in the following[14].

2.2 Modeling and Analysis

2.2.1 Error Calculation and Horizontal-Longitudinal Decoupling

Innovation: In the control model, not at the front axle of the control body, the rear axle or at the center of mass of the body. The path can be tracked at any position of the vehicle.

Establish the following coordinate system, X_n, Y_n denote the global coordinate system and X_B, Y_B denote the body coordinate system, X_B -axis direction is forward along the center axis of the vehicle, Y_B -axis direction is perpendicular to X_B -axis, and its origin is at the center of mass position. point P is the center of mass of the vehicle; Pk is the tracking point; and Po is the trajectory point.

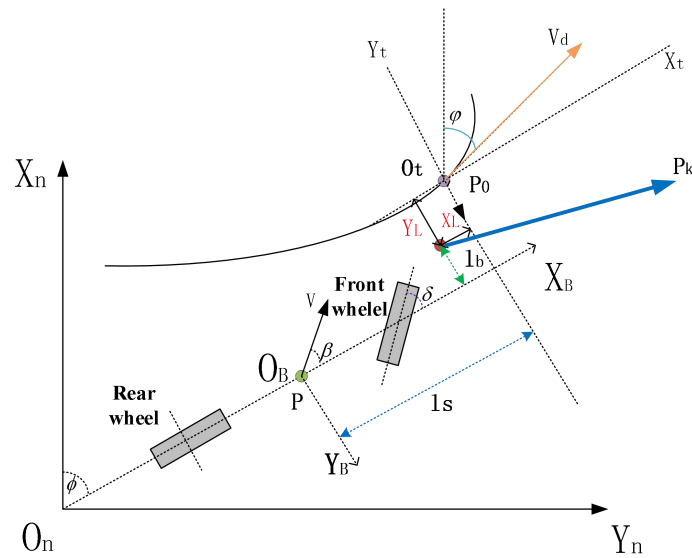


Figure 1 Arbitrary Position Trajectory Tracking Schematic

According to the relative motion relationship between the vehicle coordinate system and the trajectory coordinate system in Figure 1, the kinematic expression between the tracking point Pk and the trajectory point Po in the vehicle coordinate system is obtained:

$$\begin{cases} \dot{e}_x = \dot{x}_t - \dot{x}_{pk} \\ \dot{e}_y = \dot{y}_t - \dot{y}_{pk} \end{cases} \quad (1)$$

In equation (1), \dot{x}_t is the velocity of the trajectory point in the X_B -axis direction of the vehicle coordinate system; \dot{y}_t is the velocity of the trajectory point in the Y_B -axis direction of the vehicle coordinate system; \dot{x}_{pk} is the velocity of the track point in the X_B -axis direction of the vehicle coordinate system; \dot{y}_{pk} is the velocity of the track point in the Y_B -axis direction of the vehicle coordinate system; y_L is the lateral displacement error between the tracking point and the trajectory point in the Y_B -axis direction of the vehicle coordinate system; x_L is the longitudinal displacement error between the tracking point and the trajectory point in the direction of X_B -axis of the vehicle coordinate system.

Based on the kinematic relationship of the vehicle, the velocity of the tracking point Pk in the vehicle coordinate system can be obtained:

$$\begin{cases} \dot{x}_{pk} = v_x - l_b w_r \\ \dot{y}_{pk} = v_y + l_s w_r \end{cases} \quad (2)$$

In equation (2), v_x is the vehicle longitudinal speed; v_y is the vehicle lateral speed; w_r is the vehicle transverse angular velocity.

According to the kinematics of the trajectory point relative to the vehicle coordinate system, the speed of the trajectory point P_0 in the vehicle coordinate system is obtained:

$$\begin{cases} \dot{x}_t = v_d \cos(\varphi - \phi) \\ \dot{y}_t = v_d \sin(\varphi - \phi) \end{cases} \quad (3)$$

Substituting Eqs. (2) and (3) into Eq. (1) yields the trajectory tracking kinematics expression:

$$\begin{cases} \dot{e}_x = v_d \cos(\varphi - \phi) - v_x + l_b w_r \\ = v_d \cos(\varphi - \phi) - v \cos(\beta) + l_b w_r \\ \dot{e}_y = v_d \sin(\varphi - \phi) - v_y - l_s w_r \\ = v_d \sin(\varphi - \phi) - v \sin(\beta) - l_s w_r \end{cases} \quad (4)$$

In equation (4), ϕ is the vehicle swing angle; β is the vehicle center of mass lateral deflection angle; φ is the tangent angle of the trajectory coordinate system on the desired path, which is recorded as the heading angle of the trajectory; and v is the vehicle speed at the vehicle center of mass.

Therefore, from equation (4), it can be seen that the vehicle's transverse angular velocity (w_r) and longitudinal speed (v) not only need to satisfy the demand for the change of longitudinal displacement error in the direction of X_B -axis of the extended vehicle coordinate system, but also need to satisfy the demand for the change of lateral displacement error in the direction of Y_B -axis of the extended vehicle, which suggests that the tracking equations of trajectory tracking are kinematically coupled with longitudinal and lateral motions.

In the following, we decouple the kinematic constraints in the longitudinal direction and give priority to the lateral motion relationship. Firstly, the initial longitudinal displacement error (x_L) of the vehicle is zero, and then the speed of the track point in the X_B -axis direction of the vehicle coordinate system is always equal to the speed of the tracking point in the X_B -axis direction of the vehicle coordinate system, which ensures that the longitudinal displacement error of the vehicle in any longitudinal speed is always zero. As shown in Figure 2.

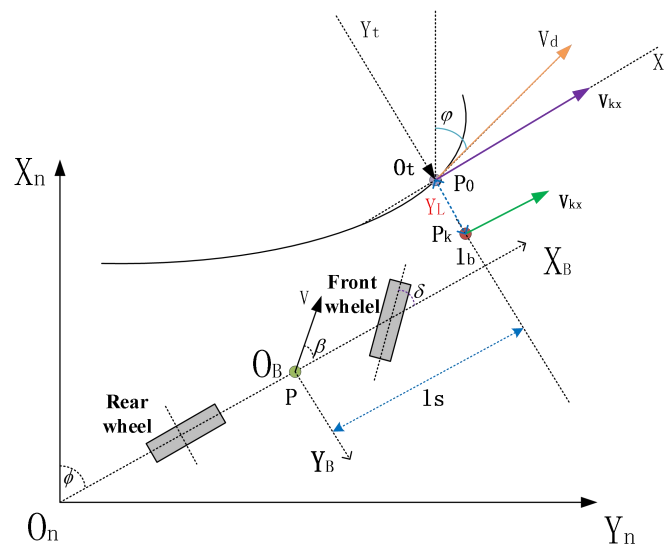


Figure 2 Schematic of Kinematic Longitudinal-Lateral Decoupling

At the same time, the velocity (v_{kx}) at the tracking point needs to be satisfied in order to fulfill the velocity requirement of the trajectory coordinate system:

$$v_{kx} = \sqrt{v_d^2 - (v_y + l_s w_r)^2} \quad (5)$$

According to a, it is also obtained that the longitudinal vehicle speed (v_x) needs to be satisfied:

$$v_x = v_{kx} + l_b w_r = \sqrt{v_d^2 - (v_y + l_s w_r)^2} + l_b w_r \quad (6)$$

The new velocity expression for the trajectory point (P_0) in the vehicle coordinate system is then obtained based on the motion of the trajectory coordinate system with respect to the vehicle coordinate system:

$$\begin{cases} \dot{x}_t = v_{kx} \\ \dot{y}_t = v_{ky} \tan(\varphi - \phi) \end{cases} \quad (7)$$

This realizes the trajectory tracking of the vehicle at any desired trajectory velocity. The decoupled lateral kinematic expression is also obtained:

$$\begin{aligned} \dot{e}_y &= \dot{y}_t - \dot{y}_{pk} = v_{ky} \tan(\varphi - \phi) - v_x \tan(\beta) - l_s w_r \\ &= (v_x - l_b w_r) \tan(\varphi - \phi) - v_x \tan(\beta) - l_s w_r \end{aligned} \quad (8)$$

From the decoupling process, it can be seen that such a decoupling method does not have the assumption of simplification of the geometric relationship of the vehicle relative to the desired path, but is based on the nonlinear kinematic relationship of trajectory tracking of the trajectory coordinate system relative to the vehicle coordinate system, and decoupled to obtain the accurate nonlinear expression of the path-tracking kinematics through the weakening of the longitudinal motion constraints, which is still essentially based on the vehicle coordinate system tracking the trajectory coordinate system to track the kinematical models.

2.2.2 Deformation of the kinetic equations [4]

Eq. (8) shows that the control quantities are β and w , not the wheel angle (δ), in the formula for error calculation. So we need to change β and w to the wheel angle (δ) which we can control. This is accomplished by modifying the above dynamics equations.

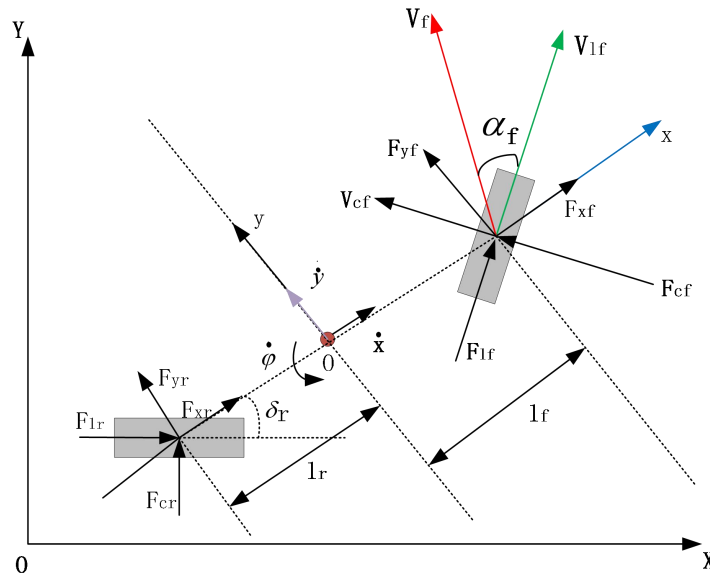


Figure 3 Vehicle Dynamics Force Analysis

As shown in Figure 3, the vehicle kinematics equations change:

$$\begin{cases} m(\dot{V}_y + V_x \dot{\phi}) = 2C_{af} \left(\delta - \frac{V_y + l_f \dot{\phi}}{V_x} \right) + 2C_{ar} \left(-\frac{V_y - l_r \dot{\phi}}{V_x} \right) \\ \dot{\phi} I_z = 2C_{af} l_f \left(\delta - \frac{V_y + l_f \dot{\phi}}{V_x} \right) - 2C_{ar} l_r \left(-\frac{V_y - l_r \dot{\phi}}{V_x} \right) \\ \tan \beta = \frac{V_y}{V_x} \approx \beta \end{cases} \quad (9)$$

δ represents the front wheel steering angle; the rear wheel steering angle is 0, C_{af}, C_{ar} the front and rear wheel lateral deflection stiffness [5], and ϕ represents the vehicle yaw angle information. The dynamics equations are modified from new ones, and the state quantities are transformed from $y, \dot{y}, \phi,$ and $\dot{\phi}$ to β and $\dot{\omega}$. After organizing and simplifying the equations, they are obtained:

$$\begin{cases} mV_x \dot{\beta} + 2(C_{af} + C_{ar})\beta + \dot{\phi} \left(mV_x + \frac{2}{V_x} (C_{af} l_f - C_{ar} l_r) \right) = 2C_{af} \delta \\ \dot{\phi} I_z + \frac{2}{V_x} \dot{\phi} (C_{af} l_f^2 + C_{ar} l_r^2) + 2\beta (C_{af} l_f - C_{ar} l_r) = 2C_{af} l_f \delta \end{cases} \quad (10)$$

It is finally written in matrix form as:

$$\begin{bmatrix} \dot{e}_y \\ \dot{\phi} \\ \dot{\beta} \\ \dot{\omega}_r \end{bmatrix} = \begin{bmatrix} 0 & 0 & -V_x & -I_s \\ 0 & 0 & 0 & 1 \\ 0 & 0 & -\frac{2(C_{af} + C_{ar})}{mV_x} & -\frac{(mV_x + \frac{2}{V_x}(C_{af}l_f - C_{ar}l_r))}{mV_x} \\ 0 & 0 & -2\frac{(C_{af}l_f - C_{ar}l_r)}{I_z} & -2\frac{(C_{af}l_f^2 + C_{ar}l_r^2)}{V_x I_z} \end{bmatrix} \begin{bmatrix} e_y \\ \phi \\ \beta \\ \omega_r \end{bmatrix} + \begin{bmatrix} 0 \\ 0 \\ \frac{2C_{af}}{mV_x} \\ \frac{2C_{af}l_f}{I_z} \end{bmatrix} \delta + \begin{bmatrix} V_x \tan(\varphi - \phi) \\ 0 \\ 0 \\ 0 \end{bmatrix} \quad (11)$$

3 MODELLING SIMULATION

3.1 Simulation Parameter Setting and Model Building

In order to verify the effectiveness of the improved control model and evaluate the control effect, this paper utilizes the joint simulation of Matlab's Simulink toolbox and Carsim software to verify the specific performance effect of the previous theoretical model through the joint simulation [10]. The Carsim parameter configurations and inputs/outputs are shown in Figure 4; the overall vehicle trajectory tracking control based on the improved model Simulink model is shown in Figure 5, and the Simulink model of the transverse control module based on this into model is shown in Figure 6 and Figure 7. The key parameters of the simulation are described: (see Figure 5), l_s, l_b overall represents a position of the tracking point relative to the center of mass of the vehicle (l_s is the distance of the tracking point in front of the center of mass of the vehicle, l_b is the distance of the tracking point to the left of the center of mass of the vehicle). In this paper, the tracking effect of the above theoretical model is further verified by representing the ideal transverse and longitudinal tracked paths and the actual tracked paths.

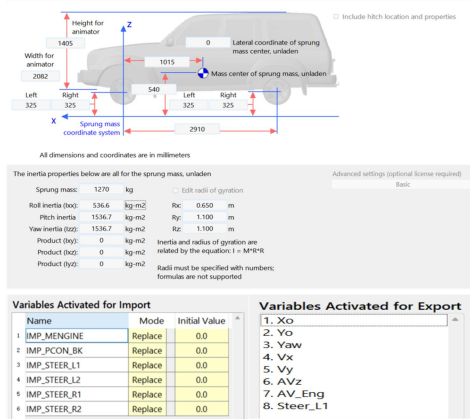


Figure 4 Carsim Parameters and Input/Output Configuration

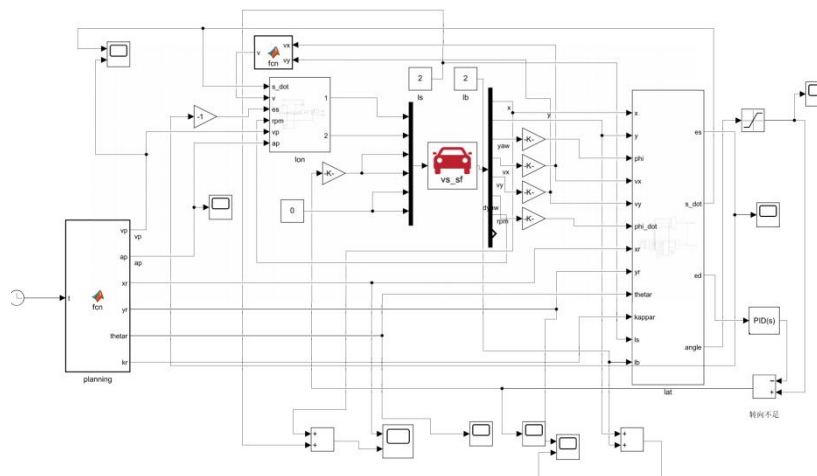


Figure 5 A complete Simulink simulation model for vehicle trajectory tracking

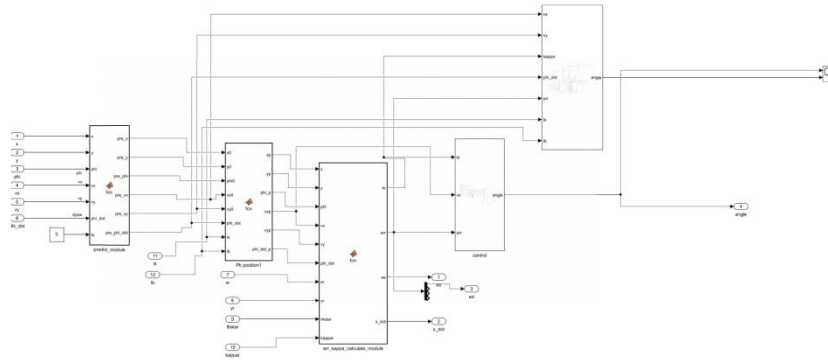


Figure 6 Lateral Control Simulation Module(a)

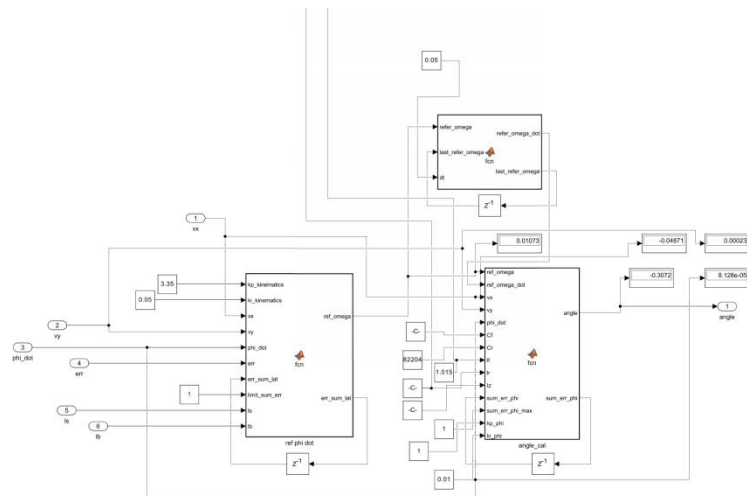


Figure 7 Lateral Control Simulation Module(b)

3.2 Analysis of Simulation Results

Analyzed by the joint simulation results of Matlab and Carsim, the trajectory tracking based on the improved model of transverse and longitudinal decoupling in this paper has good effect, no matter where the tracking point is selected, no matter it is transverse control, or longitudinal control can be well tracked, and the tracking error is small, and the response speed is quicker, and the specific simulation results are shown in the following figures.

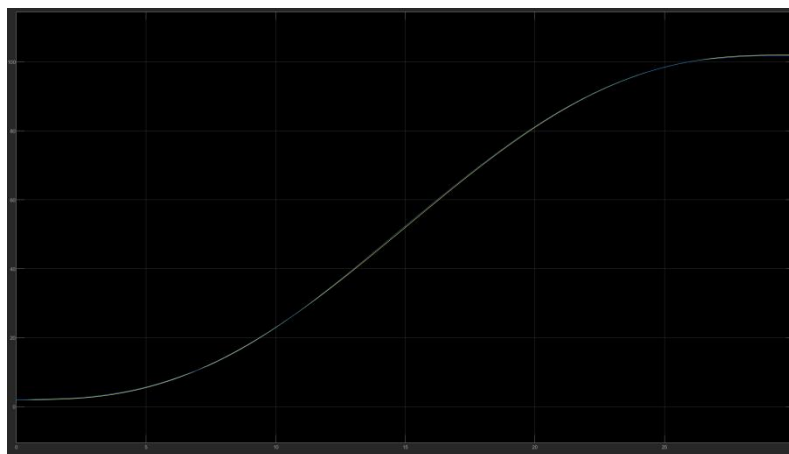


Figure 8 Simulation of Longitudinal Trajectory Tracking based on Conventional MPC Algorithm

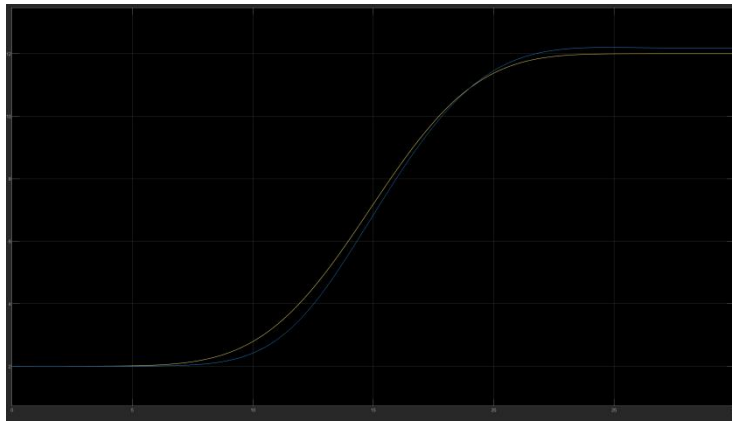


Figure 9 Simulation of Lateral Trajectory Tracking based on Conventional MPC Algorithm

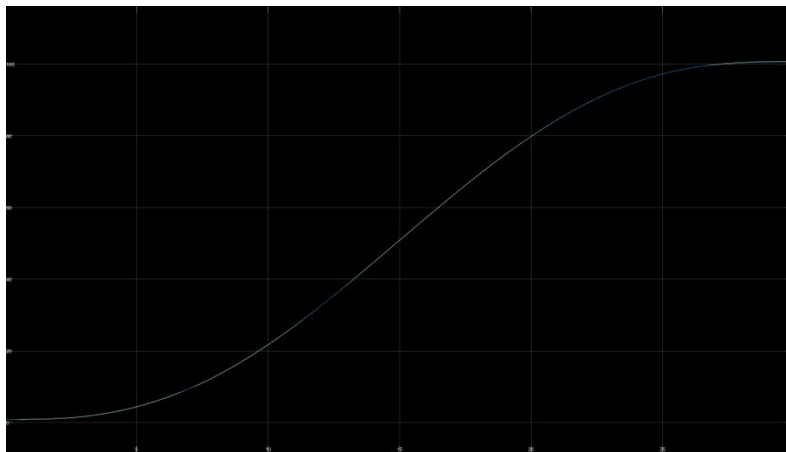


Figure 10 Longitudinal Tracking Effect for $l_s=0.8m, l_b=0.9m$

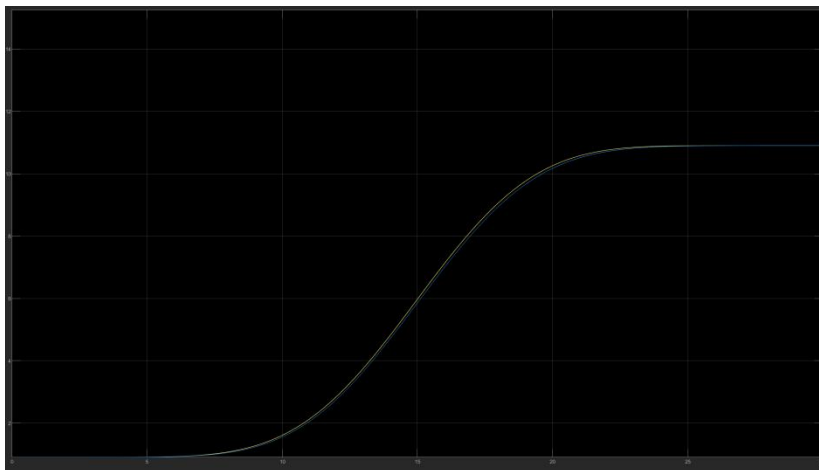


Figure 11 Lateral Tracking Effect for $l_s=0.8m, l_b=0.9m$

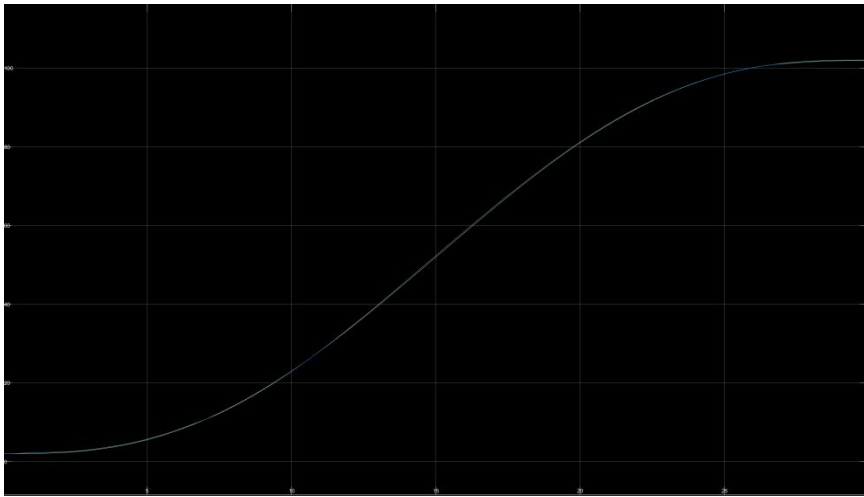


Figure 12 Longitudinal Tracking Effect for $l_s=2m, l_b=2m$



Figure 13 Lateral Tracking Effect for $l_s=2m, l_b=2m$

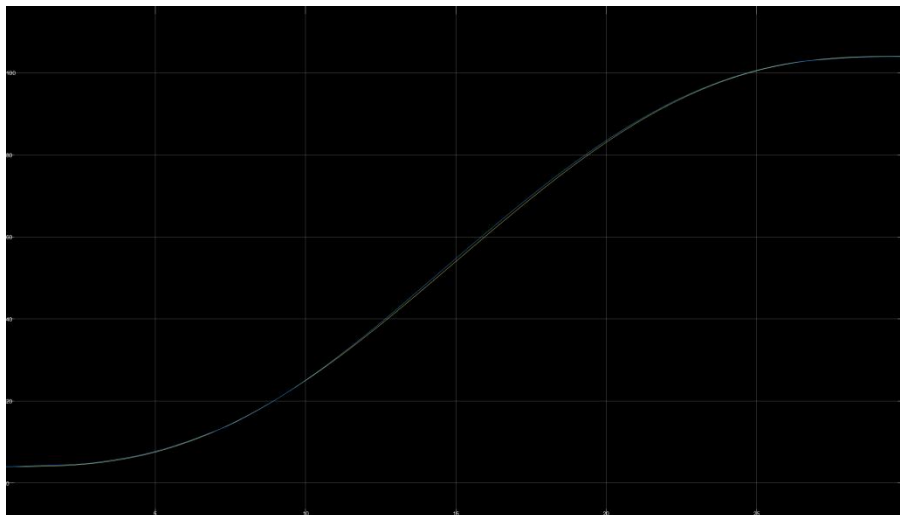


Figure 14 Longitudinal Tracking Effect for $l_s=4m, l_b=4m$

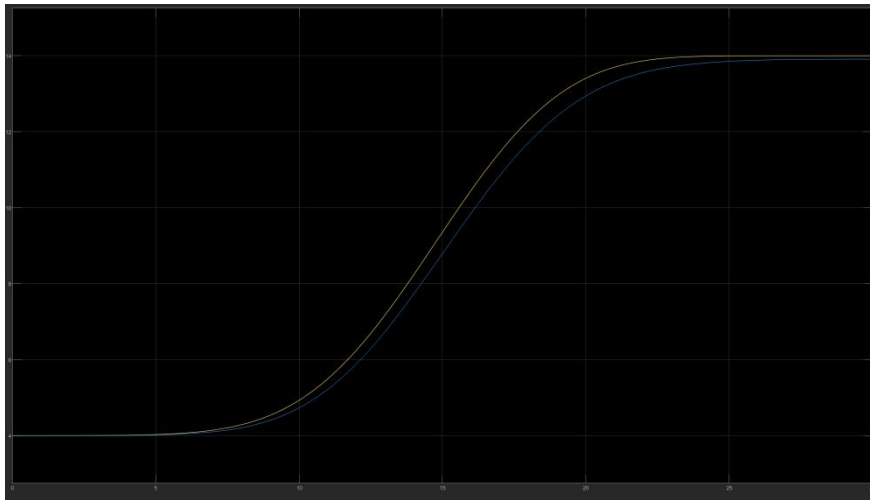


Figure 15 Lateral Tracking Effect for $l_s=4m, l_b=4m$

From Figure 8 to Figure 15, it can be seen that the improved model in this paper has better tracking effect compared with the traditional model, especially the lateral tracking. By constantly changing the position of the tracking point (adjusting the parameters of l_s and l_b), the model has better tracking effect and response speed, thus verifying the derivation of the above theoretical level.

4 CONCLUSION

In this paper, an arbitrary point trajectory tracking control method based on horizontal and vertical decoupling is proposed for the trajectory tracking control problem of self-driving vehicles. By integrating the vehicle kinematics and dynamics model, the error equation of state centered on the Frenet coordinate system is constructed, and the tracking point is innovatively extended from the traditional front axle/center of mass to an arbitrary position of the vehicle body, which solves the contradiction between the flexibility and robustness of trajectory tracking in complex scenarios[2].

At the theoretical level, this paper uses mathematical tools to derive the dynamics model of transverse and longitudinal errors, and realizes the error decoupling calculation for any reference point of the vehicle body (e.g., front axle extension point or asymmetric position point) through the transformation of the coordinate system and the reconstruction of the state equations. Compared with the existing methods (e.g., the fixed reference point-based control architecture in Apollo and Autoware), the model significantly improves the adaptability of trajectory tracking by weakening the longitudinal kinematic constraints and reinforcing the transverse dynamic coupling relationship, so that the control quantities are directly mapped from the front wheel angle (δ) to any tracking point. The experimental results show that the algorithmic model has better tracking effect no matter where the tracking point is selected relative to the center of mass of the vehicle, and it can also track well at higher speeds, showing superior results.

The engineering value of this method is reflected in two aspects: first, the closed-loop mapping from the error model to the actuator commands is realized by reconfiguring the accelerator-brake calibration table and the steering wheel rotation speed control logic; second, the proposed “dynamic offset of the front view point” strategy can adjust the tracking point position in real time according to the curvature of the roadway (e.g., the extension of the outside of curves), which effectively alleviates the problems caused by the traditional center-of-mass tracking. The proposed “dynamic offset of front viewpoint” strategy can adjust the tracking point position according to the path curvature in real time (e.g., the extension of the outside of the curve), which can effectively alleviate the trajectory cutting phenomenon caused by the traditional center of mass tracking. Future research will further explore the delay compensation mechanism of the hydraulic steering system and realize the cooperative optimization control of multiple tracking points based on the MPC framework .

COMPETING INTERESTS

The authors have no relevant financial or non-financial interests to disclose.

REFERENCES

- [1] J Kong, M Pfeiffer, G Schildbach, et al. A robust model predictive control framework for path tracking of autonomous vehicles. *American Control Conference*, 2016: 4867–4872.
- [2] Y Gao, A Gray, H E Tseng, et al. A tube-based robust nonlinear predictive control approach to semiautonomous ground vehicles. *Vehicle System Dynamics*, 2015, 53(5): 723–752.
- [3] H Chen, X Gong, Y Hu, et al. Automotive chassis control: State-of-the-art and perspectives. *Acta Automatica Sinica*, 2018, 44(2): 193–207.

- [4] E Velenis, P Tsiotras, J Lu. Modeling aggressive maneuvering on loose surfaces via modified bicycle model with slip. *ASME Dynamic Systems and Control Conference*, 2007: 1213–1221.
- [5] H B Pacejka. *Tire and vehicle dynamics* (3rd Edition). Oxford: Butterworth-Heinemann, 2012.
- [6] M Werling, J Ziegler, S Kammel, et al. Optimal trajectory generation for dynamic street scenarios in a Frenet frame. *IEEE International Conference on Robotics and Automation*, 2010: 987–993.
- [7] J Ziegler, P Bender, T Dang, et al. Trajectory planning for Bertha—A local, continuous method. *IEEE Intelligent Vehicles Symposium*, 2014: 450–457.
- [8] W Chen, J Hu, M Tomizuka. Adaptive Frenet-frame trajectory tracking control for autonomous vehicles with time-varying longitudinal velocity. *Vehicle System Dynamics*, 2023, 61(2): 241–259.
- [9] X Li, Z Sun, D Chu, et al. Deep reinforcement learning for autonomous vehicle trajectory tracking: A coupled longitudinal-lateral perspective. *IEEE Transactions on Intelligent Transportation Systems*, 2022, 23(9): 14368–14381.
- [10] R Verschueren, G Frison, D Kouzoupis, et al. acados—A modular open-source framework for fast embedded optimal control. *Mathematical Programming Computation*, 2022, 14(1): 147–183.
- [11] M Falcone, F Borrelli, J Asgari, et al. Predictive active steering control for autonomous vehicle systems. *IEEE Transactions on Control Systems Technology*, 2007, 15(3): 566–580.
- [12] J Backman, T Oksanen, A Visala. Navigation system for agricultural machines: Nonlinear model predictive path tracking. *Computers and Electronics in Agriculture*, 2012, 82: 32–43.
- [13] J Kong, M Pfeiffer, G Schildbach, et al. Kinematic and dynamic vehicle models for autonomous driving control design. *IEEE Intelligent Vehicles Symposium*, 2015: 1094–1099.
- [14] SAE International. *Taxonomy and definitions for terms related to driving automation systems for on-road motor vehicles: J3016_202104*. Warrendale: SAE International, 2021.

INTERNAL HEAT AND MASS TRANSFER MECHANISM OF SOLAR CPC CONCENTRATOR ADSORBER BASED ON CFD SIMULATION

YuDong Li*, HaiPeng Sun, XiuJuan Chen

New Energy Engineering, Weifang Institute of Technology, Qingzhou 262500, Shandong, China.

Corresponding Author: Yudong Li, Email: yd2248782575@163.com

Abstract: With the global energy crisis and increasingly serious environmental problems, solar adsorption refrigeration system has been widely concerned because of its environmental protection characteristics and advantages of using renewable energy. In this paper, a new type of solar CPC adsorption refrigeration system is designed. By establishing the CFD model of the adsorption bed and using the finite control volume method, the heat transfer characteristics of the refrigerant in the desorption process of the adsorption bed are simulated and calculated, and the flow characteristics of the refrigerant in the adsorption bed and its influence on the surrounding wall are analyzed according to the changes of the temperature, phase and flow rate of the refrigerant. The results show that the refrigerant near the outlet of the adsorption bed is more likely to absorb heat and desorb. The average velocity of mixed-phase refrigerant is around 1m/s at the transverse section of the pipeline, and the temperature near the wall in the adsorption pipe can reach 360K. In the longitudinal direction, the velocity near the outlet pipeline is faster, and a small area of turbulence appears at the upper side.

Keywords: Solar CPC; Adsorbent bed; Desorption process; Numerical simulation

1 INTRODUCTION

The effective use of solar energy resources to cope with global climate change, coordinate and realize human sustainable development has gradually become an increasingly important issue for human beings. Different from traditional compression refrigeration, solar adsorption refrigeration can effectively utilize solar radiation, without using HCFC and HFC refrigerants, without CFCs and greenhouse effect, and is more friendly to the environment. Adsorption bed is the core component of adsorption refrigeration and an indispensable part of physical processes such as adsorption and desorption of refrigerant. Its heat and mass transfer performance will determine the performance of the whole system. The adsorption bed is filled with adsorption working pairs (mainly zeolite-water, silica gel-water, activated carbon methyl alcohol, calcium chloride-water, etc.) in a certain shape of the shell, and the granular packed adsorption bed, that is, the characteristics of porous media, cause problems such as slow heat transfer process and long periodicity [1].

The traditional solar energy collection system will lose the solar radiation energy passing through the interlayer due to the vacuum interlayer, and it cannot be absorbed by the selective absorption coating in the pipe. The performance improvement of solar adsorption refrigeration is mainly through adopting different enhanced mass transfer to improve refrigeration efficiency. Some scholars have added fins to enhance heat transfer inside the adsorption bed or adopted a double-bed solar adsorption model. Although double-bed solar adsorption refrigeration effectively solves the problems of discontinuous refrigeration process, low power and long cycle, there are some problems such as unstable heat source and energy waste [2].

In this paper, a "light-heat-cooling" comprehensive energy-saving refrigeration system based on solar CPC concentrating adsorber with silica gel-water as working pair is established, and the heat and mass transfer characteristics of adsorption bed are studied by computational fluid dynamics. Through numerical analysis of the interaction of fluids and the variation of temperature field in the process of heat transfer, some theoretical basis is provided for the optimization of solar refrigeration.

2 DESIGN OF SOLAR CPC ADSORPTION REFRIGERATION SYSTEM

Combining concentrated photovoltaic with adsorption refrigeration technology can improve the efficiency and form a combined cooling and heating system, which is of great significance to alleviate energy shortage and reduce energy consumption [3-5]. Traditional solar adsorption refrigeration mostly depends on the pressure difference in the system, which belongs to natural mass transfer characteristics [6]. The circulation of high temperature and high pressure refrigerant desorbed from the adsorption bed in the mass transfer pipeline is mainly self-diffusion, and some scholars have made many contributions to the heat transfer enhancement of the adsorption bed [7]. In this paper, the heat transfer performance of the adsorption bed is numerically simulated with silica gel-water as the adsorption working medium. The filling height of the adsorption material is in the range of 70-100mm, and the overall design size of the adsorption bed should not be too large. In order to improve the heat and mass transfer performance of the adsorption bed and

reduce the heat and heat resistance of the adsorption bed, the size of the adsorption bed should be reduced as small as possible [8].

The size of the adsorption bed used in this simulation is shown in Figure 1, with a length of 1150mm and a width of 1150 mm. The single mass transfer pipeline is filled with the space in a circular tube with a diameter of 47-94mm, and the filling length is 1050 mm. The filling material is C-type silica gel, which is easy to form a composite working medium with CaCl_2 , and its performance is better [9-10]. See Table 1 for its main physical parameters. The heat source is mainly provided by CPC concentrator using solar radiation energy, and can be supplemented by hot water system when the solar illumination is insufficient.

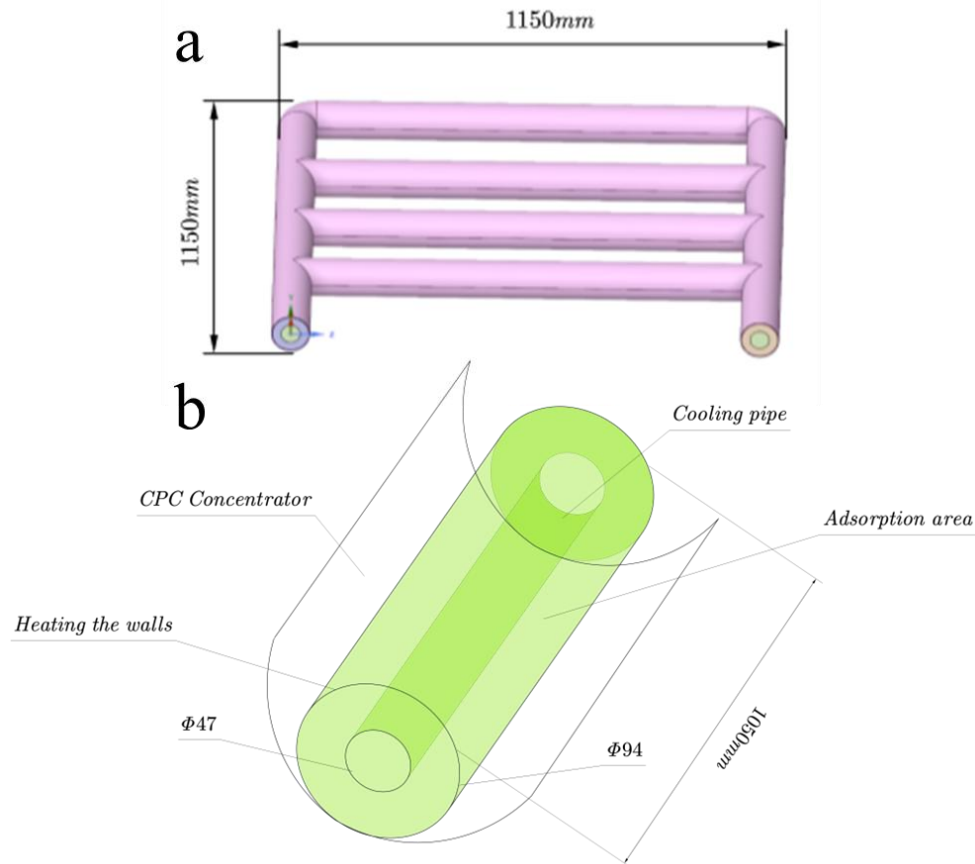
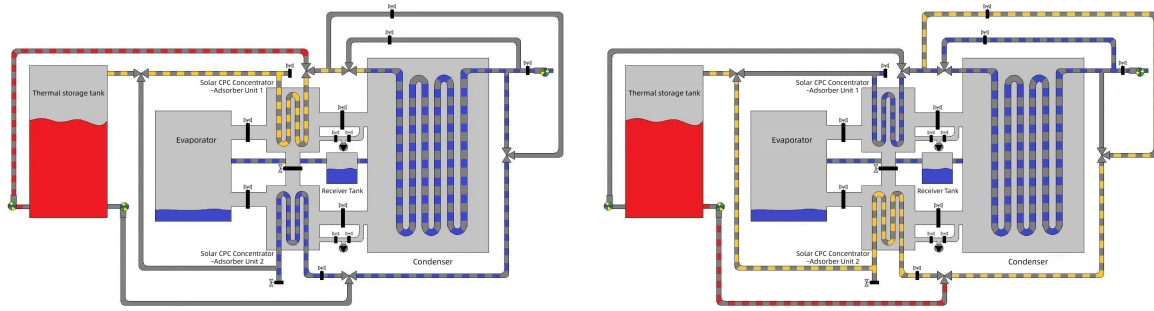


Figure 1 Three-Dimensional Effect Diagram of Adsorption Bed

(a) Schematic Diagram of Adsorption Bed; (b) Schematic diagram of a single adsorption tube

This project designs a refrigeration system based on solar CPC concentrator, which mainly includes two solar CPC concentrator, evaporator, condenser, air cooler, liquid storage tank, heat preservation water tank and micro vacuum pump. Two solar CPC condensing adsorbers work alternately, which can realize continuous cooling of the system during the day, and the supporting heat preservation water tank can store solar heat, which can provide heat for the system to work at night, thus realizing all-weather cooling of the system. Silica gel- CaCl_2 composite adsorbent is used in solar CPC concentrator, which can improve the adsorption capacity and capacity of the system and increase the refrigeration capacity of the system. At the same time, the system combines the dual operation strategy of natural-enhanced mass transfer, simplifies the system structure by adding some pipelines and equipment, effectively avoids the desorption of gas by low-temperature active adsorbent, and avoids the inevitable intermittent refrigeration problem in natural mass transfer mode. This system makes full use of solar energy through the compound parabolic concentrator, and combines with the compound adsorption mode to realize the effective utilization of low-grade energy, reduce the power consumption, relieve the power shortage, and has the dual functions of saving the environment.



(a) Desorption by adsorption bed 1 and adsorption by adsorption bed 2 (b) Desorption by adsorption bed 2 and adsorption by adsorption bed 1

Figure 2 Schematic Diagram of Adsorption and Desorption in Adsorption Bed

When one adsorption bed is heated for desorption, cooling water is introduced into the other adsorption bed to reduce the temperature for adsorption, and the heat source is directly supplied by solar energy. When rainy weather or night occurs, hot water in the heat preservation water tank provides heat for desorption, and a micro vacuum pump is installed in a pipeline between the condenser and the adsorption bed in parallel, so as to avoid reverse adsorption due to insufficient temperature, and at the same time, the mass transfer process can be enhanced and the refrigeration capacity can be increased. The inevitable intermittent refrigeration problem in the natural mass transfer mode is solved. During the alternation of two adsorption beds, the heat of the condenser is taken away by cooling water to preheat the adsorption beds, so that the working state can be switched faster and the energy utilization rate can be improved. The adsorption and desorption process of adsorption bed is shown in Figure 2 and Table 1.

Table 1 Various Performance Parameters of C-Type Silica Gel Selected in this Paper

grain size	specific surface area	Kong Rong	specific heat	Thermal conductivity	stacking density	True density
<i>mm</i>	<i>m²/g</i>	<i>ml/g</i>	<i>KJ/(kg·K)</i>	<i>W/(m·K)</i>	<i>kg/m³</i>	<i>kg/m³</i>
0.6-1.5	700-800	0.40-0.50	0.92	0.175	750	2100

3 NUMERICAL MOFRL AND BOUNDARY CONDITIONS

Under the condition of sunlight, it is assumed that the intensity of solar radiation received by the outer wall of the CPC concentrating adsorption tube is uniform, and the outer wall of the adsorption tube is heated by a heat flow of 800W/m² [6]. The particles of adsorption working medium filled in the adsorption bed are evenly distributed, and there is no air thermal resistance between the particles, and the other walls are insulated.

3.1 Basic Conditions of Model

Here, the fractional equation, momentum calculation, energy conservation and mass conservation of fluid will be introduced respectively. Regarding the fluid volume fraction, implicit formula is used here in this study, and the volume fraction equation is discretized as follows:

$$\frac{a_q^{n+1} \rho_q^{n+1} - a_q^n \rho_q^n}{\Delta t} V + \sum_f (\rho_q^{n+1} U_f^{n+1} a_{qf}^{n+1}) = [S_{a_q} + \sum_{p=1}^n (\dot{m}_{pq} - \dot{m}_{qp})] V \quad (1)$$

Where $n + 1 =$ Current index time step; $n =$ The index of the previous time step; $a_q^{n+1} =$ Step $n+1$ of unit volume value of current volume fraction; $a_q^n =$ Unit volume value of volume fraction at current step n ; $a_{qf}^{n+1} =$ Volume fraction of face value in time step $n + 1q^{th}$; $U_f^{n+1} =$ The volume flux through the face is at time step $n+1$; $V =$ Unit volume.

In the aspect of momentum calculation, a single momentum equation is solved in the whole domain, and the generated velocity field is shared among all phases, and the momentum equation depends on the ergodic property sum of all stages.

$$\frac{\partial}{\partial t} (\rho \vec{v}) + \nabla \cdot (\rho \vec{v} \vec{v}) = -\nabla p + \nabla \cdot [\mu (\nabla \vec{v} + \nabla \vec{v}^T)] + \rho \vec{g} + \vec{F} \quad (2)$$

The energy equation is satisfied in the process of interaction between phases:

$$\frac{\partial (\rho E)}{\partial t} + \nabla \cdot [\vec{v} (\rho E + p)] = \nabla \cdot \left[k_{eff} \nabla T - \sum_q \sum_j h_{jq} \vec{J}_{jA} + (\vec{\tau}_{eff} \cdot \vec{v}) \right] + S_h \quad (3)$$

It is difficult to calculate the mass of a single phase when calculating the overall mass, so the average method is used to calculate the average mass variable instead of calculating the mass of a single phase.

$$E = \frac{\sum_{q=1}^n \alpha_q \rho_q E_q}{\sum_{q=1}^n a_q \rho_q} \quad (4)$$

$$E_q = h_q - \frac{p}{\rho_q} + \frac{v^2}{2} \quad (5)$$

The porous medium model is to add momentum source to the standard momentum equation, and the obstacles to the velocity are not expressed in the model. The velocity calculated in this area is the apparent velocity, and the porous medium area is regarded as completely open. The correlation coefficient is defined based on this assumption. For the calculation of porosity, using C-type silica gel (easy to compound with CaCl₂ _ 2, etc. to form a better composite silica gel), the bulk density =400g/L and the real density = 1.12 g/cm, the porosity is:

$$\varepsilon = 1 - \frac{\rho_b}{\rho_p} = 0.67 \quad (6)$$

Among them, the resistance source term f in the momentum equation is:

$$F = - \left(\sum_{j=1}^3 D_{ij} \mu v_j + \sum_{j=1}^3 C_{ij} \frac{1}{2} \rho |v| v_j \right) \quad (7)$$

Sticky term: $\sum_{j=1}^3 D_{ij} \mu v_j ;$

Inertia term: $\sum_{j=1}^3 C_{ij} \frac{1}{2} \rho |v| v_j ;$

$$\frac{\Delta P}{L} = \frac{150 \mu (1 - \varepsilon)^2}{D_p^2 \varepsilon^3} v + \frac{1.75 \rho (1 - \varepsilon)}{D_p \varepsilon^3} v^2 \quad (8)$$

ErgunEquation is used to deduce the input of porous media:

Viscous resistance coefficient: $D_{ij} = \frac{1}{\alpha} = \frac{150 (1 - \varepsilon)^2}{D_p^2 \varepsilon^3}$

Inertia resistance coefficient: $C_{ij} = C_2 = \frac{3.5 (1 - \varepsilon)}{D_p \varepsilon^3}$ (Equivalent Sphere Diameter)

3.2 Boundary Conditions and Initial Conditions

In the adsorption process, the heating wall is used to exchange heat with the adsorbent, and the other walls are set as adiabatic walls. The solid material is copper, and the heat transfer fluid medium is steady incompressible water, and its physical parameters are constant at the equivalent temperature. The inlet of heat transfer fluid adopts velocity boundary condition and the outlet adopts pressure boundary condition. Coupled heat transfer calculation is used for internal measurement pipeline and wall.

Initial conditions for heating wall temperature of adsorption bed:

$$T(x, y, z)|_{t=0} = 348K \quad (9)$$

Initial conditions for calculating regional pressure:

$$P_b(x, y, z)|_{t=0} = 0Pa \quad (10)$$

4 ANALYSIS OF CALCULATION RESULTS

In the model, the initial time step is set to 1e-5s, and the Adaptive type and Multiphase-Specific method are selected. When the step is 83000, the flow is stable, and the parameter characteristics at this moment are selected.

4.1 Transverse Characteristics of Refrigerant

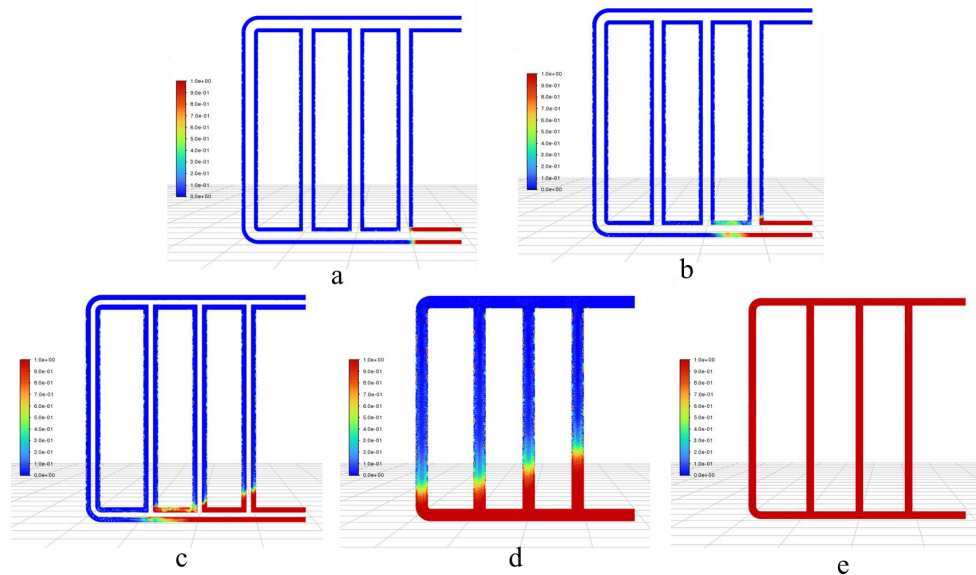


Figure 3 Steam distribution

In the model, the Y-axis is 0mm as the datum, and five positions are taken at intervals of 10mm upward. Figure 3 reflects the distribution of refrigerant vapor during desorption at this time. In the adsorption area, due to the poor thermal conductivity of the adsorbed working medium, the working medium in the upper position is more likely to absorb heat and desorb during heating. Compared with the inlet position, the working medium in the pipeline near the outlet is more likely to absorb heat and evaporate, and at the same time, the refrigerant vapor is generated near the wall and gradually converges to the outlet pipeline by small bubbles.

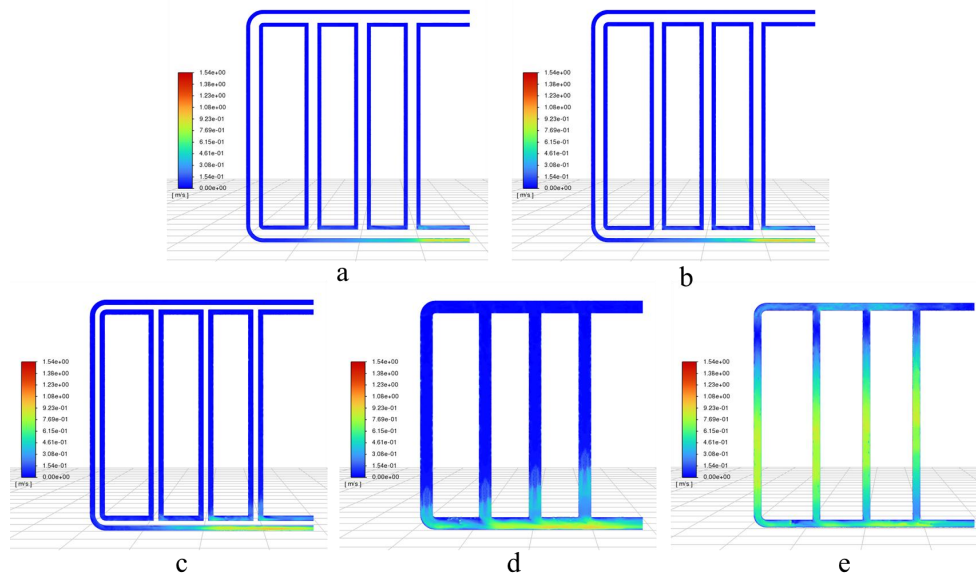


Figure 4 Velocity Distribution of Mixed Phase

Figure 4 shows the velocity distribution of two-phase mixture of refrigerant. The flow characteristics of working medium are consistent with the distribution of steam state. The more intense the desorption of working medium is, the faster the flow rate of steam is compared with other positions. At the upper position of the pipeline in the adsorption area, the working fluid velocity is closer to the inlet of the pipeline than the outer pipeline, which may be caused by the pressure difference. The maximum velocity of the mixed phase can reach 1.54m/s, and the average velocity is around 1 m/s.

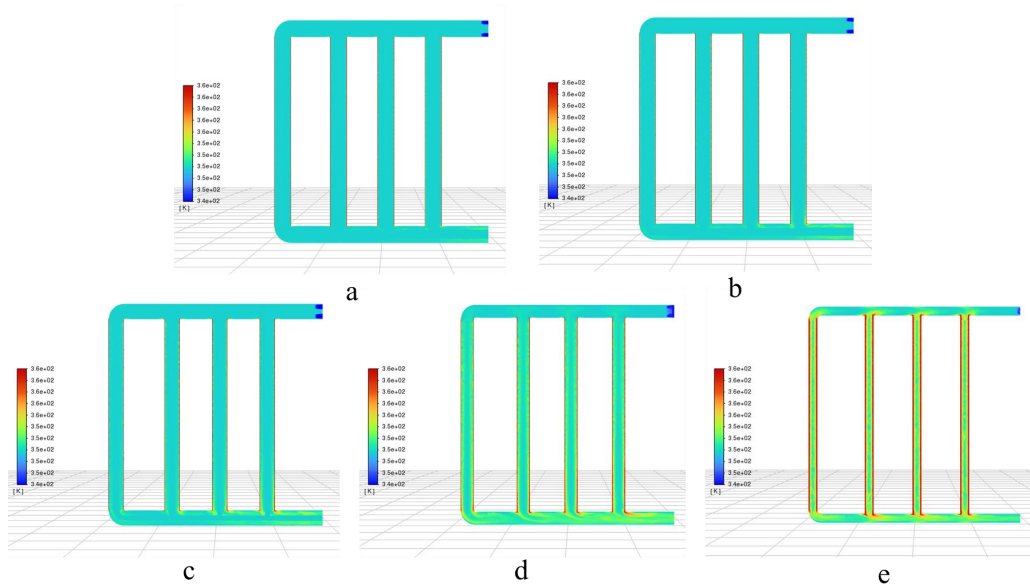


Figure 5 Mixed Phase Temperature Distribution

Figure 5 shows the temperature distribution of the mixed phase in the mass transfer pipeline. Because of the low thermal conductivity of the material, the desorption process of refrigeration wages mostly occurs near the upper wall of the pipeline. How to increase the heat transfer effect and enhance the thermal conductivity of the material is also the main research direction at present. It is worth noting that when the position is in the middle and upper part of the adsorption bed, the temperature near the second tube wall intersects with other tube walls higher, which may be caused by the flow of working fluid in the tube, that is, the change of pressure in the surrounding tube enhances the disturbance of fluid in the middle tube, and then enhances the heat transfer effect.

4.2 Longitudinal Characteristics of Refrigerant

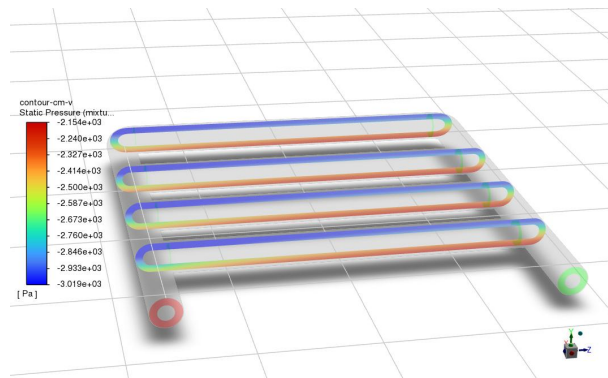


Figure 6 Pressure Distribution

Based on the center of each pipeline, four positions are separated. Figure 6 shows that the pressure distribution of the longitudinal mass transfer pipeline is high in the lower side and low in the upper side, and the side with higher pressure closer to the Z axis is more inclined to the entrance. Therefore, when optimizing the characteristics of the adsorption bed, it is considered to design the pipeline materials in different regions to save costs.

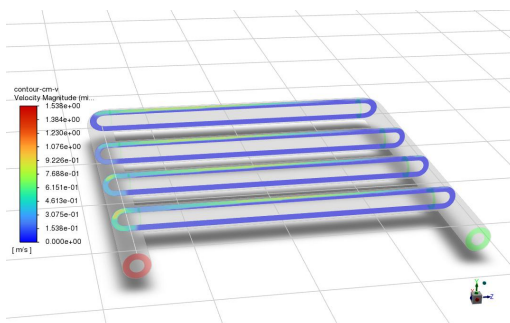


Figure 7 Velocity Distribution

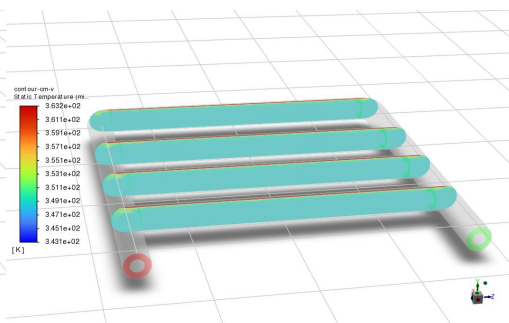


Figure 8 Temperature Distribution

Figure 7 and Figure 8 respectively show the velocity and temperature of the mixed phase in the mass transfer pipeline in the longitudinal direction. The velocity in the middle of the pipeline is higher at the upper side, and the velocity near the left wall of the outlet pipeline is relatively higher, which is due to the change of fluid velocity caused by the shape of the pipeline, and the longitudinal temperature distribution in each pipeline is similar, which is mainly heat transfer at the upper side. When making pipeline materials, the influence of material deformation on the upper and lower surfaces due to different heating should be considered.

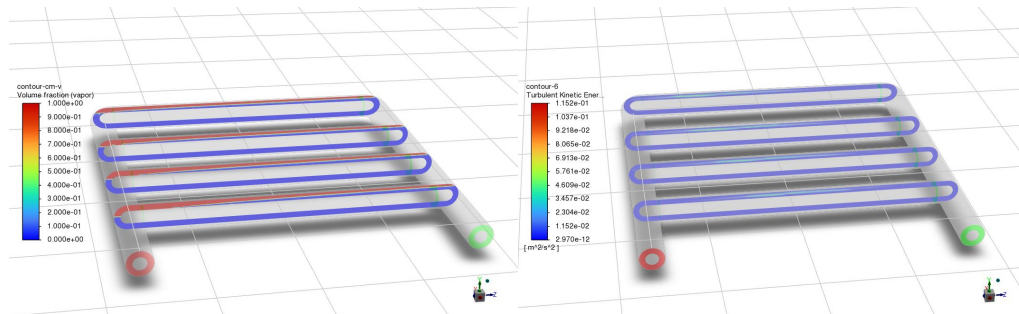


Figure 9 Steam Distribution

Figure 10 Turbulence Situation

Figure 9 shows the distribution of refrigerant vapor in the longitudinal direction, and fig. 10 shows the turbulent distribution in the longitudinal direction. In the longitudinal position of the middle pipeline, the desorption of refrigerant on the upper side of each pipeline is almost the same, but there is a small area of turbulence in the middle part. The turbulence in the pipeline closer to the inner side is closer to the middle of the pipeline, and this position is affected by the pressure in the whole area. When considering the size of the adsorption bed and the number of mass transfer pipelines, it should be selected by measuring the change of pressure in the pipeline to enhance efficiency.

5 CONCLUSION

During the operation of the system, in the transverse direction, the refrigerant near the outlet of the adsorption bed is more likely to absorb heat and desorb, and at the same time, under the action of pressure difference, the maximum flow rate of the refrigerant is closer to the outlet pipeline when it goes to the outside, while the temperature distribution is higher when it is close to the upper side of the pipeline. In the longitudinal direction, the pressure in the pipeline is in a state of low and high, which is beneficial to the flow of refrigeration steam, while the velocity is higher at the outer side wall of the outlet pipeline. The desorption rate of longitudinal refrigerant in each pipeline is almost the same, and turbulence appears in the middle of the pipeline. Due to the influence of pressure, the turbulence position of the outer pipeline is close to the outlet pipeline.

Based on computational fluid dynamics, supplemented by CFD, this paper provides an idea and framework for studying the change process of characteristic parameters of solar adsorption refrigeration during operation, and how to choose a suitable plane to show the change process. By showing the system designed in this paper, it proves the feasibility of applying this idea to explore the process of solar adsorption refrigeration. On this basis, the follow-up research on the operating characteristics of adsorption refrigeration system can be carried out in this way, and other refrigeration methods can also follow this method to understand the internal characteristics of the system, providing a basis for the real construction of the system.

COMPETING INTERESTS

The authors have no relevant financial or non-financial interests to disclose.

FUNDING

This work was funded by the project of Shandong University Students' Innovation and Entrepreneurship Training Plan in 2024 (Design of Integrated Energy-saving Refrigeration System with Light, Heat and Cooling for Multi-purpose Water), Project number S202413379002.

REFERENCES

- [1] Duan Pengfei, Gü tter, Chen Fei, et al. Study on the shape model of circular absorber compound parabolic concentrator and its simulation verification. *Acta Optica Sinica*, 2017, 37(06): 211-219.
- [2] Zhang Ci-zhi, Lu Guan-li. Analysis on the design of condensing continuous high-efficiency intelligent adsorption air conditioner and its enhanced heat transfer. *Energy and Environment*, 2019(01): 55-56.
- [3] Hu Wei, Zhao Yue. Study on optimization of adsorption bed structure of silica gel-water adsorption refrigeration system. *Science and Technology Innovation*, 2021(02): 1-8.

- [4] Peng Jiajie, Pan Quanwen, Ge Tianshu, et al. Performance test of adsorption combined cooling and heating system driven by solar energy. *Journal of Shanghai Jiaotong University*, 2020, 54(07): 661-667.
- [5] Li Qiwei, He Zhaohong, Li Jun, et al. Research progress on reducing the temperature of driving heat source of adsorption refrigeration system. *New Energy Progress*, 2021, 9(05): 368-378.
- [6] Zhao Wenkui, Wang Yunfeng, Zhao Chong, et al. Optimization of operation strategy for enhancing mass transfer of solar adsorption refrigerator. *Journal of Yunnan Normal University (Natural Science Edition)*, 2020, 40(04): 6-10.
- [7] Zhang Pin, Duan Huanhuan, Liu Qunsheng, et al. Research status of heat and mass transfer enhancement of adsorption bed in adsorption refrigeration system. *Refrigeration Technology*, 2021, 41(03): 12- 17+ 36.
- [8] Zhao Chong. Study on the performance of adsorption refrigeration system based on solar energy concentrated heat transfer and enhanced mass transfer mode. Yunnan Normal University, 2020.
- [9] Zepeng Wang, Yuan Zhongxian, Wang Jie, et al. Effect of silica gel particle size on the performance of solar adsorption refrigeration system. *Progress in Chemical Industry*, 2022, 41(07): 3545-3552.
- [10] Liu Yan, Ma Chunyuan, Meng Zhang. Research status and development prospect of solar adsorption refrigeration system. *Solar Energy*, 2018(07): 5- 9+ 26.

LEAST SQUARES AND CLUSTER ANALYSIS BASED METHODOLOGY FOR SONIC BOOM LOCALIZATION OF ROCKET DEBRIS

XianYang Zhou^{1*}, WeiRong Zhang², SiQi Ji¹, Yang Song¹

¹College of Arts and Sciences, Northeast Agricultural University, Harbin 150030, Heilongjiang, China.

²Guiyang No. 25 High School, Guiyang 550025, Guizhou, China.

Corresponding Author: XianYang Zhou, Email: xianyangzhou1799@163.com

Abstract: Aiming at the transonic sonic boom localization problem generated by the falling rocket debris, this paper proposes a spatio-temporal localization method of debris based on acoustic monitoring. The sonic boom signal is received by multiple monitoring devices, and the effects of time error and equipment layout on positioning accuracy are analyzed to construct a single target and multi-target cooperative positioning model. For single wreckage, the four-sphere intersection principle and the least-squares method with error compensation are adopted to realize the accurate solution of three-dimensional coordinates and sonic boom moment through four monitoring devices, and the localization results are 110.57° longitude, 27.16° latitude, 957.96 m elevation, and 100.753 s. For multi-wreckage scenarios, the classification model of vibration wave signals is proposed, and the classification model of vibration wave signals is proposed by combining the Pearson correlation coefficient and the K-means clustering algorithm. A vibration wave signal classification model is proposed, and a time difference threshold constraint (≤ 5 s) is introduced to optimize the wreckage matching, which effectively solves the problem of overlapping multi-source sonic boom signals. The results of this paper show that the proposed method significantly improves the robustness and accuracy of rocket debris localization in complex scenes, and can provide theoretical support for the rapid confirmation of the drop point.

Keywords: Rocket debris; Transonic sonic boom; Error compensation; Least squares; K-means

1 INTRODUCTION

Traditional methods for localizing rocket debris mainly rely on radar or visual monitoring, and these methods have problems such as limited accuracy and susceptibility to interference in complex environments. Especially in the crash area with complex terrain and variable environment, the traditional methods have limited localization effect. As a non-contact localization means[1], acoustic monitoring has gradually become a research hotspot in the field of rocket debris localization due to its advantages such as less influence by environmental factors and wide coverage.

In recent years, the localization technology based on acoustic monitoring has made significant progress in several fields[2]. For example, in the field of indoor localization, ultra-wideband (UWB) technology has realized the precise positioning of target objects by virtue of its high accuracy and strong anti-interference ability[3]. In addition, sound source localization technology based on microphone arrays has been widely used in the fields of robot auditory perception and speech recognition. The successful application of these technologies provides valuable reference and lessons for the sonic localization of rocket debris[4].

However, the sonic boom localization problem of rocket wreckage has its special characteristics [5]. The high intensity and short duration characteristics of the sonic boom signal, as well as the complex aerodynamic and thermodynamic effects during the falling process, all increase the difficulty of localization. To address the above problems, this paper proposes a spatio-temporal localization method for rocket debris based on sonic monitoring[6]. The method receives sonic boom signals through multiple monitoring devices, analyzes the influence of time error and equipment layout on positioning accuracy, and constructs a single target and multi-target cooperative positioning model. For single wreckage, the four-sphere intersection principle and the least squares method with error compensation are adopted to realize the accurate solution of 3D coordinates and sonic boom moments. For multi-wreckage scenarios, combining Pearson correlation coefficient and K-means clustering algorithm[7], the vibration wave signal classification model is proposed, and the time difference threshold constraint is introduced to optimize the wreckage matching, which effectively solves the problem of overlapping of multi-source sonic boom signals[8]. The experimental results show that the method significantly improves the robustness and accuracy of rocket debris localization in complex scenes, and provides theoretical support for the rapid confirmation of the drop point[9].

The research in this paper not only provides technical support for the safe recovery of rocket debris, but also opens up new ideas for the application of acoustic positioning technology in aerospace field.

2 SINGLE WRECKAGE LOCALIZATION MODEL BASED ON FOUR-SPHERE INTERSECTION WITH DYNAMIC ERROR COMPENSATION

2.1 Equipment coordinate normalization and four-sphere intersection principle

2.1.1 Normalization of device coordinates

Firstly, the geographic coordinates (longitude, latitude and elevation) of the monitoring equipment are converted into units in meters, and since the distance value per latitude is approximated to be 111.263 km, and the distance value per longitude is approximated to be 97.304 km, the following conversions can be performed, and the locations of the seven testing equipment in the Cartesian coordinate system are shown in Table 1:

$$\begin{cases} x_i = x \times 97304(\text{meter}) \\ y_i = y \times 111263(\text{meter}) \\ z_i = z(\text{meter}) \end{cases} \quad (1)$$

(x_i, y_i, z_i) ($i = 1, 2, \dots, 7$) denotes the positional coordinates of the seven monitoring devices A to G.

Table 1 Three-dimensional Coordinates after Conversion

Equipment	Longitude (m)	Latitude (m)	Elevation (m)
A	9370485	2992440	824
B	9416300	3020160	727
C	9410520	3056350	742
D	9371335	3060750	850
E	9394540	3037870	786
F	9389695	3071310	678
G	9353995	2983310	575

2.1.2 Four-sphere intersection localization (math.)

In this paper, the sonic boom arrival time is used to construct a time difference for multistation passive localization[10], and since acoustic waves propagate at a constant velocity in the air, the relationship between the arrival time and the speed of sound can be utilized to calculate the distance from the detection equipment to the rocket wreckage.

Assuming that the start time of the sonic boom in the wreckage is t_0 , and the time for the sonic boom to reach each piece of equipment is t_i ($i = 1, 2, 3, \dots, 7$), then the time required for the sonic boom to be transmitted is $(t_i - t_0)$. It is known that the velocity of propagation of the vibration wave is $v = 340$ m/s, and the distance between the wreckage and each piece of equipment is:

$$d_i = v \cdot (t_i - t_0) \quad (2)$$

Assuming that the 3D coordinates of the wreckage when the sonic boom occurs are (x, y, z) and the 3D coordinates of the monitoring equipment are (x_i, y_i, z_i) , the true distance between the monitoring equipment and the wreckage can be expressed as:

$$D_i = \sqrt{(x_i - x)^2 + (y_i - y)^2 + (z_i - z)^2} \quad (3)$$

Neglecting a number of error factors such as ground curvature, time errors, etc., the following equation should hold:

$$\sqrt{(x_i - x)^2 + (y_i - y)^2 + (z_i - z)^2} = v \cdot (t_i - t_0) \quad (4)$$

Three balls in three-dimensional space should intersect at two points, but due to the wreckage of the beginning of the sonic boom time is also unknown, it is still necessary to solve an equation, then at least four monitoring devices need to be arranged to accurately locate the wreckage to each detection device as the center of the sphere, the four spheres of the intersection as shown in Figure 1.

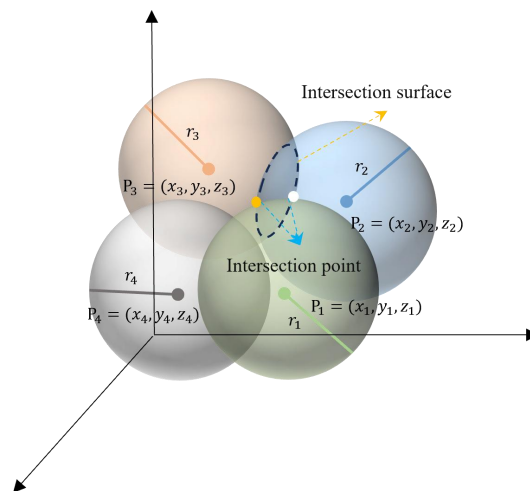


Figure 1 Four-sphere Intersection

That is, the program consists of one sonic boom signal source and four ground monitoring devices, as shown in Figure 2. The principle of localization is to record the moment when the sonic boom signal source and each monitoring station

receives the radiation source signal[11], and calculate the time difference between the received localization signals, so as to solve the position of the target.

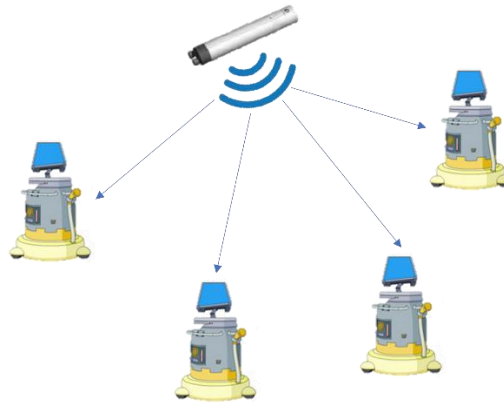


Figure 2 Sonic Boom Signal Propagation

The equations for passive localization can be listed as Equation 5, and by solving the joint equations by association the positional coordinates of the bomb and arrow wreckage segments can be calculated.

$$\begin{cases} \sqrt{(x_1 - x)^2 + (y_1 - y)^2 + (z_1 - z)^2} = v \cdot (t_1 - t_0) \\ \sqrt{(x_2 - x)^2 + (y_2 - y)^2 + (z_2 - z)^2} = v \cdot (t_2 - t_0) \\ \sqrt{(x_3 - x)^2 + (y_3 - y)^2 + (z_3 - z)^2} = v \cdot (t_3 - t_0) \\ \sqrt{(x_4 - x)^2 + (y_4 - y)^2 + (z_4 - z)^2} = v \cdot (t_4 - t_0) \end{cases} \quad (5)$$

2.2 Least Squares Optimization Algorithm with Error Factors

However, in reality, the signal propagation environment is not ideal, and various influencing factors interfere with the propagated signal, resulting in a positive error in the measured value of the sonic boom's arrival time or arrival time difference, thus making the equation unsolved. Because the measurement error is usually linear with the measurement distance increases the pattern of growth, so here to introduce an error factor β ($0 \leq \beta \leq 1$). Then the actual distance between the monitoring equipment and the wreckage can be expressed as.

$$D_i = \beta \cdot d_i \quad (6)$$

Then Equation 5 can be transformed into:

$$\begin{cases} \beta^2 d_1^2 = (x_1 - x)^2 + (y_1 - y)^2 + (z_1 - z)^2 \\ \beta^2 d_2^2 = (x_2 - x)^2 + (y_2 - y)^2 + (z_2 - z)^2 \\ \vdots \\ \beta^2 d_i^2 = (x_i - x)^2 + (y_i - y)^2 + (z_i - z)^2 \end{cases} \quad (7)$$

Let the distance from the monitoring equipment to the wreckage be: $k_i = x_i^2 + y_i^2 + z_i^2$ and, at the same time, transform equation (7):

$$\begin{cases} \beta^2(d_1^2 - d_2^2) + 2(x_1 - x_2)x + 2(y_1 - y_2)y + 2(z_1 - z_2)z = K_1 - K_2 \\ \beta^2(d_1^2 - d_3^2) + 2(x_1 - x_3)x + 2(y_1 - y_3)y + 2(z_1 - z_3)z = K_1 - K_3 \\ \vdots \\ \beta^2(d_1^2 - d_i^2) + 2(x_1 - x_i)x + 2(y_1 - y_i)y + 2(z_1 - z_i)z = K_1 - K_i \end{cases} \quad (8)$$

It is further rewritten in least squares matrix form:

$$AX = b \quad (9)$$

where $b = \begin{bmatrix} K_1 - K_2 \\ K_1 - K_3 \\ \vdots \\ K_1 - K_i \end{bmatrix}$, $A = \begin{bmatrix} (d_1^2 - d_2^2) & 2(x_1 - x_2) & 2(y_1 - y_2) & 2(z_1 - z_2) \\ (d_1^2 - d_3^2) & 2(x_1 - x_3) & 2(y_1 - y_3) & 2(z_1 - z_3) \\ \vdots & \vdots & \vdots & \vdots \\ (d_1^2 - d_i^2) & 2(x_1 - x_i) & 2(y_1 - y_i) & 2(z_1 - z_i) \end{bmatrix}$

where β^2 is the squared value of the measurement error factor, $X = (\beta^2, x, y, z)$ is the vector representation of all unknown quantities, and where (x, y, z) is the 3D coordinates of the rocket wreckage. Therefore the final solution value can be obtained using the least squares algorithm as:

$$X = (A^T A)^{-1} A^T b \quad (10)$$

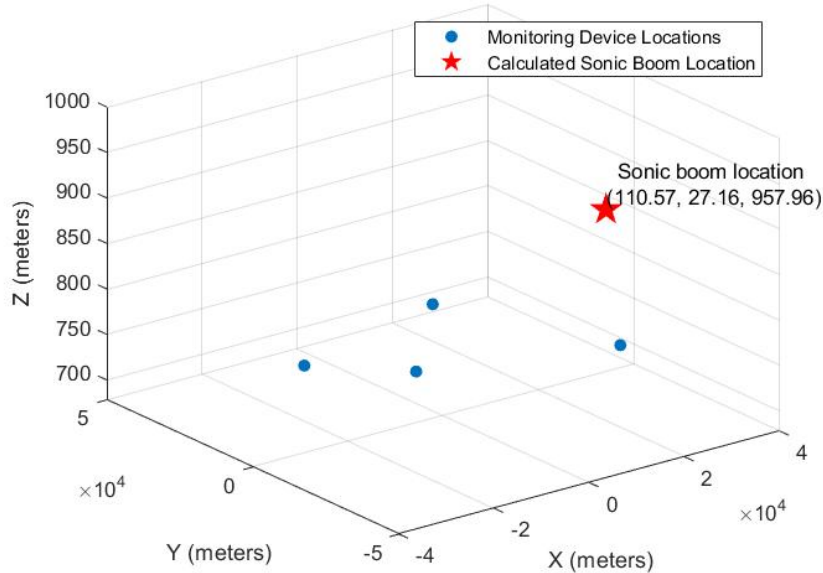
2.3 Single Wreck Localization Results and Error Analysis

In this paper, the least squares algorithm with error factor is used for the solution[12]. The error analysis of the proposed method is performed using data, the test data has a total of 1 wreck and 7 monitoring devices, and the arrival time of the signal received corresponding to each device, the results are shown in Table 2:

Table 2 Positioning Results

Parameters	X(latitude)	Y(longitude)	Z(elevation)	T(seconds)
numerical value	110.57	27.16	957.96	100.753

This paper finally obtained the sonic boom point longitude 110.57 ° , latitude 27.16 ° , altitude 957.96m, sonic boom moment for 100.753 s. In order to more intuitively show the best monitoring equipment and the wreckage of the location of the relationship between the data, plotting the detection of equipment coordinates as shown in Figure 3.

**Figure 3** Monitoring Equipment and Wreckage Coordinates

3 CLUSTER CLASSIFICATION AND CO-LOCALIZATION OF MULTI-WRECK SONIC BOOM SIGNALS

3.1 Vibration Wave Correlation Analysis Based on Pearson's Coefficient

For multiple wreckage sonic boom localization analysis, each monitoring device received four vibration waves in chronological order, but could not identify the corresponding relationship between vibration waves and wreckage.

Due to the differences in the sonic boom time of different wreckage, so the arrival of different detection equipment also has a time difference, but belonging to the same wreckage sonic boom time has a certain correlation, so this paper adopts the correlation analysis[13], through the calculation of the distance between any two monitoring equipment and the sonic boom received the correlation coefficient between the difference in time to make a judgment, if the sonic boom signal comes from the same wreckage, the correlation coefficient is close to 1, and for the different wreckage of the sonic boom signal, the correlation coefficient is very small. If the sonic boom signal comes from the same wreckage, the correlation coefficient will be close to 1, while for different wreckage, the correlation coefficients will be small and not the same, which can be k-mean clustering of vibration waves to identify a group of signals from the same wreckage.[14]

In three-dimensional space, let (x_i, y_i, z_i) be the coordinates of the monitoring device i , (x_j, y_j, z_j) be the coordinates of the monitoring device j , d_{ij} be the distance between the device i and j , Δt_{ij} be the time difference between the reception of the sonic boom of the device i and j , ($i, j = 1, 2, \dots, n, i \neq j$), then the distance and time difference between any two monitoring devices are as follows.

$$d_{ij} = \sqrt{(x_i - x_j)^2 + (y_i - y_j)^2 + (z_i - z_j)^2} \quad (11)$$

$$\Delta t_{ij} = t_i - t_j \quad (12)$$

The arrival time of a sonic boom signal is a continuous value in seconds, and the Pearson correlation coefficient applies to continuous data, reflecting a linear relationship between the variables.

From a physical point of view, the propagation time of sound waves and distance usually follow a linear relationship. As the distance from the source increases, the time of propagation of the sound wave also increases. Since the data is a continuous arrival time of the sonic boom signal, and assuming that there is a linear relationship between time and distance, the Pearson's correlation coefficient can be chosen, which provides a quantitative measure of the strength of the relationship between the variables, and is calculated using the following formula.

$$r = \frac{\sum_{i=1}^n (x_i - \bar{x})(y_i - \bar{y})}{\sqrt{\sum_{i=1}^n (x_i - \bar{x})^2} \sqrt{\sum_{i=1}^n (y_i - \bar{y})^2}} \quad (13)$$

Where $-1 \leq r \leq 1$, the closer r is to 0, the weaker the correlation, the closer it is to 1, the stronger the positive correlation, and the closer it is to -1, the stronger the negative correlation.

3.2 K-means Clustering Optimization Model with Time Constraints

The K-means algorithm is a commonly used iterative, unsupervised clustering algorithm[15], which achieves the division of the samples in the dataset into a predetermined k clusters by minimizing the distance between the samples to make the samples within the same cluster as similar as possible, and as different as possible between the different clusters, and the algorithm is shown in Table 3.

Table 3 Pseudo-code of K-means Algorithm

import	$X = \{x_j\}$ //data set; k //number of clusters
1	for k in max_epochs:
2	$m_1^0, m_2^0 \dots m_k^0$ //Initialize the center of mass
3	for i in k :
4	$d_{ji} = d(x_j, m_i)$ //Calculate distance
5	assign x_j to m_i if $j = \arg \min d_{ji}$ //Assigned to the nearest center of mass
6	$label_{x_j} = j$ //Get Tagged
7	end for
8	for i in k :
9	$m_i = \frac{1}{ S_i } \sum_{x_i \in S_i} x_i$ //Update the center of gravity
10	end for
11	if $ \Delta m_i < \epsilon$
12	end for
13	else:
14	break
15	end for
export	$m_1, m_2 \dots m_k$ //Best Quality Heart; $Y = \{label_{x_j}\}$ //Clustered Tags

After calculating the correlation coefficients between the distances of different monitoring devices and the time difference between the reception of sonic booms, this paper uses the K-means cluster analysis algorithm in machine learning to cluster the correlation coefficients and construct a K-means cluster analysis model to obtain the debris corresponding to the vibration waves received by different monitoring devices[16][17].

The first need for data preprocessing, unified data outline. Assuming that there are m debris in the air, the ground has n monitoring equipment, remember the position coordinates of the i th debris is (x_i, y_i, z_i) , the position coordinates of the j th monitoring equipment is (X_j, Y_j, Z_j) , the moment of receiving the sonic boom signal of the i th debris is $T_{ij}(i = 1, 2 \dots m, j = 1, 2 \dots n)$, where c denotes the speed of propagation of the vibration wave, then there are:

$$\sqrt{(x_i - X_j)^2 + (y_i - Y_j)^2 + (z_i - Z_j)^2} = c(T_{ij} - t_i) \tag{14}$$

Considering that the four wrecks may produce sonic booms at different times, but differ from each other by no more than 5 s, a constraint exists:

$$|t_i - t_j| \leq 5 \tag{15}$$

After adding the constraints, at least $4m$ independent equations are required to determine the location and sonic boom moments of m wrecks. Similarly, similar to the single-wreck sonic boom localization, a system of overdetermined equations can be obtained by listing the corresponding four equations separately for each wreck[18], when the number of monitoring devices $n > 4$. In order to fully utilize the redundant information and improve the localization accuracy, a least squares problem can be constructed:

$$\min_{x_i, y_i, z_i, t_i} \sum_{i=1}^m \sum_{j=1}^n (\sqrt{(x_i - X_j)^2 + (y_i - Y_j)^2 + (z_i - Z_j)^2} - c(T_{ij} - t_i))^2 \tag{16}$$

Therefore, for determining the location and time of the sonic booms of the four wrecks in the air, it is necessary to arrange at least four monitoring devices based on the use of the cluster analysis model and the sonic boom localization model.

3.3 Multi-wreck Localization Equation System Construction and Solution

Taking a given four wrecks as an example, assuming that five monitoring devices are installed on the ground, their locations and the arrival times of the received vibration waves are shown in Table 4:

Table 4 Coordinates of Detection Equipment and Arrival Time of Sonic Booms

Equipment	X(km)	Y(km)	Z(km)	D1(s)	D2(s)	D3(s)	D4(s)
device M	1.0	2.4	0.0	2.0	3.3	4.4	6.6

device N	0.5	0.3	0.0	3.2	4.0	4.9	5.5
device U	3.9	0.4	0.0	2.0	2.6	4.2	8.0
device V	2.0	2.8	0.0	2.5	4.0	5.2	6.9
device W	1.5	2.0	0.0	4.3	5.3	7.0	7.1

Using the least squares model with an error factor, the optimal estimates of the positions and sonic boom moments of the four wrecks were obtained as shown in Table 5 below:

Table 5 Wreckage Coordinates and Sonic Boom Time Estimates

Wreckage	X(km)	Y(km)	Z(km)	sonic boom time(s)
Wreckage 1	-3.36	4.46	5.76	1.44
Wreckage 2	5.45	-3.08	7.83	5.54
Wreckage 3	1.64	3.75	2.56	0.85
Wreckage 4	-2.27	-4.63	7.02	3.38

Comparing and analyzing the localization results with the monitoring data, the error between the theoretical reception time of the vibration wave and the actual time of each monitoring device can be calculated, and the root mean square error is 0.43s. The error is within the allowable range, indicating that the localization results are more accurate and the clustering algorithm and localization model are effective.

For the multi-rocket debris sonic boom localization problem, this paper proposes a method based on least squares estimation and K-means clustering. By establishing a mathematical model for multi-wreckage localization, combined with vibration wave signal identification and clustering analysis, the sonic boom signals of different wreckages are effectively separated and matched. The least squares method is used to optimize and solve the wreckage location and sonic boom moment, and the example validation shows that the method has high accuracy and feasibility. The results show that the method can efficiently deal with the problem of the overlapping of the sonic boom signals from multiple sources, and provides a reliable solution for the localization of the rocket wreckage in complex scenarios. The algorithm can be further optimized in the future to adapt to the dynamic environment requirements.

4 CONCLUSION

Aiming at the complexity of transonic sonic boom localization of rocket wreckage and the problem of multi-source signal aliasing, this paper proposes a spatio-temporal localization method based on acoustic wave monitoring, which significantly improves the localization accuracy and robustness in complex scenes through the single-target and multi-target synergistic localization model.

In single-wreckage localization, the four-sphere intersection principle and the least-squares method with error compensation are used to solve the three-dimensional coordinates of the wreckage and the moment of sonic boom by combining the time difference of the sonic boom signals from the four monitoring devices. By introducing the error factor optimization equation, the measurement error caused by environmental interference is effectively compensated, and high accuracy positioning is finally achieved, and the error analysis shows that the method can significantly reduce the influence of time error and equipment layout on the positioning results.

Aiming at the multi-wreckage scenario, a signal classification model based on Pearson correlation coefficient and K-means clustering is proposed. By calculating the correlation coefficients of time difference and distance of signals received by different monitoring devices, combined with the time difference threshold constraint, the multi-source sonic boom signals are effectively separated. The least squares method is utilized to construct a system of super-definite equations to collaboratively solve the positions and sonic boom moments of multiple wrecks. The validation of the algorithm shows that the root-mean-square error of multi-wreckage localization is 0.43 s. The results are in good agreement with the actual data, which verifies the feasibility and accuracy of the model.

The innovation of this paper is to introduce the error compensation mechanism and cluster analysis into the field of sonic localization, which solves the limitations of traditional methods in complex environments. The research results not only provide reliable theoretical support for the rapid recovery of rocket debris, but also open up a new path for the application of acoustic positioning technology in aerospace engineering. Future research can further optimize the error model and explore the real-time positioning algorithms in dynamic environments to adapt to a wider range of engineering scenarios.

COMPETING INTERESTS

The authors have no relevant financial or non-financial interests to disclose.

REFERENCES

- [1] Wang H. Research on mobile robot sound source localization method based on sound arrival time difference. Qingdao University of Science and Technology, 2020.

- [2] Jin-Hong Xu. Three-dimensional localization method based on optimization principle in non-line-of-sight propagation environment. Zhejiang Gongshang University, 2018.
- [3] Wang J T, Huang F Y, Li Z Z, et al. Research on indoor localization based on UWB ranging technology. *Communication Power Technology*, 2018, 35(05): 50-53+56.
- [4] Wang Pei, Xu Shan, Xiong Wei, et al. Research on trajectory localization and monitoring technology of bullet and arrow wreckage based on TDOA. *Fire and Command Control*, 2023, 48(11): 139-144+151.
- [5] An Jinxia, Qin Zhigang, Li Xuan, et al. Comprehensive situational analysis method and application of rocket debris landing site. *Network Security and Data Governance*, 2024, 43(11): 37-42.
- [6] Chen Zhangrui. Reflection and analysis on launch vehicle recovery technology. *Science and Technology Communication*, 2019, 11(06): 140-142.
- [7] Dai Yufan, Jin Hongping. Indoor localization method based on K-means and KNCN algorithm. *Journal of Hubei Institute of Automobile Industry*, 2024, 38(04): 59-63+68.
- [8] Albert A, Alves S, André M, et al. Acoustic positioning for deep sea neutrino telescopes with a system of piezo sensors integrated into glass spheres. *Experimental Astronomy*, 2025, 59(1): 6.
- [9] Fumiaki T, Motoyuki K. An approximate travel time calculation and a robust GNSS-acoustic positioning method using an MCMC technique. *Earth, Planets and Space*, 2022, 74(1).
- [10] Geng Aoting. Research on key technology of multi-station passive localization based on AOA. Nanchang University, 2023.
- [11] Wu P. Research on key technology of multi-station passive localization based on TDOA. National University of Defense Technology, 2019.
- [12] Guo Jian, Zeng Zhihao, Huang Xihang. Secondary localization of mobile robot based on improved least squares method. *Combined Machine Tools and Automated Machining Technology*, 2024, (12): 62-66+71.
- [13] Petrushka K, Petrushka I, Yuxhman Y. Assessment of the Impact of Military Actions on the Soil Cover at the Explosion Site by the Nemerov Method and the Pearson Coefficient Case Study of the City of Lviv. *Journal of Ecological Engineering*, 2023.
- [14] Xi Z L, Lu W. Application of Kmeans Algorithm with Pearson Coefficient in College Student Sports Quality and Sports Resources. *Advanced Materials Research*, 2014, 3078(905): 725-730.
- [15] Zhang Xiaodong, Li Bo, Zhang Tiange, et al. Calculation and analysis of wind deviation of transmission lines based on K-mean clustering algorithm. *Electrical Technology*, 2023, 24 (12): 20-26+34.
- [16] hemiakina A, Khrisanfov M, Chikurova N, et al. Getting Insights Into Chromatographic Properties of HILIC and Mixed-Mode Homemade Stationary Phases Using Principal Component and Cluster Analyses. *Journal of Chemometrics*, 2025, 39(3): e70019.
- [17] Díaz T M, Ruiz M A, Henríquez L P. Functional PCA and cluster analysis for determining temperature patterns in Chile. *Theoretical and Applied Climatology*, 2025, 156(3): 186.
- [18] Mao Chunxian. Research on the method of solving system of super definite linear equations based on vector DSP. Hunan University of Science and Technology, 2023.

